The Role of Exotic Mesons and Final State Interactions in e^+e^- Collisions

Dissertation
zur Erlangung des Grades
„ Doktor der Naturwissenschaften “

am Fachbereich Physik, Mathematik und Informatik
der Johannes Gutenberg-Universität Mainz

vorgelegt von

Daniel Alberto Stanischesk Molnar

geboren in São Paulo (Brasil)

Mainz, 2022

Abstract

In recent years, a plethora of new resonances has been discovered in the charmonium region, which cannot be interpreted in a simple quark model picture as states consisting of a charm quark and an anti-charm quark. A study of the reaction dynamics through which such states are produced is crucial to understand the intrinsic properties of these exotic resonances and for shedding light on their nature. A powerful non-perturbative tool to analyze hadronic processes is the dispersive formalism, which is based on the fundamental physical principles of causality, crossing symmetry and unitarity of the S-matrix. In this thesis we apply this formalism to investigate three reactions in which charged exotic mesons were observed by the BESIII Collaboration. We account for these exotic mesons explicitly as intermediate states in the process and incorporate final state interactions (FSI) through a Muskhelishvili-Omnès approach in order to provide a physical description of the experimental data.

First, we study the process $e^+e^- \to \psi(2S)\,\pi^+\pi^-$ at four different electron-positron center of mass energies q for which data exists. For this reaction, the $\pi\pi$-FSI can be accounted for through a single channel formalism. We observe a distinct behavior for each energy, indicating a change of the underlying physical process. For the lowest energies $q = 4.226$ GeV and $q = 4.258$ GeV, considering the $Z_c(3900)$ as the intermediate state is essential to describe the invariant mass distributions. In contrast, at $q = 4.358$ GeV, there is no evidence of any intermediate states and the line shape of the data can be described with good precision using only the $\pi\pi$-FSI. For the highest energy $q = 4.416$ GeV, a new heavier state is necessary to describe the experimental data. After performing a scan search we find that a charged intermediate state with mass 4.016(4) GeV and width 52(10) MeV provides the best description of the peaks in the $\psi(2S)\pi^\pm$ mass distribution. We observe that the $\pi\pi$-FSI is essential to explain the $\pi^+\pi^-$ invariant mass distribution for all energies.

We next extend the formalism to a $\pi\pi/K\bar{K}$ coupled-channel FSI and consider the $Z_c(3900)$ as the intermediate state, in order to investigate the process $e^+e^- \to J/\psi\,\pi^+\pi^-$ at $q = 4.23$ GeV and $q = 4.26$ GeV. Since the phase space for this reaction is much larger, we need to consider the $\pi\pi$ and $K\bar{K}$ rescattering simultaneously. The formalism not only allows to describe the $J/\psi\pi^\pm$ and $\pi^+\pi^-$ invariant mass distributions very well, but also predicts the $J/\psi K$ and $K\bar{K}$ line shapes. Furthermore, we also use the formalism to predict the angular distributions of J/ψ and $Z_c(3900)$.

For the third process $e^+e^- \to h_c\,\pi^+\pi^-$, studied at $q = 4.23$ GeV and $q = 4.26$ GeV, we account for a relative angular momentum between the pion-pair and h_c. Furthermore, we also consider explicitly the charged exotic meson $Z_c(4020)$ as an intermediate state and investigate scenarios with and without including the $Z_c(3900)$. Assuming the $Z_c(4020)$ as an axial-vector, we predict the angular distributions of h_c.

Zusammenfassung

In den letzten Jahren wurde in der Charmonium-Region eine Fülle neuer Resonanzen entdeckt, die sich in einem einfachen Quark-Modell nicht als Zustände interpretieren lassen, die aus einem Charm-Quark und einem Anti-Charm-Quark zusammen gesetzt sind. Eine Untersuchung der Reaktionsdynamik, durch die solche Zustände erzeugt werden, ist entscheidend, um die intrinsischen Eigenschaften dieser exotischen Resonanzen zu verstehen und ihre Natur zu ergründen. Eine machtvolle, nicht-perturbative Methode zur Analyse hadronischer Prozesse ist der dispersive Formalismus, der auf den grundlegenden physikalischen Prinzipien der Kausalität, Crossingsymmetrie und Unitarität der S-Matrix basiert. In dieser Arbeit wenden wir diesen Formalismus an, um drei Reaktionen zu untersuchen, in denen geladene exotische Zustände von der BESIII-Kollaboration beobachtet wurden. Wir berücksichtigen diese exotische Zustände explizit als Zwischenzustände in den Prozessen und beziehen die Endzustandswechselwirkung (EZW) durch einen Muskhelishvili-Omnès-Ansatz ein, um eine physikalische Beschreibung der experimentellen Daten zu erlangen.

Zuerst untersuchen wir den Prozess $e^+e^- \to \psi(2S)\,\pi^+\pi^-$ bei vier verschiedenen Elektron-Positron-Massenschwerpunktsenergien q, für die Daten vorliegen. Für diese Reaktion kann die $\pi\pi$-EZW in einem Einkanalformalismus berücksichtigt werden. Wir beobachten für jede Energie ein bestimmtes Verhalten, was auf eine Veränderung durch den zugrunde liegenden physikalischen Prozess hinweist. Für die niedrigsten Energien $q = 4.226$ GeV und $q = 4.258$ GeV ist die Berücksichtigung von $Z_c(3900)$ als Zwischenzustand wesentlich, um die invarianten Massenverteilungen zu beschreiben. Im Gegensatz dazu gibt es bei $q = 4.358$ GeV keine Hinweise auf irgendwelche Zwischenzustände und die Daten können mit guter Genauigkeit nur mit dem $\pi\pi$-EZW beschrieben werden. Für die höchste Energie $q = 4.416$ GeV ist ein neuer, schwererer Zustand notwendig, um die experimentellen Daten zu beschreiben. Nach der Suche mittels eines Scanverfahrens stellen wir fest, dass ein geladener Zwischenzustand mit einer Masse 4.016(4) GeV und einer Breite von 52(10) MeV die beste Beschreibung der Peaks in der Massenverteilung von $\psi(2S)\pi^\pm$ liefert. Wir beobachten, dass die $\pi\pi$-EZW wesentlich ist, um die $\pi^+\pi^-$ invariante Massenverteilung für alle Energien zu erklären.

Als nächstes erweitern wir den Formalismus zu einem $\pi\pi/K\bar{K}$ Zweikanalformalismus und betrachten $Z_c(3900)$ als Zwischenzustand, um den Prozess $e^+e^- \to J/\psi\,\pi^+\pi^-$ bei einer Energie von $q = 4.23$ GeV und $q = 4.26$ GeV zu untersuchen. Da der Phasenraum für diese Reaktion viel größer ist, müssen wir die Rückstreuung von $\pi\pi$ und $K\bar{K}$ gleichzeitig berücksichtigen. Der Formalismus erlaubt nicht nur die $J/\psi\pi^\pm$ und $\pi^+\pi^-$ invarianten Massenverteilungen sehr gut zu beschreiben, sondern kann auch die Massenverteilungen für $J/\psi K$ und $K\bar{K}$ voraussagen. Außerdem verwenden wir den Formalismus, um die Winkelabhängigkeit von J/ψ und $Z_c(3900)$ vorherzusagen.

Für den dritten Prozess $e^+e^- \to h_c\,\pi^+\pi^-$, untersucht für die Energien $q = 4.23$ GeV und $q = 4.26$ GeV, berücksichtigen wir einen relativen Drehimpuls zwischen dem Pionenpaar und h_c. Außerdem betrachten wir explizit das geladene exotische Meson $Z_c(4020)$ als Zwischenzustand und untersuchen Szenarien mit und ohne den Zustand $Z_c(3900)$. Unter der Annahme, dass $Z_c(4020)$ ein axialer Vektor ist, sagen wir die Winkelabhängigkeit von h_c voraus.

List of publications

[1] Daniel A. S. Molnar, Igor Danilkin and Marc Vanderheaghen "The role of charged exotic states in $e^+e^- \to \psi(2S)\pi^+\pi^-$",
Phys. Lett. B **797**, 134851 (2019), arXiv:1903.08458 [hep-ph].

[2] Igor Danilkin, Daniel A. S. Molnar and Marc Vanderheaghen "Simultaneous description of the $e^+e^- \to J/\psi\pi\pi(K\bar{K})$",
Phys. Rev. D **102**, 016019 (2020), arXiv:2004.13499 [hep-ph].

[3] Igor Danilkin, Daniel A. S. Molnar, Marc Vanderheaghen and BESIII Collaboration "Dispersive Analysis of $e^+e^- \to h_c\pi^+\pi^-$",
In preparation.

Contents

Chapter 1

Introduction

Hadron physics studies the particles in nature that feel the strong nuclear force. Despite the fact that this field has a long history, there are still many fundamental questions to answer, such as: How many hadrons exist? What is their internal structure? What are their properties? How do they interact and decay?

In 1934, Yukawa predicted the existence and the approximate mass of the mediator particle of nuclear forces [4]. This particle, the pion, was later measured in cosmic rays by Lattes *et.al.* in 1947 [5, 6]. In the following years, with the technological development of particle detectors and the increase of accessible energy ranges in particle accelerators, hundreds of new strongly interacting particles were found. At that time, these hadrons were believed to be distinct elementary particles, giving rise to the term "particle zoo". In 1964 Gell-Mann [7] and independently Zweig [8] introduced the concept that these particles were in fact not elementary, but composed of combinations of particles and antiparticles, named quarks by Gell-Mann. This classification of hadrons according to their valance quark content, the so-called quark model, distinguishes mesons (bosons), which are particles composed of an even number of quarks, and baryons (fermions), which are made up of an odd number of quarks. The lack of experimental evidence of free quarks made Gell-Mann refer to quarks as merely convenient mathematical constructs, not real particles.

Parallel to the development of the quark model during the 1960's, experiments at Stanford Linear Accelerator Center (SLAC) on deep inelastic scattering (DIS) revealed that protons and neutrons are not elementary particles, indicating that they do have internal structure. In order to explain the DIS experiment, Feynman led the formulation of the parton model, which considers that partons form the internal structure of hadrons [9], but these objects were not yet identified as quarks. Feynman argued that

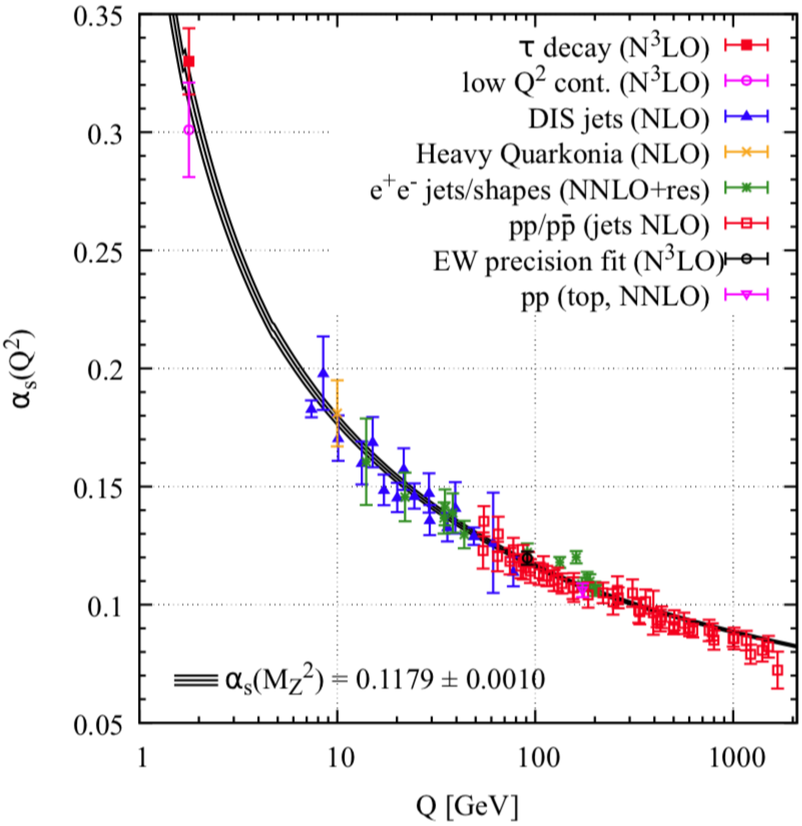

FIGURE 1.1: Behavior of the running coupling of QCD (α_S) as function of the energy scale Q [10].

the high energy experiments show that partons are real particles and not just abstract mathematical concepts.

The inconsistency with the Pauli principle due to the fact that the quark model allowed for states of three quarks of the same flavor (e.g. $\Delta^{++} = uuu$) was not understood at that time. This was overcome by the conjecture of an additional quantum number, called color, in order to fix the (anti-)symmetry (total) wave function problem for baryons. The concept of color as the source of a strong field led to the formulation of a renormalizable quantum field theory for the strong interactions in the 1970s [11]. Quantum chromodynamics (QCD) describes the color interaction among quarks, where gluons are the massless force carrier bosons. The theory is based on a non-Abelian SU(3) color gauge symmetry and exhibits two main properties, asymptotic freedom and color confinement, which are related to the energy-dependence of the coupling constant. In 1973 Gross, Wilczek [12] and independently Politzer [13], observed that quarks interact weakly at high energies, they are asymptotically free. This means the

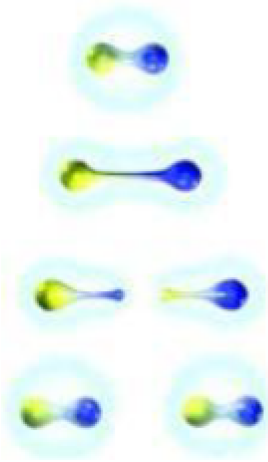

Figure 1.2: Simple depiction of string breaking, one of the defining characteristics of a confining gauge theory [23].

coupling constant of QCD at high energies is small, allowing the use of pertubative methods in the calculation. Many experiments confirm the running behavior of the coupling constant of QCD as shown in Fig.1.1. This fact was very important to consolidate the theory, since it enabled precise predictions using QCD, as for instance, the prediction of angular distribution of jets of hadrons in electron-positron collisions [10, 14–19]. For low energies though, the QCD coupling constant increases and perturbation theory breaks down. In this energy region the quarks are not quasi-free particles. The energy required to separate two quarks increases with the distance between them, they are confined to hadrons and can not be observed separately. Instead, at some point the increasing energy is sufficient to spontaneously create a quark-antiquark pair from the vacuum, resulting therefore in two hadrons instead of isolated color states. This phenomenon, known as string breaking, which is depicted in Fig.1.2, is a direct consequence of color confinement. Perturbation theory cannot be applied for distances close to the confinement length, making low energy phenomena accessible only to non-perturbative methods. Lattice QCD is a well-established, non-perturbative approach to solving QCD numerically by discretizing space-time. Its simulations show results compatible with confinement [20] and have allowed for many successful pre- and post-dictions in agreement with experiments [21, 22]. Another method for the purpose of understanding the spectroscopy of hadrons is the use of models which incorporate the essential features of QCD, such as the quark model.

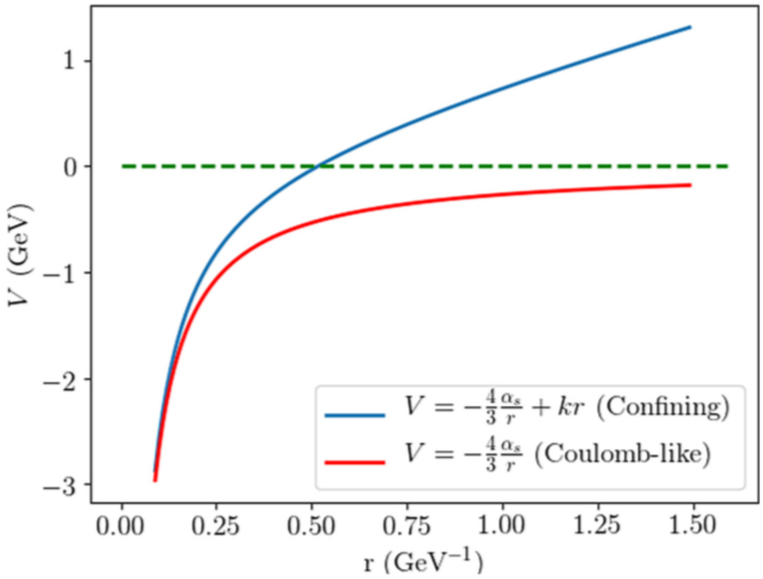

FIGURE 1.3: Comparison between confining QCD potential (blue line) and Coulomb-like potential (red line) in terms of the distance between quarks, extracted from Ref.[24]. The models are generated with $\alpha_s = 0.2$ and $k = 1$ GeV^2.

In 1974, the discovery of an electrically neutral, very heavy particle with the extraordinarily long lifetime of $10^{-20}s$, the J/ψ meson, led to a debate about its nature [25, 26]. The most successful explanation was given by the quark model [27], which required a new fourth quark, with a mass much heavier than the three light quarks up ($m_u \approx 2.4$ MeV), down ($m_d = 4.8$ MeV) and strange ($m_s \approx 95$ MeV). This new heavy quark is known as charm quark ($m_c \approx 1.3$ GeV). The idea of the existence of a fourth quark was not new, it had already been proposed by Bjorken and Glashow a decade earlier [28]. In the quark model, the J/ψ is a bound state of a charm quark and its antiparticle ($c\bar{c}$), also called charmonium. For heavy quarks, such as the charm quark, as well as the bottom quark ($m_b \approx 4.2$ GeV) discovered later in 1977 [29], one can solve a non-relativistic equation to determine the mass spectrum, using a phenomenological potential, which satisfies the properties of QCD. At short distance, one-gluon exchange dominates the interaction, which adds a term to the potential, similar to the Coulomb interaction ($\sim 1/r$). At large distances, a second term, which rises linearly with the distance between the quarks, accounts for confinement. An example of this potential is shown in Fig.1.3. This simple model was very successful not only in describing the particles that were already discovered, but also in predicting new hadrons. The charmonium spectrum is shown in Fig.1.4, where the blue lines indicate the states predicted

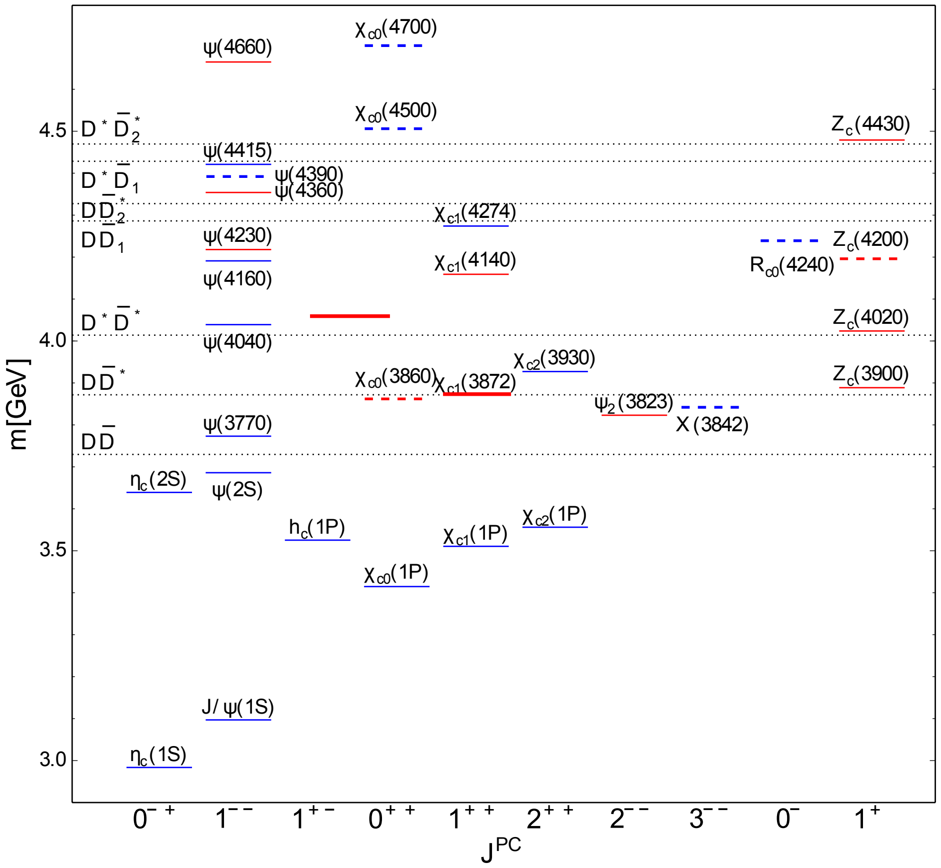

FIGURE 1.4: The charmonium spectrum taken from Ref.[30]. The established $c\bar{c}$ states are indicated by solid blue lines while the exotic candidates with established quantum numbers are shown by the red lines. The dashed lines refer to states that are claimed but yet not established. The horizontal dotted black lines show the relevant open-charm mesons thresholds.

within the quark model and observed experimentally.

At the beginning of the 21st century, one of the main goals of Babar and Belle collaborations was to measure CP-violating processes and compare to Standard Model predictions. However, they accidentally discovered new states incompatible with the quark model predictions. These new states were referred to as exotic. The X(3872), recently renamed as $\chi_{c_1}(3872)$, was the first exotic state found in the charmonium spectrum, discovered in 2003 by Belle collaboration and confirmed by CDF and D0

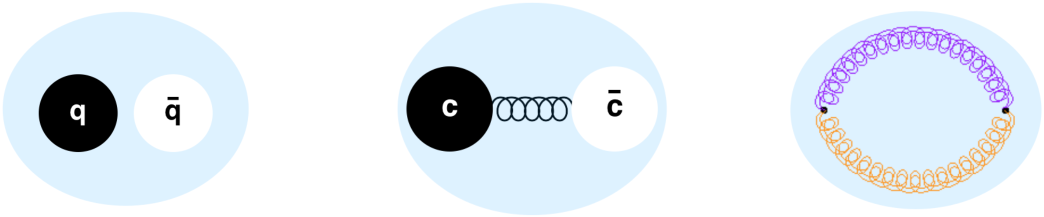

(A) Quark Model (B) Quark-Gluon Hybrid (C) Glueball

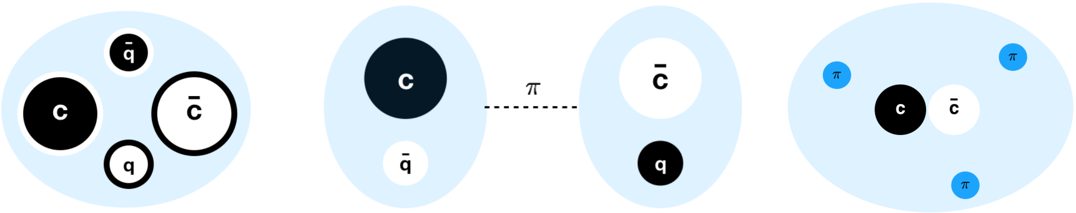

(D) Tetraquark (E) Mesonic Molecule (F) Hadrocharmonium

FIGURE 1.5: Pictorial representation of models for the substructure of a meson. Black and white colors represent particle and antiparticle, respectively.

collaborations [31, 32]. Afterwards, many exotic state candidates started to be observed experimentally and it was especially surprising when the Belle collaboration claimed that a charged exotic state $Z_c^-(4430)$ was detected in the charmonium spectrum in 2007 [33]. It was the first charged charmonium-like state observed in the invariant mass distribution of B decays, $B \to K\pi^-\psi(2S)$. In order to explain such a state a minimal quark content of four quarks is required ($c\bar{c}d\bar{u}$). Only in 2013, seven years later, it was confirmed by LHCb [34] and observed again by Belle [35]. In the same year, BESIII observed a new charged charmonium-like state $Z_c(3900)$ in electron-positron annihilation $e^-e^+ \to \pi^+\pi^-J/\psi$, confirming the existence of charged exotic states [36]. From there on, several further new charged states were claimed to be observed experimentally in the charmonium sector [37–39]. The exotic candidates are shown as red lines in Fig.1.4. Notice that the mass of all exotic candidates lies above the $D\bar{D}$ threshold.

At the moment, the nature of exotic mesons is still a puzzle in the hadron physics community. QCD allows more complex structures for mesons than the conventional quark model picture, such as quark-gluon hybrid, glueball, tetraquark, mesonic molecule and hadrocharmonium, see Fig.1.5 for pictorial illustration of the models. A quark-glue hybrid is a two quark state combined with one or more gluons in an excited state, while a glueball is a meson comprised only of gluons. Both explanations are not sufficient

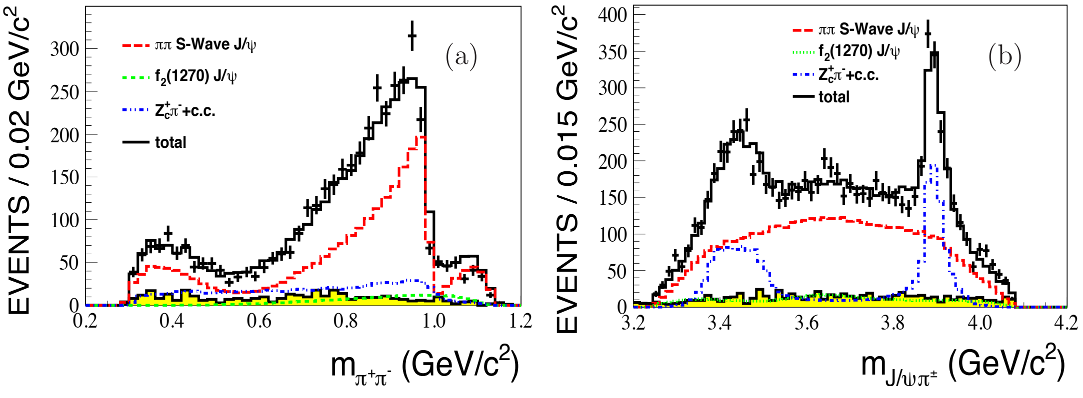

FIGURE 1.6: Experiemntal data for invariant mass distributions of $e^+e^- \to J/\psi\,\pi^+\pi^-$ at e^+e^- center-of-mass energy 4.23 GeV, where the individual contributions to the total fit are detailed in Ref.[51].

to explain charged exotic states, but they can explain mesons with exotic quantum numbers, such as 0^{--}, 0^{+-}, 1^{-+}, etc. A tetraquark consist of four quarks compacted together interacting through color force, whereas a mesonic molecular state is formed by two mesons bound together via Yukawa-like nuclear forces. Another explanation is the so-called hadrocharmonium, which is a quarkonium core surrounded by a cloud of light mesons. Beyond the exotic explanations, it is also possible that the experimental signals associated with new states could be interpreted as kinematic effects. For detailed reviews about exotic states see Refs.[30, 39–50]. More experiments and more detailed theoretical investigations of different reactions are crucial to clarify the nature of these states.

For conventional heavy quarkonium states above open-charm or open-bottom thresholds, the branching fractions in open-flavor decay modes are found to be two or three orders of magnitude larger than the hidden-flavor decay modes. In contrast, many of the newly found exotic states have in common that the hidden-flavor decay modes are only suppressed by a factor of ten or less relative to the open-flavor decay modes and actually turn out to be their discovery channels.

The work that we present in this thesis is an effort to contribute towards a better understanding of the substructures of these exotic states and also their production and decay dynamics. We study in particular the following hidden-flavor decay channels

$$\begin{aligned} &e^+e^- \to \psi(2S)\,\pi^+\pi^-, \\ &e^+e^- \to J/\psi\,\pi^+\pi^-, \\ &e^+e^- \to h_c\,\pi^+\pi^-, \end{aligned}$$

where charged exotic states were found. As an example, consider the experimental data given in Fig.1.6, where the sharp peaks in the $J/\psi\,\pi^\pm$ mass distribution are associated to the charged exotic state $Z_c(3900)$. In order to determine the mass and the width of this exotic state, the $J/\psi\,\pi^\pm$ line shape must be described. However, one needs to simultaneously describe the non-trivial behavior of the $\pi^+\pi^-$ mass distribution, since this provides the necessary background for the $J/\psi\,\pi^\pm$ data. A consistent description of final state interactions can be obtained by using a dispersive formalism, which combines fundamental physical principles such as causality, conservation of probability and crossing symmetry. This allows us to incorporate systematically the strong final state interactions between the pions and kaons, consisting of light quarks, and furthermore to analyse the effects of triangle and anomalous singularities under the hypothesis that Z_c states correspond to the physical resonances. The purpose of this work is to demonstrate a dispersive amplitude analysis, which can be applied to experimental works to describe the whole Dalitz plot with minimal assumptions about the nature of the charged Z_c state. This work resulted in two publications, one in Physics Letter B [1] and the other in Physical Review D [2] and also led to on going collaboration of the theory group in Mainz with the BESIII Collaboration.

The thesis is organized as follows. In Chapter 2, the theory background for this work is introduced. We start by defining the S-matrix of a scattering process and its properties, such as unitarity, crossing symmetry and analyticity. Based on this, we introduce the dispersion theory framework, which enables the reconstruction of the transition amplitudes in a robust approach using these fundamental properties. Next, we introduce the main elements for incorporating the final state interactions (FSI) in our formalism. Furthermore, we discuss different origins of singularities, focusing on resonances and kinematic singularities, which can manifest as signals in experimental observables. At the end of the chapter, we derive the helicity amplitude for a 3-body decay in terms of sequential 2-body decays.

In Chapter 3, we apply the theory presented in the previous chapter to the $\pi\pi$ and KK FSI. We present intermediate results which are used in the formalism, such as the phase shifts and the Omnès functions both in single- and coupled-channel approaches.

In Chapter 4, we define the kinematics and derive the formula for the cross section of processes with two pions and a hidden-charm meson in the final state, produced in electron-positron annihilation.

In the subsequent chapters we apply the formalism to analyze the processes $e^+e^- \to \psi(2S)\,\pi^+\pi^-$ (Chapter 5), $e^+e^- \to J/\psi\,\pi^+\pi^-$ (Chapter 6) and $e^+e^- \to h_c\,\pi^+\pi^-$ (Chapter 7). Using a dispersive formalism, we provide for each channel a physical description of the invariant mass distributions at specific e^+e^- center-of-mass energies. Charged exotic states are accounted for explicitly as intermediate states and the $\pi\pi$ and KK FSI is incorporated through a Muskhelishvili-Omnès approach.

Finally, Chapter 8 summarises the work and presents the conclusions of this thesis. Furthermore, it also gives an outlook on the perspectives which this work creates.

Chapter 2

Theoretical Foundations

The dispersion theory is an elegant formalism based on general physical principles and a very powerful tool to study strongly interacting particles. The scattering process can be divided into three stages: before and after the collision, where the particles can be described by free states and the intermediate stage, which is characterized by the interaction of the particles. Proposed for the first time by Wheeler [52] in 1937, the S-matrix is the operator which transforms the initial state into the final state. Later in 1942, Heisenberg suggested that the S-matrix actually contains all the necessary information to calculate physical observables, such as cross-sections and energies of bound states [53].

The S-matrix can be constructed based on fundamental principles satisfied by the interaction, that is, relativistic covariance of the theory, the unitarity condition and causality. Relativistic covariance means that the observables calculated using the theory should have the same values independently of the inertial frame. The unitarity condition of the S-matrix can be translated into a conservation of probability. This ensures that the probability of all possible outcomes of an interaction must be equal to one (see Section 2.1 for more details). The most general meaning of causality is that the "cause" always precedes the "effect". The relativistic or macroscopic causality is more specific, stating that no physical signal can propagate faster than the speed of the light in the vacuum. A microscopic causality condition, also called local commutativity, is introduced in quantum field theory, defining that the commutator of field operators must vanish at two distinct space-like points, which implies that there is no interference of measurement performed at these positions. The introduction of the causality condition in the properties of the S-matrix is essentially equivalent to ensuring analyticity (holomorphicity) of the S-matrix when the energy variables are extended to complex values. Consequently, the application of the Cauchy's integral theorem and considering the asymptotic behavior at infinity in the complex plane give rise to the dispersion relations for the scattering amplitude.

In this chapter we present the theory background for this thesis. First, we define the S-matrix of a scattering process and its properties such as unitarity, crossing symmetry and analyticity. As a next step, we show that using these fundamental principles one can construct dispersion relations, which relate the total transition amplitude with its discontinuity via an integration in the complex plane. Afterwards, we introduce the main elements for final state interactions that we use in this thesis. We then briefly discuss resonances in the complex plane, the Dalitz region resulting from a three body final state, and kinematic effects originating from triangle diagrams. Finally at the end of the chapter, we derive the helicity amplitude for a 3-body decay, expressed as a sequential 2-body decay. For further reading and additional details see Refs. [54–67].

2.1 Unitarity of the S-Matrix

In a scattering process, the S-matrix is the operator, which relates the initial and final states

$$|f\rangle = S\,|i\rangle\,, \tag{2.1}$$

where $|i\rangle$ and $|f\rangle$ are are asymptotic states corresponding to free particles before and after the interaction. Thus, the probability of measuring the respective final state is given by the absolute value squared of the matrix element

$$\mathcal{P}_{i\to f} = |\,\langle f|\,S\,|i\rangle\,|^2. \tag{2.2}$$

From the conservation of the particle flux, one can see that the probability of the initial state going to any final state must be equal to one

$$\sum_f \mathcal{P}_{i\to f} = \sum_f |\,\langle f|\,S\,|i\rangle\,|^2 = 1. \tag{2.3}$$

Consequently, due to the conservation of probability, the S-matrix operator has to be unitary

$$S^\dagger S = S S^\dagger = \mathbb{1}. \tag{2.4}$$

It is convenient to express the S-matrix in two terms, separating explicitly the non-interacting part

$$S = \mathbb{1} + iT, \tag{2.5}$$

where $\mathbb{1}$ is the trivial term, when the particles do not interact. The T-matrix operator (T) describes the interaction process, which due to the unitarity of the S-matrix, satisfies the relation

$$T - T^\dagger = iT^\dagger T = iTT^\dagger. \tag{2.6}$$

Considering four-momentum conservation, the transition amplitude, which contains the main information about the scattering, is given by

$$\langle f| T |i\rangle = (2\pi)^4 \delta^4(p_f - p_i) T_{fi}, \tag{2.7}$$

leading to the following equation

$$\langle f| T |i\rangle - \langle f| T^\dagger |i\rangle = (2\pi)^4 \delta^4(p_f - p_i) \left(T_{fi} - T^*_{if}\right). \tag{2.8}$$

The difference of the transition amplitude on the right-hand side of Eq.(2.8), for interactions that obey time reversal symmetry ($T_{fi} = T_{if}$), is simply its imaginary part,

$$\mathrm{Im} T_{fi} = \frac{T_{fi} - T^*_{if}}{2i}. \tag{2.9}$$

Introducing a complete set of intermediate states on the right hand side of the Eq.(2.6) leads to

$$\langle f| iTT^\dagger |i\rangle = i \sum_n \langle f| T |n\rangle \langle n| T^\dagger |i\rangle = i(2\pi)^8 \sum_{\{n\}} \delta^4(p_f - p_n) \delta^4(p_n - p_i) T_{fn} T^*_{in}. \tag{2.10}$$

Therefore, the unitary relation for the transition amplitude can be written as

$$2\,\mathrm{Im}\,T_{fi} = (2\pi)^4 \sum_{\{n\}} \delta^4(p_n - p_i) T_{fn} T^*_{in}, \tag{2.11}$$

where $\sum_{\{n\}}$ contains the phase-space integral and the sum over all possible intermediate states, given by the expression

$$\sum_{\{n\}} = \sum_n \int \prod_{j=1}^{n} \frac{d^3 p_j}{(2\pi)^3 2E_j}. \tag{2.12}$$

2.2 Crossing Symmetry

Consider next a 2 → 2 scattering process of scalar particles with different masses

$$A(p_a) + B(p_b) \to C(p_c) + D(p_d), \tag{2.13}$$

with $p_i = (E_i, \vec{p}_i)$, where the index i indicates a, b, c or d. The 4-momentum conservation reads

$$p_a + p_b = p_c + p_d \tag{2.14}$$

and the on-shell condition is given by

$$p_i^2 = m_i^2, \tag{2.15}$$

where m_i is the mass of each particle. It is convenient to use Lorentz invariant kinematic variables, commonly called Mandelstam variables, to describe the scattering process

$$\begin{aligned} s &= (p_a + p_b)^2 = (p_c + p_d)^2, \\ t &= (p_a - p_c)^2 = (p_b - p_d)^2, \\ u &= (p_a - p_d)^2 = (p_b - p_c)^2. \end{aligned} \tag{2.16}$$

From Eq.(2.14) and Eq.(2.16), it is possible to see that the following relation is satisfied

$$s + t + u = p_a^2 + p_b^2 + p_c^2 + p_d^2. \tag{2.17}$$

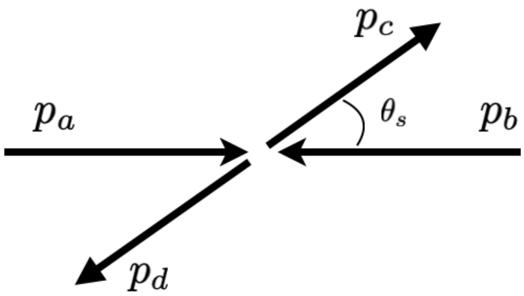

FIGURE 2.1: Pictorial representation of the 2-body scattering in the center of mass frame.

This implies that one of the Mandelstam variables can be written in terms of the other two. Moreover, this means that the two-body scattering can be described with only two independent kinematic variables, usually s and t or one Mandelstam variable and an angle between the momenta. This can also be seen by investigating the number of degrees of freedom. The total number of degrees of freedom in a system is given by the number of all particles (N) times four, due to the 4-momentum of each. However, they are not independent, the conservation of 4-momentum reduces the total number by four degrees of freedom ($p_i = p_f$). Furthermore, we can always fix six degrees of freedom considering Lorentz invariance (three boosts and three rotations). Then using the on-shell condition Eq.(2.15) it is possible to fix N extra degrees of freedom, which gives us the general relation for the number of independent kinematic variables

$$N_{\text{vars}} = 3N - 10. \tag{2.18}$$

Note that the number of independent kinematic variables can be further reduced using the symmetry of the system, see Chapter 4.

In the center of mass frame of the initial and final particles, shown in Fig.2.1, we expand the expressions (2.16) in terms of the masses and momenta of the particles

$$\begin{aligned} s &= m_a^2 + m_b^2 + 2(E_a E_b - |\vec{p_a}||\vec{p_b}|\cos\pi), \\ t &= m_a^2 + m_c^2 - 2(E_a E_c - |\vec{p_a}||\vec{p_c}|\cos\theta_s), \\ u &= m_a^2 + m_d^2 - 2(E_a E_d + |\vec{p_a}||\vec{p_d}|\cos\theta_s), \end{aligned} \tag{2.19}$$

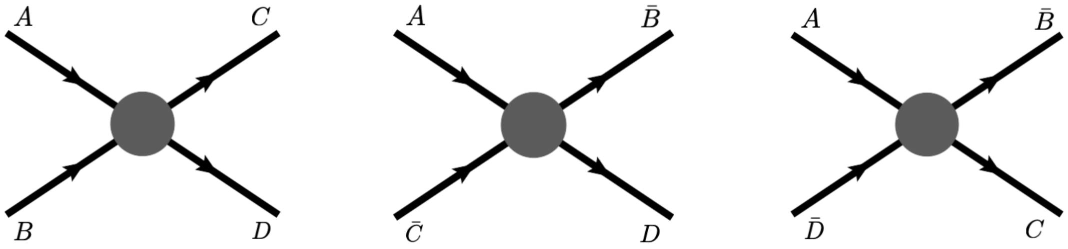

(A) s-channel (B) t-channel (C) u-channel

FIGURE 2.2: The crossing channels of a $2 \to 2$ scattering process where $\bar{B}$, $\bar{C}$ and $\bar{D}$ are the anti-particles of B, C and D, respectively. The analytic expression for scattering in the three channels are given in Eq.(2.26).

with θ_s the angle between the momenta p_a and p_c . The momenta in the center of mass frame are given by

$$\begin{aligned} |\vec{p_i}|^2 = |\vec{p_a}|^2 = |\vec{p_b}|^2 = \frac{\lambda(s, m_a^2, m_b^2)}{4s} = \frac{(s-(m_a+m_b)^2)(s-(m_a-m_b)^2)}{4s}, \\ |\vec{p_f}|^2 = |\vec{p_c}|^2 = |\vec{p_d}|^2 = \frac{\lambda(s, m_c^2, m_d^2)}{4s} = \frac{(s-(m_c+m_d)^2)(s-(m_c-m_d)^2)}{4s}, \end{aligned} \tag{2.20}$$

where $\lambda(a, b, c)$ is the the Källen function

$$\lambda(a, b, c) = a^2 + b^2 + c^2 - 2(ab + bc + ca). \tag{2.21}$$

Remembering that the energies can be expressed in terms of the 3-momenta using the on-shell relation in Eq.(2.15), $E_i^2 = |\vec{p_i}|^2 + m_i^2$, the energies can be rewritten as

$$\begin{aligned} E_a = \frac{s + m_a^2 - m_b^2}{2\sqrt{s}}, \quad E_b = \frac{s + m_b^2 - m_a^2}{2\sqrt{s}}, \\ E_c = \frac{s + m_c^2 - m_d^2}{2\sqrt{s}}, \quad E_d = \frac{s + m_d^2 - m_c^2}{2\sqrt{s}}. \end{aligned} \tag{2.22}$$

The scattering process described in Eq.(2.13), depicted in Fig.2.2a, indicates that the kinematic variable s is related to the center mass energy of the reaction. Therefore, from expressions (2.20) and (2.22), it can be seen that the minimum energy s has to be larger than the squared sum of the masses of the initial particles ($s \geq (m_a + m_b)^2$). In the same way, to produce the particles with masses m_c and m_d, $s \geq (m_c + m_d)^2$. Thus, we call s_{th} the minimum energy necessary for the scattering process to be allowed. Due to crossing symmetry, the amplitude that describes the scattering process in the s-channel is related to the t-channel (Fig.2.2b) as well as u-channel (Fig.2.2c). In other words, crossing symmetry states that the scattering amplitude in the s-, t- and u-channel is giving by the same analytic function if the kinematic variables are switched

$$\begin{aligned} T_s &\equiv T(s,t,u), \\ T_t &\equiv T(t,s,u), \\ T_u &\equiv T(u,t,s). \end{aligned} \tag{2.23}$$

Notice that for identical particles in the final state (or initial state), one can exchange the final states without changing the amplitude, that is,

$$T(s,t,u) = T(s,u,t) = T_s. \tag{2.24}$$

Therefore, we label the amplitudes with the subscripts s, t and u, indicating the respective channel. Analogously as for the s-channel, we can obtain the minimum values of t and u for the scattering to be allowed in the respective channels. They are given by the following expressions

$$\begin{aligned} s \geq s_{th} &= \max\left[(m_a+m_b)^2, (m_c+m_d)^2\right], \\ t \geq t_{th} &= \max\left[(m_a+m_c)^2, (m_b+m_d)^2\right], \\ u \geq u_{th} &= \max\left[(m_a+m_d)^2, (m_b+m_c)^2\right], \end{aligned} \tag{2.25}$$

$$\begin{aligned} &s\text{-channel:} \quad A(p_a) + B(p_b) \rightarrow C(p_c) + D(p_d) \qquad s \geq s_{th}, \\ &t\text{-channel:} \quad A(p_a) + \bar{C}(-p_c) \rightarrow \bar{B}(-p_b) + D(p_d) \qquad t \geq t_{th}, \\ &u\text{-channel:} \quad A(p_a) + \bar{D}(-p_d) \rightarrow \bar{B}(-p_b) + C(p_c) \qquad u \geq u_{th}, \end{aligned} \tag{2.26}$$

where $\bar{B}$, $\bar{C}$ and $\bar{D}$ are the anti-particles, with reverse four-momenta as compared to the s-channel kinematics. This requires an analytical continuation outside the physical region when going e.g. from the physical s-channel to the physical t-channel.

2.3 Dalitz Region

So far we have constrained our discussion to two-body scattering. However, for the scope of this thesis we also need to discuss decay kinematics. By crossing symmetry, the amplitude for the 2 → 2 scattering is related to the decay process by switching one of the initial particles to the final state. Consider the 3-body decay $A \to B + C + D$. The main condition for the decay process to be allowed is that the mass of the initial particle is heavier than the mass of the three final particles,

$$m_a > m_b + m_c + m_d. \tag{2.27}$$

It is common practice to name the kinematic variables as invariant masses, which are defined as

$$M_{bc}^2 = (p_b + p_c)^2 = (p_a - p_d)^2, \tag{2.28}$$
$$M_{bd}^2 = (p_b + p_d)^2 = (p_a - p_c)^2, \tag{2.29}$$
$$M_{cd}^2 = (p_c + p_d)^2 = (p_a - p_b)^2. \tag{2.30}$$

Also, analogous to Eq.(2.17) they satisfy the relation

$$M_{bc}^2 + M_{bd}^2 + M_{cd}^2 = m_a^2 + m_b^2 + m_c^2 + m_d^2. \tag{2.31}$$

Notice, that in the rest frame of the decaying particle ($p_a = (m_a, \vec{0})$) one can see that the initial energy of the process is fixed to m_a. Moreover, as seen in the previous sections, only two kinematic variables are necessary to describe the process. So, choosing M_{bc}^2 and M_{cd}^2, we observe that they vary within the following range

$$\begin{aligned} (m_b + m_c)^2 \leq M_{bc}^2 \leq (m_a - m_d)^2, \\ (m_c + m_d)^2 \leq M_{cd}^2 \leq (m_a - m_b)^2. \end{aligned} \tag{2.32}$$

The variable M_{cd}^2 can be expressed in terms of M_{bc}^2 and the angle θ between the momenta of particles C and D, by expanding the Eq.(2.30), analogous to Eq.(2.19). In the following it will be also convenient to consider the center of mass (CM) frame of particles B and C. In such a frame we can use the similar expressions as given in Eq.(2.20) and Eq.(2.22) for the momenta and energies, respectively. Thus,

$$M_{cd}^2 = m_c^2 + m_d^2 + 2\left(E_c E_d - \vec{p_c}\vec{p_d}\cos\theta\right). \tag{2.33}$$

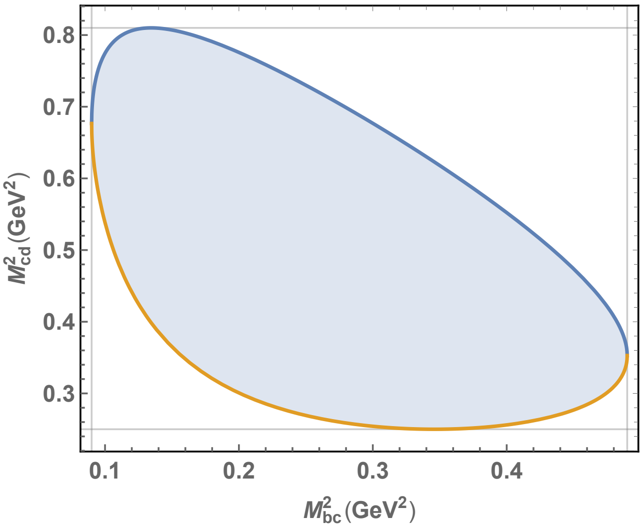

FIGURE 2.3: Dalitz plot of a 3-body decay $A \to B + C + D$, with $m_a = 1, m_b = 0.1, m_c = 0.2, m_d = 0.3$. The vertical and horizontal gray line correspond to the range in Eq.(2.32). The blue and yellow curves constrain the decay region accordingly with Eq.(2.34).

The maximum and minimum values of M^2_{cd} are obtained when $\cos\theta = \pm 1$, which means that the momenta $\vec{p_c}$ and $\vec{p_d}$ are parallel or antiparallel.

$$\begin{aligned} M^{2\,(\max)}_{cd} &= m_c^2 + m_d^2 + \frac{1}{2M^2_{bc}}\left(M^2_{bc} - m_b^2 + m_c^2\right)\left(m_a^2 - M^2_{bc} - m_d^2\right) \\ &+ \frac{1}{2M^2_{bc}}\sqrt{\lambda(M^2_{bc}, m_a^2, m_d^2)\lambda(M^2_{bc}, m_b^2, m_c^2)}, \\ M^{2\,(\min)}_{cd} &= m_c^2 + m_d^2 + \frac{1}{2M^2_{bc}}\left(M^2_{bc} - m_b^2 + m_c^2\right)\left(m_a^2 - M^2_{bc} - m_d^2\right) \\ &- \frac{1}{2M^2_{bc}}\sqrt{\lambda(M^2_{bc}, m_a^2, m_d^2)\lambda(M^2_{bc}, m_b^2, m_c^2)}, \end{aligned} \tag{2.34}$$

where the Källen function (λ) is given by Eq.(2.21). Notice that we could analogously express M^2_{bc} in terms of M^2_{cd} in the same way. The physical region for the decay process is given by Eqs.(2.32) and (2.34), which can be depicted in the so-called Dalitz plot [68, 69], shown in Fig.2.3 for $m_a = 1, m_b = 0.1, m_c = 0.2, m_d = 0.3$. It is also common to project one of the invariant masses by integrating the other over the range given by Eq.(2.34).

2.4 Partial Wave Expansion

The partial wave expansion of a scattering amplitude, corresponds to a sum of one-variable amplitudes with well defined angular momentum (J). Decomposing the amplitude in an angular momentum basis is a convenient approach since the angular momentum is conserved in the process. Assuming azimuthal symmetry, the partial wave expansion for an amplitude with four particles with helicities λ_a, λ_b, λ_c and λ_d is given by

$$T_{\lambda_a\lambda_b\lambda_c\lambda_d}(s,t) = N\sum_{J=0}^{\infty}(2J+1)d^J_{\Lambda_i\Lambda_f}(\theta_s)t^J_{\lambda_a\lambda_b\lambda_c\lambda_d}(s), \tag{2.35}$$

where θ_s is the angle between the momenta p_a and p_c, Λ_i is the difference of the helicities of the initial particles $\Lambda_i = \lambda_a - \lambda_b$, analogously Λ_f is the difference of the helicities of the final particles $\Lambda_f = \lambda_c - \lambda_d$ and $d^J_{\Lambda_i\Lambda_f}$ is the Wigner d-function. The normalization factor N depends on the reaction and is needed to ensure the same unitarity condition for identical and non-identical particles. In this thesis, we study the scattering of spinless particles ($\lambda_a = \lambda_b = \lambda_c = \lambda_d = 0$), as well as reactions with two vector (λ_a and λ_b varying among ± 1 and 0) and two pseudoscalar states ($\lambda_c = \lambda_d = 0$). Moreover, we observe that amplitudes with different helicities ($\lambda_a \neq \lambda_b$) are suppressed in the respective reactions, therefore the Wigner d-functions simplifies

$$d^J_{00}(0,\theta_s,0) = P_J(\cos\theta_s), \tag{2.36}$$

where $P_J(\cos\theta_s)$ are first kind Legendre polynomials. For simplicity, we drop the helicity indices from now onwards and consider scalar particles in this section. Consequently, applying the simplification in Eq.(2.36) to Eq.(2.35), we obtain

$$T(s,t) = N\sum_{J=0}^{\infty}(2J+1)P_J(\cos\theta_s)t_J(s). \tag{2.37}$$

Using the orthogonality of the Legendre polynomials

$$\int_{-1}^{+1} P_m(x)P_n(x)dx = \frac{2\delta_{mn}}{2n+1}, \tag{2.38}$$

the partial wave amplitude $t_J(s)$, which depends only on one kinematic variable, reads

$$t_J(s) = \frac{1}{N}\int_{-1}^{+1}\frac{dz_s}{2}P_J(z_s)T(s,t(z_s)), \tag{2.39}$$

where $z_s = \cos\theta_s$. Notice that in our case it is convenient to perform the partial wave expansion using the kinematic variable s, however one can also apply the partial wave method using the variable t or u.

Analogous to Eq.(2.5), the S-matrix, for a specific angular momentum J, can also be expressed in terms of a non-interacting term and the partial wave scattering amplitude,

$$S_J(s) = 1 + 2i\sigma(s)t_J(s), \tag{2.40}$$

where we explicitly indicate the two-body phase space $\sigma(s)$, which can be expressed as

$$\sigma(s) = \frac{1}{16\pi}\frac{2p_f(s)}{\sqrt{s}}\,, \tag{2.41}$$

with momenta p_f given by Eq.(2.20). The S-matrix continues to be unitary for each partial wave. Notice that when considering inelastic reactions the absolute modulus squared of the S-matrix is equal to an inelastic factor η,

$$|S_J(s)|^2 = \eta(s), \tag{2.42}$$

where the inelastic factor lies between 0 and 1, $0 \leq \eta(s) \leq 1$. The S-matrix can also be expressed in terms of the change in phase from incoming to outgoing particles, called phase shift $\delta_J(s)$,

$$S_J(s) = \eta(s)e^{2i\delta_J(s)}. \tag{2.43}$$

Accordingly, the scattering amplitude in terms of the phase shift reads

$$t_J(s) = \frac{\eta(s)e^{2i\delta_J(s)} - 1}{2i\sigma(s)}. \tag{2.44}$$

For the elastic case Eq.(2.44) simplifies to

$$\begin{aligned} t_J(s) =& \frac{e^{2i\delta_J(s)}-1}{2i\sigma(s)} = \frac{e^{i\delta_J(s)}\sin\delta_J(s)}{\sigma(s)} \\ =& \frac{1}{\sigma(s)\cot\delta_J(s) - i\sigma(s)} = \frac{[\sigma(s)]^{2J}}{[\sigma(s)]^{2J+1}\cot\delta_J(s) - i[\sigma(s)]^{2J+1}}. \end{aligned} \tag{2.45}$$

At low energy, the term in the denominator on the right-side of Eq.(2.45) can be expanded as

$$[\sigma(s)]^{2J+1}\cot\delta_J(s) \approx -\frac{1}{a_J} + \frac{r_J}{2}[\sigma(s)]^2 - \cdots, \tag{2.46}$$

where for S-wave ($J=0$) the effective range r_0 is related to the range of the interaction and the scattering length a_0 is related to the cross section for $s \to s_{th}$

$$\frac{d\sigma}{d\Omega} \approx |t_0(s)|^2 \approx a_0^2. \tag{2.47}$$

From the expression of the S-matrix in terms of the partial wave amplitude, as given in Eq.(2.40), we can derive a unitary relation for the partial wave amplitude $t_l(s)$ in the same way as for Eq.(2.11)

$$\text{Im } t_J^{(fi)}(s) = \sum_n \sigma_n(s) t_J^{(fn)}(s) t_J^{(in)}(s)^*, \tag{2.48}$$

where $\sigma_n(s)$ is the phase space of the internal particles and the superscript indices in the parenthesis are the coupled channel indices. Let us assume that the internal particles are simply the rescattering of the final states. For elastic scattering processes and below any inelastic threshold, Eq.(2.48) can be simplified

$$\text{Im } t_J(s) = \sigma(s)|t_J(s)|^2. \tag{2.49}$$

As soon as the first inelastic channel opens, we can rewrite Eq.(2.48) in a 2×2 matrix equation,

$$\text{Im } T_J(s) = T_J(s)\Sigma(s)T_J(s)^*, \tag{2.50}$$

where $T_J(s)$ is now a matrix,

$$T_J(s) = \begin{bmatrix} t_J^{(11)} & t_J^{(12)} \\ t_J^{(21)} & t_J^{(22)} \end{bmatrix} \tag{2.51}$$

and $\Sigma(s)$ is a matrix with the phase space of the channels on the diagonal,

$$\Sigma(s) = \begin{bmatrix} \sigma_1(s)\theta(s-s_1) & 0 \\ 0 & \sigma_2(s)\theta(s-s_2) \end{bmatrix}, \tag{2.52}$$

where $\theta(s-s_i)$ is the Heavyside function, which is zero below the respective thresholds. The coupled-channel scattering is discussed in more detail later in Section 3.4.

2.5 Analyticity

In the previous sections we saw that the unitarity of the S-matrix gives rise to an equation which relates the imaginary part of the scattering amplitude with its modulus squared, shown in Eq.(2.49). Also, considering the degrees of freedom of a $2 \to 2$ process, the scattering amplitude can be expressed in terms of two kinematic variables and the s-, t- and u-channel are related due to the crossing symmetry of the scattering process.

In this section, we turn our attention to the analyticity of the S-matrix, which states that the scattering amplitude is an analytic function of the kinematic variables when they are continued to complex values. Since the kinematic variables are real numbers, we perform the analytical continuation by adding a small imaginary part ($i\epsilon$). The original physical amplitude is recovered when the limit of $\epsilon \to 0$ is taken. Notice that from now on we work only with the partial wave amplitude $t_J(s)$, which depends only on one kinematic variable. For convenience, we drop the angular momentum index, since the propeties we show next are valid for every angular momentum J. Conventionally, the physical amplitude $t(s)$ is determined when we approach the real s-axis from above,

$$t(s) = \lim_{\epsilon \to 0^+} t(s + i\epsilon). \tag{2.53}$$

Now, looking at the complex s-plane, one needs to identify the singularities of $t(s)$. For the scattering process described in Eq.(2.26), the first singularity is the threshold s_{th}, which defines the beginning of the physical region, that is, the minimal energy for the scattering process to happen. This threshold s_{th} is also called first right-hand cut. It generates a cusp on the positive real s-axis and more cuts appear as one increases the number of intermediate particles. Since s is a function of t and u (See Eq.(2.17)), one can see that left-hand cuts (s_l) will emerge in the complex s-plane when the crossed channels are taken into account. Considering that the allowed kinematic regions in the crossed channel start from their respective thresholds t_{th} and u_{th}, the left-hand cuts are given by

$$s_l^{(\pm)} = s(t = t_{th}, \cos\theta_t = \pm 1), \tag{2.54}$$

$$s_l^{(\pm)} = s(u = u_{th}, \cos\theta_u = \pm 1), \tag{2.55}$$

where the left-hand cuts are originated from the t- and u-channel, with θ_t and θ_u the polar angle in the respective channel, analogous to θ_s given in the Eq.(2.19). The region on the real-axis between s_l and s_{th} is not physical, which means that it is not kinematically accessible in the scattering. However, bound states singularities can appear in this region. These are the only possible singularities in the first, or so-called physical, Riemann sheet.

The second Riemann sheet, also called unphysical sheet, is smoothly connected to the physical one above the threshold (s_{th}) at the real s-axis,

$$t^{II}(s - i\epsilon) = t^{I}(s + i\epsilon)\,, \quad s > s_{th}\,, \tag{2.56}$$

where the indices I and II represent explicitly the respective sheet. For values of s going above new thresholds (s_{th_i}) the number of Riemann sheets will increase consequently.

The Cauchy theorem summarizes the analytic properties of the scattering amplitude by expressing it in a dispersion relation (DR), the Cauchy integral representation for $t(s)$ is

$$t(s) = \oint_C \frac{ds'}{2\pi i}\frac{t(s')}{s' - s}. \tag{2.57}$$

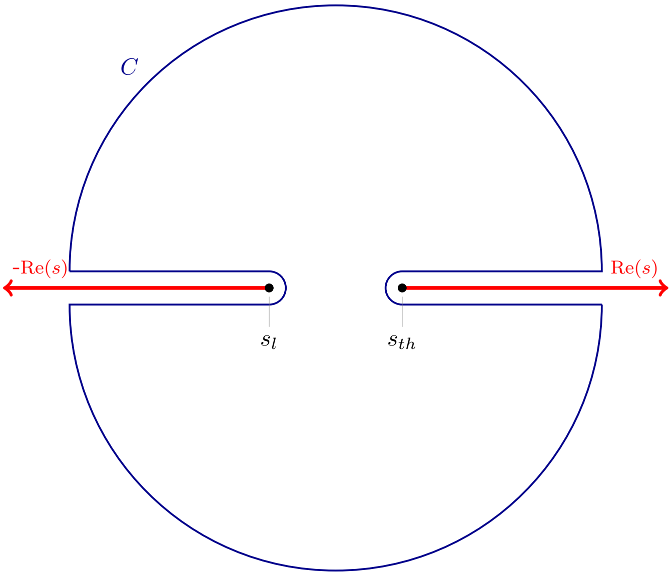

FIGURE 2.4: Integration contour in the s-plane, where the real-axis is indicated in red and the first left- and right-hand cut are labeled as s_l and s_{th}, respectively.

The closed integration contour C, shown in Fig.2.4 is taken anticlockwise and $t(s)$ is holomorphic inside of the region. Considering that

$$\lim_{|s|\to\infty} t(s) = 0 \tag{2.58}$$

and that the radius of the circle C tends to infinity, implying that the curved part of the contour C will vanish, one gets a DR for $t(s)$

$$t(s) = \int\limits_{-\infty}^{s_l} \frac{ds'}{2\pi i} \frac{t(s'+i\epsilon) - t(s'-i\epsilon)}{s'-s} + \int\limits_{s_{th}}^{\infty} \frac{ds'}{2\pi i} \frac{t(s'+i\epsilon) - t(s'-i\epsilon)}{s'-s}. \tag{2.59}$$

The Schwarz's reflection principle states that if an analytic function $f(z)$ is defined on the upper half-plane and is well-defined with real values on the real axis, then it can be analytically continued to the entire plane, that is

$$f(z^*) = f^*(z). \tag{2.60}$$

Therefore, with $t(s)$ satisfying these conditions, we can use Eq.(2.60),

$$t(s - i\epsilon) = t^*(s + i\epsilon), \tag{2.61}$$

with $\epsilon \to 0$ and positive. In this way, the discontinuity (Disc) of the amplitude can be related to its imaginary part as

$$\text{Disc } t(s) \equiv \frac{t(s+i\epsilon) - t(s-i\epsilon)}{2i} = \text{Im } t(s). \tag{2.62}$$

Therefore, using Schwarz's reflection, the DR in Eq.(2.59) can be rewritten in terms of the imaginary part of the scattering amplitude

$$t(s) = \int\limits_{-\infty}^{s_l} \frac{ds'}{\pi} \frac{\text{Im } t(s')}{s' - s - i\epsilon} + \int\limits_{s_{th}}^{\infty} \frac{ds'}{\pi} \frac{\text{Im } t(s')}{s' - s - i\epsilon}, \tag{2.63}$$

where the infinitesimal imaginary part $i\epsilon$ was explicitly included to keep the right definition of s.

When the asymptotic behavior of the amplitude does not satisfy the condition in Eq.(2.58), the contribution from the curved part of the circle in Fig.2.4 does not vanish. In this case, it is possible to subtract the DR in order to assure its convergence. The subtraction process of a dispersion relation is

$$\begin{aligned} t(s) &= \int \frac{ds'}{\pi} \frac{\text{Im } t(s')}{s' - s} \frac{(s' - s) + (s - s_0)}{s' - s_0}, \\ t(s) &= a_1 + \frac{(s - s_0)}{\pi} \int \frac{ds'}{(s' - s_0)} \frac{\text{Im } t(s')}{(s' - s)}, \end{aligned} \tag{2.64}$$

where $a_1 = t(s_0)$ is a constant originated by the subtraction

$$a_1 = \frac{1}{\pi} \int \frac{ds'}{(s' - s_0)} \text{Im } t(s'), \tag{2.65}$$

and s_0 is a fixed value of s. By induction we can generalize the Eq.(2.64) to a n-times subtracted DR,

$$t(s) = \sum_{i=0}^{n-1} a_{i+1}(s - s_0)^i + \frac{(s - s_0)^n}{\pi} \int \frac{ds'}{(s' - s_0)^n} \frac{\text{Im } t(s')}{(s' - s)}. \tag{2.66}$$

Analogously, the subtraction constants a_i are given by

$$a_i = \frac{1}{\pi} \int \frac{ds'}{(s' - s_0)^i} \text{Im } t(s'). \tag{2.67}$$

Introducing subtractions improves the convergence at high energies ($s \to \infty$), however there are also additional parameters (a_i), which often are unknown and must be determined from the final observable or matched to other theories such as Chiral Perturbation Theory (ChPT). Notice that the dispersion relations can have more subtractions than the minimum necessary for its convergence (over-subtracted),which reduces the sensitivity to the high-energy region and the extra subtraction can be fixed or compared to its sum-rule given by Eq.(2.67).

In essence, we observed in this section that the DR is a powerful method which combines analiticity, unitarity and crossing symmetry of the S-matrix to reconstruct the total amplitude from its discontinuities.

2.6 Dispersive Formalism

In this section we present how to incorporate rescattering effects using the dispersive formalism. First, we derive the essential element for the inclusion of final state interactions between pions in processes such as $e^+e^- \to \pi\pi\psi$, the Omnès function, which has the phase of the rescattering amplitude as input. Next, we show that by using the Watson theorem, this phase is equal to the phase shift. Subsequently, we explain how to handle the left-hand cuts in the DR, originating from the crossing channels, using the Omnès function. Finally, we present the inverse amplitude method, which allows us to calculate the rescattering amplitude for low energy region and consequently the phase shift.

2.6.1 Omnès Function

Here we discuss the Muskhelishvili-Omnès representation [70, 71], for a detailed derivation see Ref.[72]. The Omnès function relates the amplitude with its phase, which allows us to use the experimental information about the rescattering of the final particles in the dispersive approach. The method consists of finding the most general representation of an analytic function $G(s)$ in the complex s-plane, which has only the right-hand cut. Therefore, assuming that $\phi(s)$ is a real phase along the cut,

$$\arg\left[G(s)\right] = \phi(s), \quad s > s_{th}. \tag{2.68}$$

If $\Omega(s)$ is a special solution, then so is $G(s) = P(s)\Omega(s)$, where $P(s)$ is a real polynomial. Thus,

$$\begin{aligned} \Omega(s \pm i\epsilon) &= |\Omega(s)|e^{\pm i\phi(s)}, \\ \Omega(s - i\epsilon) &= \Omega(s + i\epsilon)e^{-2i\phi(s)}. \end{aligned} \tag{2.69}$$

In this way, we obtain from Eq.(2.69) the discontinuity of the logarithm of $\Omega(s)$

$$\text{Disc} \ln \Omega(s) = \frac{\ln \Omega(s + i\epsilon) - \ln \Omega(s - i\epsilon)}{2i} = \phi(s). \tag{2.70}$$

This allows us to write down a DR for the logarithm of $\Omega(s)$

$$\begin{aligned} \ln \Omega(s) &= \int_{s_{th}}^{\infty} \frac{ds'}{\pi} \frac{\text{Disc} \ln \Omega(s)}{s' - s}, \\ \ln \Omega(s) &= \int_{s_{th}}^{\infty} \frac{ds'}{\pi} \frac{\phi(s')}{s' - s}. \end{aligned} \tag{2.71}$$

By simply taking the exponential of Eq.(2.71), we obtain the function $\Omega(s)$. However, we subtract the dispersion relation once to explicitly ensure the normalization $\Omega(0) = 1$. Therefore, the final expression for the Omnès function is

$$\Omega(s) = \exp\left[\frac{s}{\pi} \int_{s_{th}}^{\infty} \frac{ds'}{s'} \frac{\phi(s')}{s' - s}\right]. \tag{2.72}$$

2.6.2 Watson Theorem

Recall the unitarity relation for the partial wave amplitudes Eq.(2.48)

$$\text{Im } f(s) = \sigma(s)t(s)f(s)^*, \tag{2.73}$$

where for the sake of simplicity, we omit the angular momentum index and consider the intermediate states the same as the final ones, so $t_J^{ni} = t^{fi} = f$ and $t_J^{fn} = t^{ff} = t$. This process is illustrated in Fig.2.5. Writing $f(s)$ in the polar form

$$f(s) = |f(s)|e^{i\phi(s)} \tag{2.74}$$

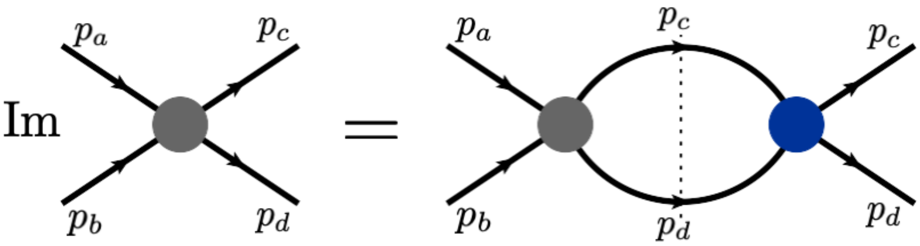

FIGURE 2.5: Diagrammatic picture of the unitary equation (2.73), where $f(s)$ is represented by the gray vertices and $t(s)$ by the blue vertex.

and expressing $t(s)$ (Eq.(2.45)) in terms of its phase shift $\delta(s)$,

$$t(s) = \frac{e^{i\delta(s)} \sin\delta(s)}{\sigma(s)}, \tag{2.75}$$

we observe that Eq.(2.73) gives

$$e^{i\phi(s)} \sin\phi(s) = e^{i\delta(s)} \sin\delta(s). \tag{2.76}$$

This implies that the phase $\phi(s)$ of the total amplitude is equal to the phase shift $\delta(s)$ of the amplitude $t(s)$,

$$\phi(s) = \delta(s) + k\pi, \quad k = \text{integer}. \tag{2.77}$$

This fact is known as the Watson theorem [73], which is only valid below inelastic thresholds and when there is no overlap between the left-hand cut and the right-hand cut. Notice that due to the Watson theorem, we can use the experimental phase shift as the phase of the amplitude, and in doing so, we are able to include the whole rescattering information of the final particles, as we will see in Chapter 3.

Asymptotic Behavior

Since we are dealing with dispersion relations which are integrated up to infinity, we need to investigate the asymptotic behavior of the Omnès function. We will see in Section 2.6.3, that the Omnès function appears inside the dispersive integral. Thus, we start by evaluating the principal value of the integral,

$$\begin{aligned}\Omega(s) &= \exp\left[\frac{s}{\pi}\int_{s_{th}}^{\infty}\frac{ds'}{s'}\frac{\phi(s')}{s'-s-i\epsilon}\right] = \exp\left[\frac{s}{\pi}\;p.v.\int_{s_{th}}^{\infty}\frac{ds'}{s'}\frac{\phi(s')}{s'-s}+i\phi(s)\right]\\ &= \exp\left[\frac{s}{\pi}\int_{s_{th}}^{\infty}\frac{ds'}{s'}\frac{\phi(s')-\phi(s)}{s'-s}+\frac{s}{\pi}\;p.v.\int_{s_{th}}^{\infty}\frac{ds'}{s'}\frac{\phi(s)}{s'-s}+i\phi(s)\right]\\ &= \exp\left[\frac{s}{\pi}\int_{s_{th}}^{\infty}\frac{ds'}{s'}\frac{\phi(s')-\phi(s)}{s'-s}+\frac{\phi(s)}{\pi}\ln\frac{s_{th}}{s-s_{th}}+i\phi(s)\right]\\ &= \exp\left[\frac{s}{\pi}\int_{s_{th}}^{\infty}\frac{ds'}{s'}\frac{\phi(s')-\phi(s)}{s'-s}\right]\left(\frac{s_{th}}{s-s_{th}}\right)^{\frac{\phi(s)}{\pi}}e^{i\phi(s)}. \qquad (2.78)\end{aligned}$$

Since for $s \to \infty$ the phase goes to a constant, $\phi(s \to \infty) = k\pi$, with $k =$ real, then the asymptotic behavior of the Omnès function is

$$\Omega(s \to \infty) = s^{-k}. \qquad (2.79)$$

2.6.3 Muskhelishvili-Omnès Formalism

As seen in the previous sections, the DR is an equation which relates the amplitude to its discontinuity. Remembering the general relation for the DR (2.63), we rewrite it in terms of the discontinuity,

$$f(s) = \int_{-\infty}^{s_l}\frac{ds'}{\pi}\frac{\text{Disc }f(s')}{s'-s-i\epsilon}+\int_{s_{th}}^{\infty}\frac{ds'}{\pi}\frac{\text{Disc }f(s')}{s'-s-i\epsilon} \equiv f_l(s)+f_r(s), \qquad (2.80)$$

where the amplitude can be explicitly separated in two terms with only the left-hand cuts (f_l) and right-hand cuts (f_r). In order to solve the Eq.(2.80), we use the Muskhelishvili-Omnès formalism, which is based on writing a DR for the combination,

$$\mathcal{F}(s) = \frac{f(s)-f_l(s)}{\Omega(s)}, \qquad (2.81)$$

where Ω is the Omnès function described in the previous section, which constrains through unitarity the right-hand cuts of $t(s)$ and $f(s)$, according to the Watson theorem 2.6.2. One can immediately observe that we chose the ansatz $\mathcal{F}$ purposefully without left-hand cuts. This implies that the discontinuity of $\mathcal{F}$ is zero for s below s_l

$$\underset{s<s_l}{\underline{\text{Disc}}}\,\mathcal{F} = 0. \qquad (2.82)$$

It follows that the DR for $\mathcal{F}$ has only the integral with the right-hand cut,

$$\mathcal{F}(s) = \int_{s_{th}}^{\infty} \frac{ds'}{\pi} \frac{\text{Disc}\, \mathcal{F}(s')}{s' - s - i\epsilon}. \tag{2.83}$$

The discontinuity of $\mathcal{F}$ above the right-hand cut is given by

$$\begin{aligned} \text{Disc}\, \mathcal{F}(s) &= \text{Disc}\left[\frac{f(s) - f_l(s)}{\Omega(s)}\right], \\ &= \underbrace{\text{Disc}\left[f(s)\Omega(s)^{-1}\right]}_{0} - f_l(s)\text{Disc}\left[\Omega(s)^{-1}\right], \end{aligned} \tag{2.84}$$

where the discontinuity of $f(s)\Omega(s)^{-1}$ is zero, because the phase of $f(s)$ is the same as $\Omega(s)$. Consequently, plugging Eq.(2.81) and Eq.(2.84) in Eq.(2.83) we obtain a simplified version of the DR (2.80)

$$f(s) = f_l(s) - \Omega(s) \int_{s_{th}}^{\infty} \frac{ds'}{\pi} \frac{f_l(s)\text{Disc}\left[\Omega(s)^{-1}\right]}{s' - s - i\epsilon}. \tag{2.85}$$

This DR is essential for the analyses we perform in this thesis. The Omnès function $\Omega(s)$ introduces the final state interaction into the dispersion formalism. The amplitudes $f_l(s)$ introduce the left hand cuts to our approach and depend on the reaction as will be described in Chapters 5 and 6.

2.7 Resonances

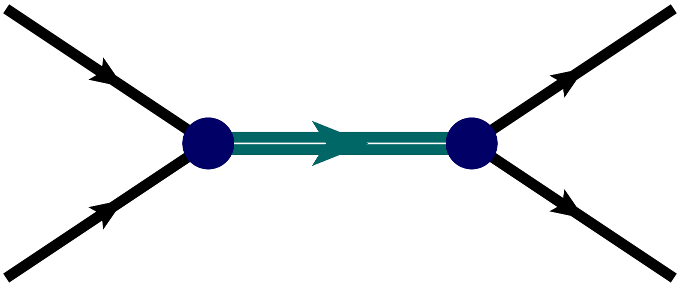

FIGURE 2.6: Diagrammatic representation of a resonance generated in a scattering process.

One of the key challenges of particle physics is to understand the meaning of line shapes in the experimental data. Peaks, bumps and dips in the observable are associated with

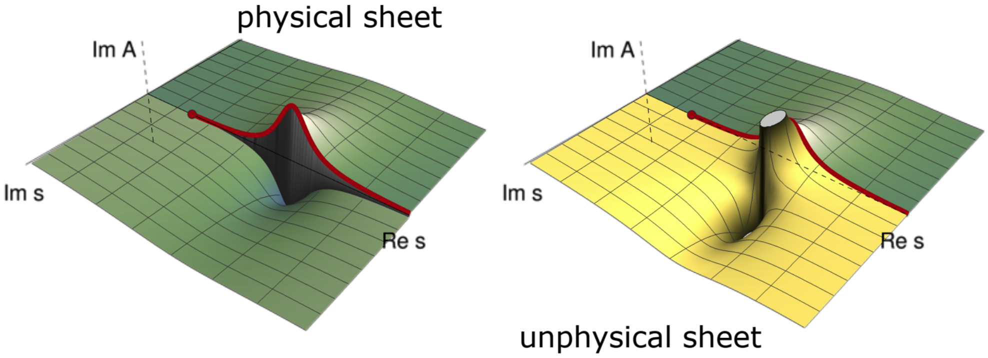

FIGURE 2.7: Complex plane illustration of a single isolated resonance. As one can see, the resonance produces a pole in the unphysical Riemann sheet (yellow plane). The closer the pole is from the physical region (red line), the higher the impact on the physical sheet (green plane). This figure was extracted from Ref.[37].

a physical process. Basically, the structures in the cross section can have two different natures, either they are particle states, such as resonances or bound states, or they are simply scattering kinematical effects, which will be discussed in more detail later in this thesis. A bound state is understood as a hadronic molecule and it manifests itself as a pole on the real axis of the first (physical) Riemann sheet below the first threshold. Due to unitarity and causality, there are only branch cuts (left- and right-hand cut, see previous sections) and bound states in the first Riemann sheet.

A resonance on the other hand is a pole in the second (unphysical) Riemann sheet, thus it has a negative imaginary part above the threshold. One of the simplest and widely used amplitude representations for the resonances is given by the Breit-Wigner (BW) propagator

$$A(s) = \frac{1}{s - m^2 + im\Gamma}, \tag{2.86}$$

where Γ is the decay width, which is inversely associated to the lifetime (τ) of the state, $\Gamma \propto 1/\tau$. Notice that since the mass has always a positive fixed value, the size of the width shows also how far from the physical region the resonance lies.

Applying the unitary relation in Eq.(A.1) to the BW representation for the amplitude in Eq.(2.86), one can observe that the decay width has to be energy dependent, that is, it depends on the s Mandelstam variable, $\Gamma(s)$. Moreover, a constant Γ would imply an imaginary part for the BW-amplitude below threshold. However unitarity says that the imaginary part of the amplitude below threshold is zero. Since one would have to know all possible decay channels with the respective coupling constants, introducing an energy-dependent decay width $\Gamma(s)$ would most certainly add a model-dependence to the representation of the BW. A simple way to ensure that the respective amplitude has no imaginary part below threshold is to write a DR for the BW-amplitude [74, 75],

$$\hat{A}(s) = \int_{s_{th}}^{\infty} \frac{ds'}{\pi} \frac{\mathrm{Im} A(s')}{s' - s - i\epsilon}. \tag{2.87}$$

Notice that the BW-amplitude (2.86) has only the right-hand cut. The Eq.(2.87) is known as the spectral representation and gives the correct analyticity properties for the amplitude resonance as shown in Ref.[76].

2.8 Triangle Singularities

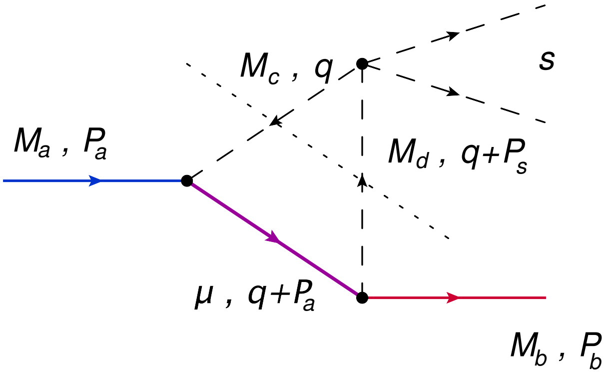

FIGURE 2.8: Triangle-loop diagram for a 3-body decay ($M_a \to M_b + M_c + M_d$). The dotted line represents the cut, which indicates the propagators that are taken to be on-shell.

In the previous section we discussed that a resonance is a pole in the unphysical Riemann sheet of the S-matrix. Usually it produces an enhancement in physical observables, mostly in the shape of a peak. Other types of singularities, when they are located near the physical region, can also produce similar patterns. However, they do not have the same origin. Resonances are particle states, defined by the interaction among quarks and gluons, therefore the position of the singularity is always fixed in the complex plane. The kinematic singularities are completely reaction dependent, in other words, the location of the singularities is determined only by the masses and energies of the particles involved. Kinematic singularities are also called Landau singularities, since their position is given by the Landau equations [77]. Squared root branch cuts from two-body thresholds are the simplest case of Landau singularities. They generate a cusp at the two-body threshold of S-wave channels [78]. In this section we focus our attention on a more complicated type of Landau singularity, the so-called triangle singularity. For a recent and detailed review on kinematic singularities in hadronic reactions see Ref.[79].

Triangle singularities emerge when the internal particles of a triangle loop diagram can go simultaneously on-shell, which in other words means that the intermediate particles in the loop can become real propagating particles, this is also known as Coleman-Norton theorem [80].

Let us now consider the triangle loop diagram shown in Fig.2.8. We can evaluate the diagram in two different ways, the standard loop calculation via the Feyman parametrization or using dispersion theory. Both start in the same way, by applying the Feynman rules and writing down the loop integral

$$\mathcal{T} = -i \int \frac{d^4q}{(2\pi)^4} \frac{1}{q^2 - M_c^2} \frac{1}{(q+P_s)^2 - M_d^2} \frac{1}{(q+P_a)^2 - \mu^2}. \tag{2.88}$$

We briefly describe both methods below, but more details can be found in the Appendix B.

Triangle loop via Feynman parametrization

The Feynman parametrization of a one-loop integral with three propagators is given by

$$\frac{1}{D_1 D_2 D_3} = \Gamma(3) \int_0^1 da \int_0^{1-a} db \frac{1}{[a\, D_1 + b\, D_2 + (1-a-b) D_3]^3}. \tag{2.89}$$

Considering only scalar propagators and vertices, we plug Eq.(B.2) into Eq.(2.88), which solves the four-momenta integral

$$\int \frac{d^4q}{(2\pi)^4} \frac{1}{(q^2 - 2qP - \Sigma)^3} = \frac{-i}{2(4\pi)^2} \frac{1}{\Sigma + P^2}, \tag{2.90}$$

where $P_a^2 = M_a^2$, $P_s^2 = s$ and $P_a P_s = (s + M_a^2 - M_b^2)/2$. Then, the triangle loop amplitude is expressed in terms of integrals of Feynman parameters

$$\mathcal{T} = \Gamma(3) \int_0^1 da \int_0^{1-a} db \frac{1}{2(4\pi)^2} \frac{1}{\Sigma + P^2}, \tag{2.91}$$

where the first integration over db can be performed analytically and the last over da numerically.

Triangle loop via Dispersion Relation

As explained in Section 2.5, knowing the discontinuity one can reconstruct the total amplitude using DR. The discontinuity of Eq.(2.88) is calculated by applying the Cutkosky's "cutting" rule [81] to the propagators of particles M_c and M_d as indicated by the dotted line crossing the respective propagators in Fig.2.8. Cutting the propagators means that they go on-shell, replacing them by a Dirac delta function in the integral in Eq.(2.88), for more details see Appendix B. Thus, the discontinuity of the triangle loop reads

$$Disc\,\mathcal{T} = \frac{1}{64\pi^2} \frac{\lambda^{1/2}(s, M_c^2, M_d^2)}{s} \int d\Omega \frac{1}{\underbrace{(q + P_a)^2}_{t} - \mu^2}. \tag{2.92}$$

Evaluating the integral we obtain the following expression for the discontinuity $\mathcal{T}$

$$Disc\,\mathcal{T} = \frac{1}{16\pi} \frac{1}{\lambda^{1/2}(s, M_a^2, M_b^2)} \log\left(\frac{\mathcal{X}+1}{\mathcal{X}-1}\right), \tag{2.93}$$

where

$$\mathcal{X} = \frac{M_a^2 + M_c^2 - \mu^2 + 2q^0 P_a^0}{2\,|\vec{q}| \cdot |\vec{P}_a|}. \tag{2.94}$$

Consequently, since we do not consider any particular interaction for the vertices, the DR can be written only for the physical region as discussed in the previous sections,

$$\mathcal{T} = \int_{(M_c+M_d)^2}^{\infty} \frac{ds'}{\pi} \frac{Disc\,\mathcal{T}(s')}{s' - s}. \tag{2.95}$$

From the discontinuity in Eq.(2.95), it is possible to see that the triangle loops for a particular kinematics produce logarithmic singularities. These so-called triangle singularities emerge from the first branch cut of the logarithm, located just above the threshold $s_{th} = (M_c + M_d)^2$. Notice that one needs to perform an analytic continuation $M_a^2 \to M_a^2 + i\epsilon$ to ensure that the branching point never crosses the unitarity cut, which guarantees a correct dispersion representation in Eq.(2.95). Since both methods to calculate the loop integral are equivalent, this offers a good possibility to cross-check the method in order to make sure that the approach is producing the desired results.

2.9 Helicity Amplitude

In this section we derive the helicity amplitude for a 3-body decay in terms of sequential 2-body decays. We show how to coherently sum the helicity amplitudes for the sequential 2-body decay in the s-, t- and u-channel, by introducing Wigner rotations to write the helicities in a consistent helicity system. For additional details see Refs.[82, 83].

2-Body Decay

Let us consider a resonance with total angular momentum J, with M its projection in z-direction, decaying to two particles with spins j_1 and j_2 and helicities λ_1 and λ_2, respectively. The 2-body decay amplitude in the CM-frame of the decaying resonance can be expressed in the following way

$$\begin{aligned} H^{J\,M}_{\lambda_1\lambda_2} &= \langle \vec{p}\lambda_1; -\vec{p}\lambda_2 |\, T\, | JM\rangle \\ &= \langle \theta\phi\lambda_1\lambda_2 | JM\lambda_1\lambda_2\rangle\, \tilde{F}^J_{\lambda_1\lambda_2}. \end{aligned} \tag{2.96}$$

$\theta \in [0,\pi]$ and $\phi \in [0, 2\pi]$ are the polar and azimuthal angles of the particle 1 in the rest frame of the decaying particle and $\tilde{F}^J_{\lambda_1\lambda_2}$ are the angular independent helicity-coupling coefficients. The angular dependent part is given by

$$\langle \theta\phi\lambda_1\lambda_2 | JM\lambda_1\lambda_2\rangle = \sqrt{\frac{2J+1}{4\pi}} D^{J\,*}_{M\lambda}(\phi,\theta,0), \tag{2.97}$$

where $\lambda = \lambda_1 - \lambda_2$ and $D^{J\,*}_{M\lambda}(\phi,\theta,0)$ are the Wigner D-functions [1]. We can rewrite Eq.(2.96) as

$$H^{J\,M}_{\lambda_1\lambda_2} = D^{J\,*}_{M\lambda}(\phi,\theta,0) F^{J}_{\lambda_1\lambda_2}. \tag{2.98}$$

where for convenience we redefine the helicity-coupling coefficients as

$$F^{J}_{\lambda_1\lambda_2} = \sqrt{\frac{2J+1}{4\pi}}\tilde{F}^{J}_{\lambda_1\lambda_2}. \tag{2.99}$$

The coefficients $F^{J}_{\lambda_1\lambda_2}$ can be obtained from a Lagrangian with the respective symmetry of the decay, as will be done in this thesis, or they can be expressed in the canonical basis as

$$F^{J}_{\lambda_1\lambda_2} = \sum_{l,s}\sqrt{\frac{2l+1}{4\pi}}\,\langle l0; s\lambda|J\lambda\rangle\,\langle s_1\lambda_1; s_2-\lambda_2|s\lambda\rangle\, a^{J}_{ls}, \tag{2.100}$$

where the bra-ket quantities are Clebsch-Gordan coefficients and the canonical amplitude a^{J}_{ls} is again reaction dependent.

Sequential Two-Body Decays

Let us now consider the following sequential two-body decays,

$$J, M \to J_i, \lambda_i + (J_\alpha, \lambda_\alpha \to J_j, \lambda_j + J_k, \lambda_k), \tag{2.101}$$

where the indices for each channel are

$$\begin{aligned} &s\text{-channel: } \alpha = s, \quad i=1, \quad j=2, \quad k=3, \\ &t\text{-channel: } \alpha = t, \quad i=2, \quad j=3, \quad k=1, \\ &u\text{-channel: } \alpha = u, \quad i=3, \quad j=1, \quad k=2. \end{aligned} \tag{2.102}$$

Notice the intermediate state, also called isobar, $(J_\alpha, \lambda_\alpha)$ can be in the s-, t- and u-channel. The Fig.2.9 visualizes the sequential two-body decay for each decay chain. We can obtain the helicity amplitude for processes by applying the Eq.(2.99) and summing

---

[1] Notice that we use the no-phase convention for the helicity states $(D^{J\,*}_{M\lambda}(\phi,\theta,0))$, similarly as done in Ref.[83]. An alternative is the Jacob-Wick phase convention $(D^{J\,*}_{M\lambda}(\phi,\theta,-\phi))$ [84], which can change the sign of some helicity couplings.

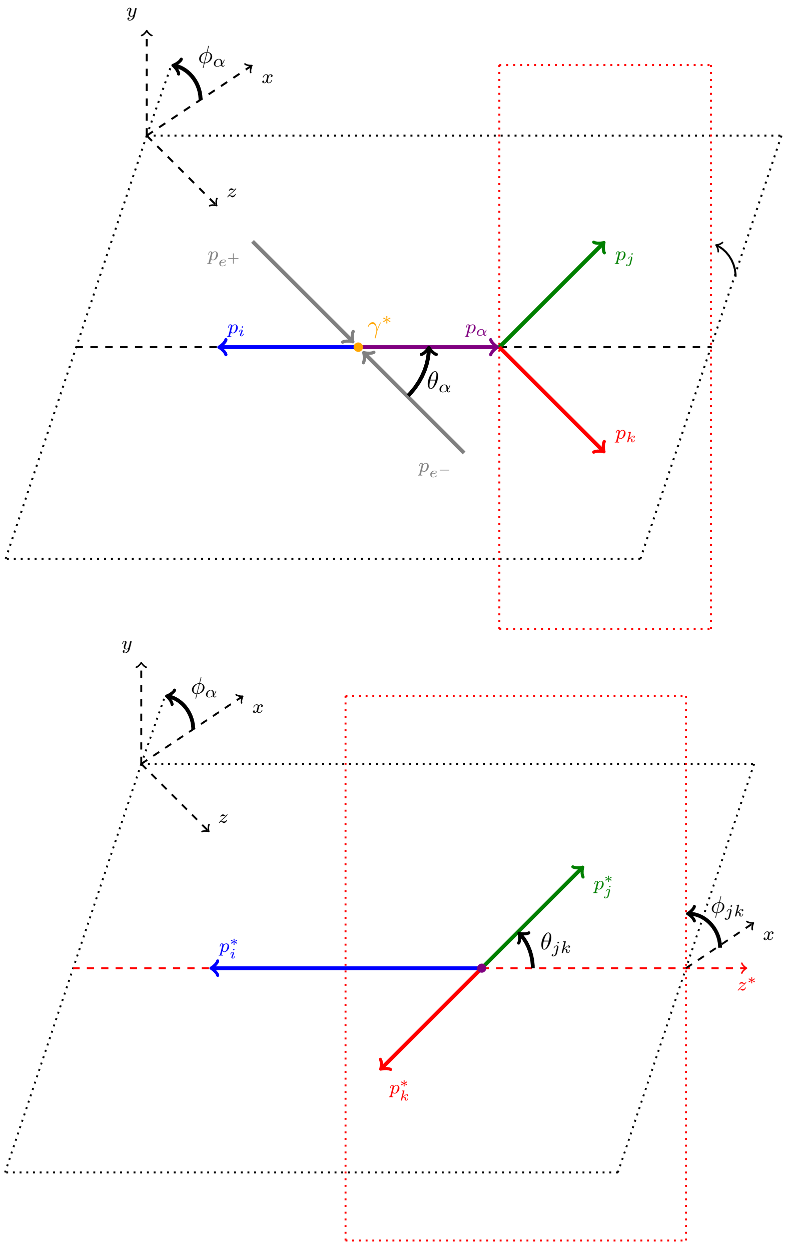

FIGURE 2.9: Visualization of the sequential two-body decay, the top figure shows the e^+e^--CM frame while the bottom figure depicts the isobar jk rest frame. The black dotted plane is the production plane of the first decay with azimuthal angle ϕ_α. The momenta of the second decay lies in the red dotted plane with azimuthal angle ϕ_{jk}. The production beam is aligned with the z-axis, with θ_α the polar angle of the isobar p_α. The polar angle between p_j^* and the z^*-axis is θ_{jk}. The arrows show the momenta of the particles (* indicates quantities in the isobar jk rest frame), where the index α and consequently the indices i, j and k, are related to the decay channels as shown in Eq.(2.102).

over the helicities of the intermediate state, for the s-channel we obtain

$$H^{J\,M\,(s)}_{\lambda_1\lambda_2\lambda_3} = \sum_{\lambda_s} \left(D^{J\,*}_{M(\lambda_s-\lambda_1)}(\phi_s, \theta_s, 0) F^{J}_{\lambda_s\lambda_1} \right) BW(m_s) \left(D^{J_s\,*}_{\lambda_s(\lambda_2-\lambda_3)}(\phi_{23}, \theta_{23}, 0) F^{J_s}_{\lambda_2\lambda_3} \right), \tag{2.103}$$

where the propagator of the intermediate state ($BW(m_s)$) can be expressed in terms of the Breit-Wigner amplitude, discussed in Section 2.7. Consequently, we can also consider the sequential decay in the other channels,

$$H^{J\,M\,(t)}_{\lambda_1\lambda_2\lambda_3} = \sum_{\lambda_t} \left(D^{J\,*}_{M(\lambda_t-\lambda_2)}(\phi_t, \theta_t, 0) F^{J}_{\lambda_t\lambda_2} \right) BW(m_t) \left(D^{J_t\,*}_{\lambda_t(\lambda_3-\lambda_1)}(\phi_{31}, \theta_{31}, 0) F^{J_t}_{\lambda_3\lambda_1} \right), \tag{2.104}$$

$$H^{J\,M\,(u)}_{\lambda_1\lambda_2\lambda_3} = \sum_{\lambda_u} \left(D^{J\,*}_{M(\lambda_u-\lambda_3)}(\phi_u, \theta_u, 0) F^{J}_{\lambda_u\lambda_3} \right) BW(m_u) \left(D^{J_u\,*}_{\lambda_u(\lambda_1-\lambda_2)}(\phi_{12}, \theta_{12}, 0) F^{J_u}_{\lambda_1\lambda_2} \right). \tag{2.105}$$

To sum the helicity amplitudes written in Eqs.(2.103), (2.104) and (2.105), we need to first decide in which channel the helicity will be defined and rotate the other channels accordingly, that ensures that the helicities have the same meaning in every channel. This extra rotation will introduce one Wigner D-function for each particle in the final state. In this thesis we consider processes where $J = 1$, $J_s = 0$, $J_t = J_u = 1$, and $\lambda_2 = \lambda_3 = 0$, which simplify considerably the helicity amplitude. For convenience, we drop the indices λ_2 and λ_3 in the notation. Therefore, choosing the s-channel as the main chain we can express the coherent sum of helicity amplitudes as

$$H^{J\,M}_{\lambda_1} = H^{J\,M\,(s)}_{\lambda_1} + \sum_{\bar{\lambda}_1} H^{J\,M\,(t)}_{\bar{\lambda}_1} D^{J_1\,*}_{\bar{\lambda}_1\lambda_1}(0, \omega_1^{(t)}, \phi_{23}) + \sum_{\bar{\lambda}_1} H^{J\,M\,(u)}_{\bar{\lambda}_1} D^{J_1\,*}_{\bar{\lambda}_1\lambda_1}(0, \omega_1^{(u)}, \phi_{23}). \tag{2.106}$$

The angles (ϕ_t, θ_t) and (ϕ_u, θ_u) can be expressed in terms of (ϕ_s, θ_s) by applying the following rotations

$$\begin{aligned} R_z(\phi_t)R_y(\theta_t)R_z(\phi_{31}) &= R_z(\phi_s)R_y(\theta_s)R_z(\phi_{23})R_y(\bar{\theta}_{ts}), \\ R_z(\phi_u)R_y(\theta_u)R_z(\phi_{12}) &= R_z(\phi_s)R_y(\theta_s)R_z(\phi_{23})R_y(\bar{\theta}_{us}), \end{aligned} \tag{2.107}$$

where $\bar{\theta}_{ts}$ ($\bar{\theta}_{us}$) are the rotation angles that bring the configuration of the t-channel

(u-channel) to the configuration in the s-channel. Using that the Wigner D-functions can be expanded as

$$D^{j}_{m'm}(\alpha,\beta,\gamma) = e^{-im'\alpha}\, d^{j}_{m'm}(\beta)\, e^{-im\gamma}, \tag{2.108}$$

we can rewrite the D-functions in Eqs.(2.103),(2.104) and (2.105) as

$$\begin{aligned}
&D^{J\,*}_{M(\lambda_s-\lambda_1)}(\phi_s,\theta_s,0)D^{J_s\,*}_{\lambda_s 0}(\phi_{23},\theta_{23},0) = D^{J\,*}_{M(\lambda_s-\lambda_1)}(\phi_s,\theta_s,\phi_{23})\, d^{J_s\,*}_{\lambda_s 0}(\theta_{23})\, e^{i\lambda_1\phi_{23}},\\
&D^{J\,*}_{M\lambda_t}(\phi_t,\theta_t,0)D^{J_t\,*}_{\lambda_t(-\lambda_1)}(\phi_{31},\theta_{31},0) = D^{J\,*}_{M\lambda_t}(\phi_t,\theta_t,\phi_{31})\, d^{J_t\,*}_{\lambda_t(-\lambda_1)}(\theta_{31}),\\
&D^{J\,*}_{M\lambda_u}(\phi_u,\theta_u,0)D^{J_u\,*}_{\lambda_u\lambda_1}(\phi_{12},\theta_{12},0) = D^{J\,*}_{M\lambda_u}(\phi_u,\theta_u,\phi_{12})\, d^{J_u\,*}_{\lambda_u\lambda_1}(\theta_{12}).
\end{aligned} \tag{2.109}$$

Finally we can use Eq.(2.107) to express the Wigner D-functions that depend on the angles (ϕ_t,θ_t) and (ϕ_u,θ_u) in terms of the D-function that depends on the angles (ϕ_s,θ_s),

$$\begin{aligned}
D^{J\,*}_{M\lambda_t}(\phi_t,\theta_t,\phi_{31}) &= \sum_{\bar\lambda} D^{J\,*}_{M\bar\lambda}(\phi_s,\theta_s,\phi_{23})\, d^{J}_{\bar\lambda\lambda_t}(\bar\theta_{ts}),\\
D^{J\,*}_{M\lambda_u}(\phi_u,\theta_u,\phi_{12}) &= \sum_{\bar\lambda} D^{J\,*}_{M\bar\lambda}(\phi_s,\theta_s,\phi_{23})\, d^{J}_{\bar\lambda\lambda_u}(\bar\theta_{us}).
\end{aligned} \tag{2.110}$$

In this way it is convenient to rewrite the Wigner D-function for the angles in the s-channel

$$D^{J\,*}_{M(\lambda_s-\lambda_1)}(\phi_s,\theta_s,\theta_{23}) = \sum_{\bar\lambda} D^{J\,*}_{M\bar\lambda}(\phi_s,\theta_s,\phi_{23})\, \delta_{\bar\lambda(\lambda_s-\lambda_1)}. \tag{2.111}$$

Therefore we can factor out the dependence on the angles ϕ_s and θ_s in the helicity amplitude Eq.(2.106) and rewrite it in the following way

$$H^{JM}_{\lambda_1} = \sum_{\bar\lambda} D^{J\,*}_{M\bar\lambda}(\phi_s,\theta_s,\phi_{23})\, e^{i\lambda_1\phi_{23}} H_{\bar\lambda\,\lambda_1}, \tag{2.112}$$

where

$$\begin{aligned}
H_{\bar\lambda\,\lambda_1} = \Bigg[&\delta_{\bar\lambda(-\lambda_1)} F^{1}_{0\lambda_1} BW(m_s) F^{0}_{00}\\
&+ \sum_{\lambda_t}\sum_{\bar\lambda_1} d^{1}_{\bar\lambda\lambda_t}(\bar\theta_{ts}) F^{1}_{\lambda_t 0} BW(m_t) F^{1}_{0\bar\lambda_1}\, d^{1}_{\lambda_t(-\bar\lambda_1)}(\theta_{31}) d^{J_1}_{\bar\lambda_1\lambda_1}(\omega_1^{(t)})\\
&+ \sum_{\lambda_u}\sum_{\bar\lambda_1} d^{1}_{\bar\lambda\lambda_u}(\bar\theta_{us}) F^{1}_{\lambda_u 0} BW(m_u) F^{1}_{\bar\lambda_1 0} d^{1}_{\lambda_u\bar\lambda_1}(\theta_{12}) d^{J_1}_{\bar\lambda_1\lambda_1}(\omega_1^{(u)})\Bigg].
\end{aligned} \tag{2.113}$$

The expression of the angles in terms of the independent kinematic variables and direction of rotation are explained in Appendix D. The overall phase given in the term $e^{i\lambda_1\phi_{23}}$ is unobservable and we will thus drop it in further calculations.

Chapter 3

$\pi\pi$ Final State Interaction

This chapter is a direct application of the theory presented in the previous chapter. The $\pi\pi$ scattering is essential to describe the final state interactions (FSI) in all three reactions we study in this thesis. First we start by introducing the pion's quantum numbers and the experimental data available for the $\pi\pi$ scattering. We use the inverse amplitude method (IAM) to calculate the $\pi\pi$ phase shift and scattering amplitude for elastic collisions. As we saw in the previous chapter, with the $\pi\pi$ phase shift we can obtain the Omnès function, which is a key element to explain the rescattering of pions using the experimental information. Last but not least, when the energy is higher than the two kaon threshold, the scattering of pions and kaons is entangled and needs to be analyzed together in a coupled-channel equation. This chapter is mainly based on the references [54, 57, 58, 60, 64–67].

3.1 Isospin States

Pions are the lightest mesons known in particle physics, with $m_{\pi^0} \approx 134.97$ MeV the mass of the neutral state and $m_{\pi^\pm} \approx 139.57$ MeV the mass of the charged states [37]. Thus, it is a good assumption that the lightest quarks up (u) and down (d) can explain the internal structure of pions. In the quark model, the quark flavor eigenstates for pions are

$$\left|\pi^+\right\rangle = \left|u\bar{d}\right\rangle, \qquad \left|\pi^-\right\rangle = \left|d\bar{u}\right\rangle, \qquad \left|\pi^0\right\rangle = \frac{1}{\sqrt{2}}\left(\left|u\bar{u}\right\rangle - \left|d\bar{d}\right\rangle\right). \tag{3.1}$$

Kaons are the second lightest mesons, with $m_{K^0} \approx 497.61$ MeV the mass of the neutral state and $m_{K^\pm} \approx 493.68$ MeV the mass of the charged ones. They also carry strangeness, therefore the quark flavor eigenstates for kaons read

$$\begin{aligned} \left|K^+\right\rangle &= \left|u\bar{s}\right\rangle, & \left|K^0\right\rangle &= \left|d\bar{s}\right\rangle, \\ \left|K^-\right\rangle &= \left|\bar{u}s\right\rangle, & \left|\bar{K}^0\right\rangle &= \left|\bar{d}s\right\rangle. \end{aligned} \tag{3.2}$$

It is common practice in studying strong interactions to describe the state of hadrons in terms of their isospin, since isospin symmetry is a very good symmetry for the strong interactions. From the isospin of the quarks we can construct the the isospin eigenstates for pions $|I, I_3\rangle$

$$\left|\pi^+\right\rangle = -\left|1, +1\right\rangle, \qquad \left|\pi^-\right\rangle = \left|1, -1\right\rangle, \qquad \left|\pi^0\right\rangle = \left|1, 0\right\rangle. \tag{3.3}$$

Thus, pions have isospin $I_\pi = 1$, kaons however are divided into two isodoublets with isospin $I_K = 1/2$

$$\begin{aligned} \left|K^+\right\rangle &= \left|\frac{1}{2}, +\frac{1}{2}\right\rangle, & \left|K^0\right\rangle &= \left|\frac{1}{2}, -\frac{1}{2}\right\rangle, \\ \left|K^-\right\rangle &= -\left|\frac{1}{2}, -\frac{1}{2}\right\rangle, & \left|\bar{K}^0\right\rangle &= \left|\frac{1}{2}, +\frac{1}{2}\right\rangle. \end{aligned} \tag{3.4}$$

The algebra for constructing the $\pi\pi$ and KK isospin states is similar to the spin algebra. The total two-particle isospin varies within the range

$$|I_\alpha - I_\beta| \leq I_{\alpha\beta} \leq I_\alpha + I_\beta, \tag{3.5}$$

where α and β are indices representing each state, respectively. Consequently, for two-pion and two-kaon states one finds

$$\begin{aligned} 0 \leq I_{\pi\pi} \leq 2, \\ 0 \leq I_{KK} \leq 1. \end{aligned} \tag{3.6}$$

The third component of the isospin ($I^{(3)}$) varies in terms of the total isospin (I)

$$-I \leq I^{(3)} \leq +I. \tag{3.7}$$

Using the completeness relation, the coupled state has the following expression

$$\left|I_{\alpha\beta}\; I_{\alpha\beta}^{(3)}\right\rangle = \sum_{I_\alpha^{(3)}=-I_\alpha}^{I_\alpha} \; \sum_{I_\beta^{(3)}=-I_\beta}^{I_\beta} \left|I_\alpha I_\alpha^{(3)} I_\beta I_\beta^{(3)}\right\rangle \left\langle I_\alpha I_\alpha^{(3)} I_\beta I_\beta^{(3)} \middle| I_{\alpha\beta}\; I_{\alpha\beta}^{(3)}\right\rangle , \tag{3.8}$$

where $\left\langle I_\alpha I_\alpha^{(3)} I_\beta I_\beta^{(3)} \middle| I_{\alpha\beta}\; I_{\alpha\beta}^{(3)}\right\rangle$ are the well-known Clebsch-Gordan coefficients. With that in mind, we can write the $\pi\pi$ isospin states in terms of the pion flavors as following

$$\begin{aligned}
|0\,0\rangle &= -\frac{1}{\sqrt{3}}\left(\left|\pi^0\pi^0\right\rangle + \left|\pi^+\pi^-\right\rangle + \left|\pi^-\pi^+\right\rangle\right), \\
|1\,0\rangle &= \frac{1}{\sqrt{2}}\left(\left|\pi^-\pi^+\right\rangle - \left|\pi^+\pi^-\right\rangle\right), \qquad |1 \pm 1\rangle = \frac{1}{\sqrt{2}}\left(\left|\pi^0\pi^\pm\right\rangle - \left|\pi^\pm\pi^0\right\rangle\right), \\
|2\,0\rangle &= \frac{1}{\sqrt{6}}\left(2\left|\pi^0\pi^0\right\rangle - \left|\pi^+\pi^-\right\rangle - \left|\pi^-\pi^+\right\rangle\right), \\
|2 \pm 1\rangle &= \mp\frac{1}{\sqrt{2}}\left(\left|\pi^\pm\pi^0\right\rangle + \left|\pi^0\pi^\pm\right\rangle\right), \qquad |2 \pm 2\rangle = \left|\pi^\pm\pi^\pm\right\rangle .
\end{aligned} \tag{3.9}$$

Analogously, for the K^+K^- and $\bar{K}^0K^0$ isospin states

$$\begin{aligned}
|0\,0\rangle &= -\frac{1}{\sqrt{2}}\left(\left|K^+K^-\right\rangle - \left|K^-K^+\right\rangle\right), \qquad & |0\,0\rangle &= \frac{1}{\sqrt{2}}\left(\left|\bar{K}^0K^0\right\rangle - \left|K^0\bar{K}^0\right\rangle\right), \\
|1\,0\rangle &= -\frac{1}{\sqrt{2}}\left(\left|K^+K^-\right\rangle + \left|K^-K^+\right\rangle\right), \qquad & |1\,0\rangle &= \frac{1}{\sqrt{2}}\left(\left|\bar{K}^0K^0\right\rangle + \left|K^0\bar{K}^0\right\rangle\right), \\
|1 \pm 1\rangle &= \left|K^\pm K^\pm\right\rangle , & |1+1\rangle &= \left|\bar{K}^0\bar{K}^0\right\rangle , \quad |1-1\rangle = \left|K^0K^0\right\rangle .
\end{aligned} \tag{3.10}$$

Since we want to study the 2 → 2 $\pi\pi$-scattering, it is also convenient to express the two-body isospin states in the reverse way. Thus, for two pions we obtain

$$\begin{aligned}
\left|\pi^\pm\pi^\mp\right\rangle &= -\frac{1}{\sqrt{3}}|0\,0\rangle \mp \frac{1}{\sqrt{2}}|1\,0\rangle - \frac{1}{\sqrt{6}}|2\,0\rangle , \\
\left|\pi^\pm\pi^0\right\rangle &= -\frac{1}{\sqrt{2}}\left(|1 \pm 1\rangle \pm |2 \pm 1\rangle\right), \qquad \left|\pi^0\pi^\pm\right\rangle = \frac{1}{\sqrt{2}}\left(|1 \pm 1\rangle \mp |2 \pm 1\rangle\right), \\
\left|\pi^0\pi^0\right\rangle &= -\frac{1}{\sqrt{3}}|0\,0\rangle + \sqrt{\frac{2}{3}}|2\,0\rangle , \qquad \left|\pi^\pm\pi^\pm\right\rangle = |2 \pm 2\rangle .
\end{aligned} \tag{3.11}$$

Using Eq.(3.11), the scattering amplitude for the process $\pi^+\pi^- \to \pi^0\pi^0$ becomes

$$T_s = \left\langle \pi^+\pi^- \middle| T \middle| \pi^0\pi^0 \right\rangle = \frac{1}{3}\underbrace{\langle 0\,0|\, T\, |0\,0\rangle}_{F_0} - \frac{1}{3}\underbrace{\langle 2\,0|\, T\, |2\,0\rangle}_{F_2}, \tag{3.12}$$

where F_i, with $i = 0,1,2$, are the isospin decomposed amplitudes. As seen in Section 2.2, due to crossing symmetry, the amplitudes in the t- and u-channel are related to the s-channel (see Eq.(2.23)). This fact allows us to express the isospin amplitudes in terms of the amplitude in each crossed channel. The scattering process in the t-channel is $\pi^+\pi^0 \to \pi^+\pi^0$, whereas in the u-channel it is $\pi^+\pi^0 \to \pi^0\pi^+$. Analogous to in Eq.(3.12), we can express the scattering amplitudes for each channel in terms of the isospin states

$$\begin{aligned} T_t &= \left\langle \pi^+\pi^0 \middle| T \middle| \pi^+\pi^0 \right\rangle = +\frac{1}{2} \underbrace{\langle 1+1|\, T\, |1+1\rangle}_{F_1} + \frac{1}{2} \underbrace{\langle 2+1|\, T\, |2+1\rangle}_{F_2}, \\ T_u &= \left\langle \pi^+\pi^0 \middle| T \middle| \pi^0\pi^+ \right\rangle = -\frac{1}{2} \underbrace{\langle 1+1|\, T\, |1+1\rangle}_{F_1} + \frac{1}{2} \underbrace{\langle 2+1|\, T\, |2+1\rangle}_{F_2}. \end{aligned} \tag{3.13}$$

Consequently, the isospin amplitudes can be disentangled and expressed in terms of the reduced amplitude of each channel,

$$\begin{aligned} F_0(s,t) &= 3T_s + T_t + T_u, \\ F_1(s,t) &= T_t - T_u, \\ F_2(s,t) &= T_t + T_u. \end{aligned} \tag{3.14}$$

We selected the specific process $\pi^+\pi^- \to \pi^0\pi^0$ to derive the isospin amplitudes, however they can be used for any $\pi\pi \to \pi\pi$. In the next sections we will see that experimental observables of the $\pi\pi$-scattering are obtained for each specific isospin and angular momentum, that is the reason why we need to decompose the amplitude in the isospin basis and apply the partial wave decomposition as described in Section 2.4.

3.2 Single-Channel $\pi\pi$ FSI

As already mentioned previously, in this thesis we include the information about the $\pi\pi$ FSI in the dispersion theory through the Omnès function (see Section 2.6.3). The input of the Omnès function is the phase shift of $\pi\pi$ scattering. However, the upper limit of the dispersive integral is infinite, therefore one needs to know the behavior of the phase shift at high energies. In this section we show that if the physical region of the reaction is below the first inelastic threshold, one can use a single channel approach to work with the $\pi\pi$ FSI.

Inverse Amplitude Method for $\pi\pi$-scattering

The mIAM described in Appendix A can be applied to the $\pi\pi$-scattering, allowing us to calculate the scattering amplitude using ChPT amplitudes, as stated in Eq.(A.13)

$$t^{JI}_{\text{IAM}}(s) = \frac{|t^{JI}_{\text{LO}}(s)|^2}{t^{JI}_{\text{LO}}(s) - t^{JI}_{\text{NLO}}(s) + A^{\text{mIAM}}(s)}, \tag{3.15}$$

where the indices J and I correspond to angular momentum and isospin respectively and the term A^{mIAM} is only necessary for the S-wave ($J = 0$) to fix the position of the Adler zeros. The leading order (LO) and next-to-leading order (NLO) amplitudes are obtained from the ChPT Lagrangian for SU(2) [85–87], which is given by

$$\begin{aligned}
\mathcal{L}_{LO} &= \frac{f_0^2}{4}\text{Tr}\left[\partial_\mu U \partial^\mu U^\dagger\right] + \frac{f_0^2\, m_0^2}{4}\text{Tr}\left[U^\dagger + U\right], \\
\mathcal{L}_{NLO} &= \frac{l_1}{4}\left(\text{Tr}\left[\partial_\mu U \partial^\mu U^\dagger\right]\right)^2 + \frac{l_2}{4}\left(\text{Tr}\left[\partial_\mu U \partial_\nu U^\dagger\right]\right)\left(\text{Tr}\left[\partial^\mu U \partial^\nu U^\dagger\right]\right) \\
&\quad + \frac{m_0^4\, l_3}{16}\left(\text{Tr}\left[U^\dagger + U\right]\right)^2 + \frac{m_0^2\, l_4}{4}\text{Tr}\left[\partial^2 U^\dagger + \partial^2 U\right] + \cdots,
\end{aligned} \tag{3.16}$$

where f_0 is related to the pion decay constant (f_π), m_0 is the bare pion mass (m_π) and the matrix of pion fields is

$$U = \exp\left[\frac{i}{f_0}\begin{pmatrix} \pi^0 & \sqrt{2}\pi^+ \\ \sqrt{2}\pi^- & \pi^0 \end{pmatrix}\right]. \tag{3.17}$$

The one-loop diagrams give rise to ultraviolet divergences, which are removed by renormalizing the l_i low energy constants (LECs) from the NLO Lagrangian. The low energy parameters can be written in scale independent form

$$l_i^r = \frac{\gamma_i}{32\pi^2}\left(\bar{l}_i + \ln\left[\frac{m_0^2}{\mu^2}\right]\right), \tag{3.18}$$

with $\gamma_1 = 1/3$, $\gamma_2 = 2/3$, $\gamma_3 = -1/2$ and $\gamma_4 = 2$.

The quark mass expansion of m_π^2 and f_0 can be written in terms of the μ-independent LECs

$$m_\pi^2 = m_0^2 \left[1 - \frac{1}{32\pi^2}\frac{m_0^2}{f_0^2}\bar{l}_3 + \mathcal{O}(m_0^4)\right], \tag{3.19}$$

$$f_\pi = f_0 \left[1 - \frac{1}{16\pi^2}\frac{m_0^2}{f_0^2}\bar{l}_4 + \mathcal{O}(m_0^4)\right], \tag{3.20}$$

Consequently, the $\pi\pi$ one-loop scattering amplitudes [85–88] are

$$T_s^{LO}\,(s,t,u) \;= \frac{s-m_\pi^2}{f_\pi^2}, \tag{3.21}$$

$$\begin{aligned} T_s^{NLO}(s,t,u) = & \frac{s-m_\pi^2}{f_\pi^2}\frac{m_\pi^2}{8\pi^2 f_\pi^2}\bar{l}_4 - \frac{m_\pi^4}{32\pi^2 f_\pi^4}\bar{l}_3 + \frac{1}{6f_\pi^4}\Big\{3(s^2-m_\pi^2)\bar{J}(s) \\ & + \left[t(t-u) - 2m_\pi^2 t + 4m_\pi^2 u - 2m_\pi^4\right]\bar{J}(t) + \left[u(u-t) - 2m_\pi^2 u + 4m_\pi^2 t - 2m_\pi^4\right]\bar{J}(u)\Big\} \\ & + \frac{1}{96\pi^2 f_\pi^4}\left\{2\left(\bar{l}_1 - \frac{4}{3}\right)(s-2m_\pi^2)^2 + \left(\bar{l}_2 - \frac{5}{6}\right)\left[s^2 + (t-u)^2\right] - 12m_\pi^2 s + 15m_\pi^4\right\}. \end{aligned} \tag{3.22}$$

We use the following values for the LECs from Refs.[85, 89, 90],

$$10^3 l_1^r = -3.7 \pm 0.2\;,\; 10^3 l_2^r = 5.0 \pm 0.4\;,\; 10^3 l_3^r = 0.8 \pm 3.8\;,\; 10^3 l_4^r = 6.2 \pm 5.7. \tag{3.23}$$

The renormalization constant is set to the rho meson mass, $\mu = m_\rho \cong 770$ MeV. To obtain phase shifts of the $\pi\pi$-scattering we need to write the amplitudes of Eq.(3.22) in an isospin-angular momentum basis. As discussed previously in Section 3.1, for the reaction $\pi\pi \to \pi\pi$ the isospin values of the pion-pair are $I = 0, 1, 2$. The corresponding isospin amplitudes are given in Eq.(3.14) and we recall them below

$$\begin{aligned} F_0(s,t) =& 3T_s + T_t + T_u, \\ F_1(s,t) =& T_t - T_u, \\ F_2(s,t) =& T_t + T_u, \end{aligned} \tag{3.24}$$

with the Mandelstam variables satisfying $s+t+u = 4m_\pi^2$. The isospin amplitudes can be expanded in partial waves in terms of the total angular momentum (J) as shown in the previous chapter. Since the two pions in the isospin basis are identical, the normalization given in Eq.(2.39) is $N = 2$. Thus, the partial wave amplitude in the s-channel is

$$t_J^I(s) = \frac{1}{2}\int_{-1}^{1} \frac{dz_s}{2} P_J(z_s) F_I(s, t(s, z_s), u(s, z_s)), \tag{3.25}$$

where z_s is the cosine of the scattering angle in the s-channel. The cross-channel variables can be written as

$$\begin{aligned} t(s, z_s) &= -2p^2(s)(1 - z_s), \\ u(s, z_s) &= -2p^2(s)(1 + z_s), \end{aligned} \tag{3.26}$$

with the momentum in the center-of-mass given by $p^2(s) = (s - 4m_\pi^2)/4$. As shown in Eq.(2.45), the partial wave amplitudes can be written as a function of a phase shift (δ_J^I),

$$t_J^I(s) = \frac{\eta_J^I(s) e^{2i\delta_J^I} - 1}{2i\sigma(s)}, \tag{3.27}$$

where for low energies we consider the inelastic factor $\eta_J^I(s) = 1$ and

$$\sigma(s) = \frac{1}{16\pi}\sqrt{1 - \frac{4m_\pi^2}{s}} = \frac{1}{8\pi}\frac{p(s)}{\sqrt{s}}. \tag{3.28}$$

We can calculate then the $\pi\pi$ phase shift using the mIAM in Eq.(3.15) for S-wave with isospin 0 and 2 and P-wave with isospin 1 to demonstrate how efficient the IAM formalism works for low energies. One can see in Fig.3.1 that the mIAM curve (black line) describes the experimental phase shift (blue dots) for the low energy region very well. The red dotted line shows the Roy equation analysis, which is a dispersive formalism that describes the $\pi\pi$ scattering [91].

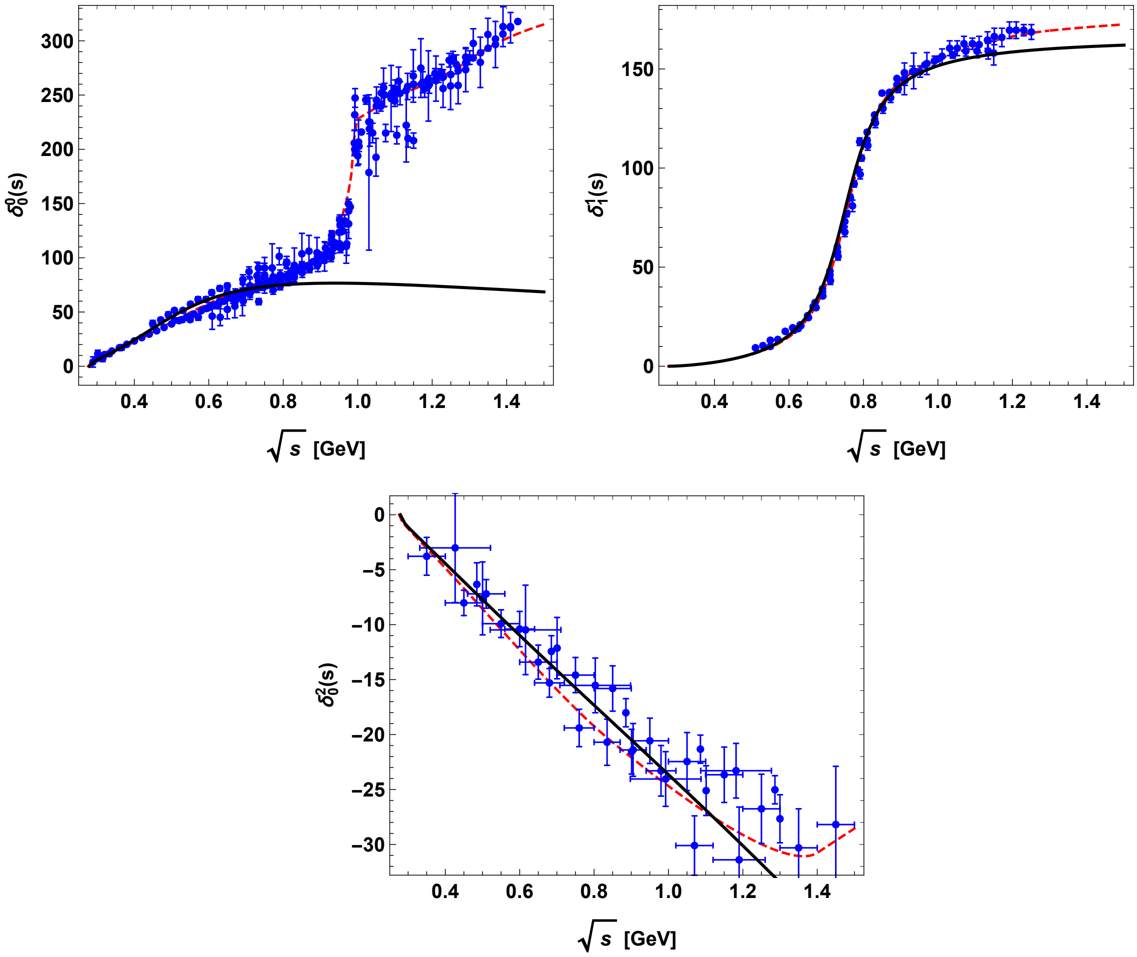

FIGURE 3.1: The $\pi\pi$ phase shift δ_0^0, δ_1^1 and δ_0^2, respectively. The red dotted line is the Roy equation analysis [91], the solid black line is the phase shift from the modified IAM [92].

3.3 Single-Channel Omnès Function for $\pi\pi$

As discussed in the previous chapter, the Omnès function (Eq.(2.72)) encodes the $\pi\pi$ rescattering when its input is the $\pi\pi$ phase shift

$$\Omega_J^I(s) = \exp\left(\frac{s}{\pi}\int_{4m_\pi^2}^{\infty}\frac{ds'}{s'}\frac{\delta_J^I(s')}{s'-s}\right) . \tag{3.29}$$

Now, we focus our attention on the S-wave $I = 0$ phase shift δ_0^0, shown on the top left panel in Fig.3.1. For the single channel case, where the physical region is below the $K\bar{K}$-threshold, $\sqrt{s} < m_{K\bar{K}} \simeq 1$ GeV, we only consider elastic unitarity, which is essentially exact in the physical regions of all Dalitz plot projections. In the previous Section 3.2, we calculated the phase shift $\delta_0^0(s)$ using the single-channel mIAM [92].

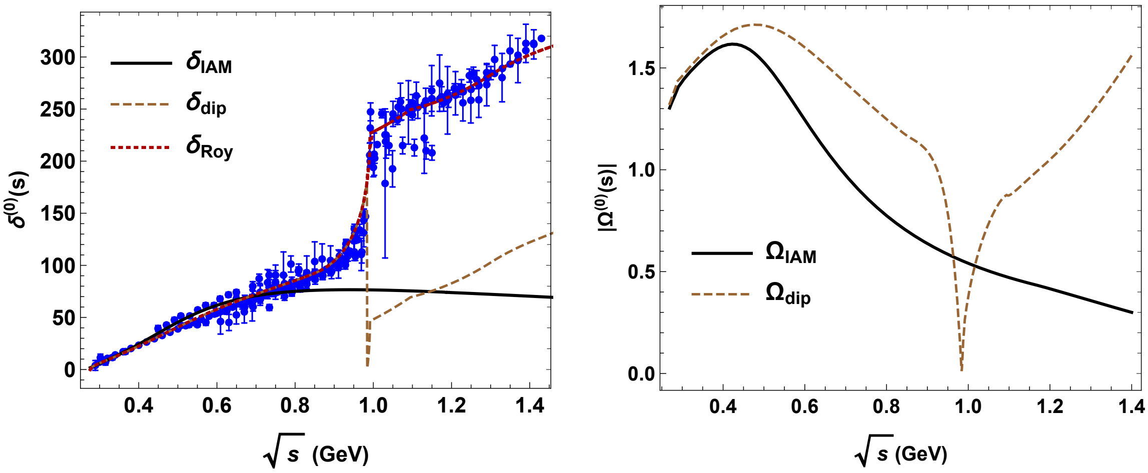

FIGURE 3.2: The left panel shows the experimental data on the $\pi\pi$ phase shift for the S-wave, $I = 0$ in comparison with the Roy equation analysis (red dotted line) [91], the modified phase shift which exhibit a sharp "dip" like behaviour at the point where phase shift crosses π (dashed brown line) [76, 95] and the phase shift from the modified IAM (solid black line) [92]. The respective module of the Omnès functions are shown on the right panel for δ_{dip} and δ_{IAM}.

This result matches with the one shown in Refs.[93, 94]. The benefit of this approach is twofold. First, it reproduces the $f_0(500)$ parameters (such as pole and coupling) consistent with the Roy equation solutions [91]. Second, there is no sharp onset of $K\bar{K}$ inelasticity due to the $f_0(980)$ resonance. The latter requires a coupled-channel treatment with inclusion of $K\bar{K}$ intermediate states, which will be discussed in the next Section 3.4. Alternatively to the input from the mIAM, in the elastic approximation one can construct a modified Omnès function with a phase which exhibits a sharp "dip" behaviour at the two-kaon threshold [76, 95], which is equivalent to setting the phase shift to zero when it is equal to π.

The impact on the Omnès function is shown in Fig.3.2. We observe that both approaches lead to similar results only at very low energies. Whereas at larger energies, the solution based on the "dip" like phase shift exhibits a cusp across the inelastic region, while the Omnès function based solution of the mIAM phase shift is completely smooth. Therefore, we find the mIAM input to be more suitable for the dispersive formalism with elastic unitarity.

In this thesis we also use the Omnès function for the D-wave ($I = 0$), which is constructed directly from the $\pi\pi$ phase shift [91], since the inelasticity around the $f_2(1270)$

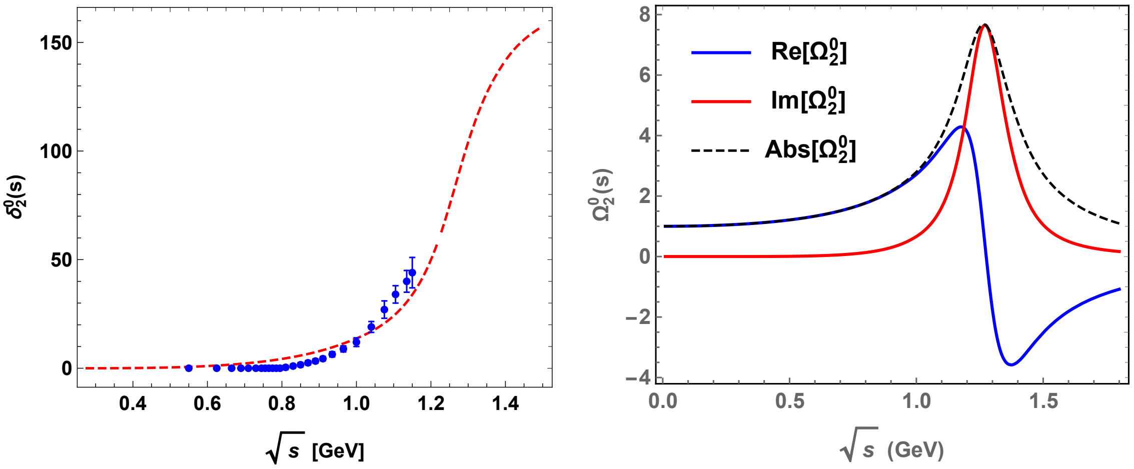

FIGURE 3.3: The left panel shows the experimental data on the $\pi\pi$ phase shift for the D-wave, $I = 0$ in comparison with the Roy equation analysis (red dotted line) [91]. The right panel shows the real part (blue curve), imaginary part (red curve) and absolute value (dashed curve) of the respective Omnès function.

peak is suppressed [37]. The real part, imaginary part and absolute value of the D-wave Omnès function are displayed in Fig.3.3.

3.4 Coupled-Channel Rescattering

For the S-wave isospin $I = 0$ case, when the physical region extends above the two-kaon threshold $s > m_{K\bar{K}}^2$, the pions and kaons are entangled and we need to consider both together in a coupled-channel formalism, as mentioned in Section 2.4. The partial wave expansion in Eq.(2.37) for the scattering of pions and kaons becomes

$$T_{ij}(s,t) = N_{ij} \sum_{J=0}^{\infty} (2J+1) P_J(\cos\theta_s) t_{ij}^J(s), \tag{3.30}$$

where the indices i and j refer to the initial and final state, respectively. The normalization N_{ij} ensures the unitarity for identical particles,

$$N_{\pi\pi,\pi\pi} = 2, \quad N_{\pi\pi,K\bar{K}} = \sqrt{2}, \quad N_{K\bar{K},K\bar{K}} = N_{\pi K,\pi K} = 1. \tag{3.31}$$

Therefore, the matrix in Eq.(2.51) for the S-wave ($J = 0$) scattering of pions and kaons can be expressed as

$$t(s) = \begin{bmatrix} \frac{\eta(s)e^{2i\delta_{\alpha,\alpha}(s)}-1}{2i\sigma_\alpha(s)} & |t_{\alpha,\beta}|e^{\delta_{\alpha,\beta}} \\ |t_{\beta,\alpha}|e^{\delta_{\beta,\alpha}} & \frac{\eta(s)e^{2i\delta_{\beta,\beta}(s)}-1}{2i\sigma_\beta(s)} \end{bmatrix}, \tag{3.32}$$

where $\alpha = \pi\pi$ and $\beta = K\bar{K}$. The inelasticity is given by

$$\eta(s) = \sqrt{1 - 4\sigma_\alpha\sigma_\beta|t_{\alpha,\beta}|} \tag{3.33}$$

and the phase space factor (σ_i) can be expressed using the CM momentum of the two mesons ($p_i(s)$),

$$\sigma_i = \frac{p_i(s)}{8\pi\sqrt{s}}\,\theta(s - s_i), \tag{3.34}$$

where i stands either for α or β and s_i for the respective threshold. Notice that because of the Watson's theorem we can express the phase shift $\delta_{\alpha,\beta}$ in terms of $\delta_{\alpha,\alpha}$ and $\delta_{\beta,\beta}$, as following

$$\delta_{\alpha,\beta} = \delta_{\alpha,\alpha} + \delta_{\beta,\beta}\,\theta(s - s_\beta), \tag{3.35}$$

where $s_\beta = 4m_k^2$. Consequently the Omnès function is also expressed in matrix form

$$\Omega_0^0(s) = \begin{bmatrix} \Omega_{\alpha,\alpha} & \Omega_{\alpha,\beta} \\ \Omega_{\beta,\alpha} & \Omega_{\beta,\beta} \end{bmatrix}, \tag{3.36}$$

where the real, imaginary and absolute values of the matrix elements we use in this thesis are shown in Fig.3.4. In order to describe the $f_0(980)$ properly, which shows up near to the $K\bar{K}$-threshold, the coupled-channel Omnès incorporates the dynamics of the $\pi\pi$ and $K\bar{K}$ scattering simultaneously. One can only obtain the $\Omega_0^0(s)$ numerically, since in contrast to the single-channel case, there is no analytic representation.

In our case, we use the coupled-channel Omnès function calculated numerically according to Ref.[96]. The authors use a data-driven approach based on a dispersive summation scheme [97, 98] which implements constraints from analyticity and unitarity. The method uses the N/D ansatz [99], which separates the contributions of the

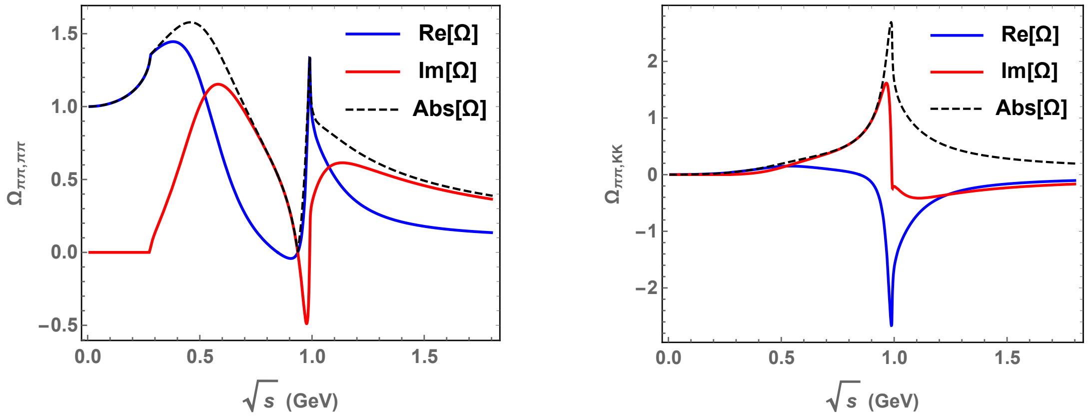

(A) $\pi\pi \to \pi\pi$

(B) $\pi\pi \to KK$

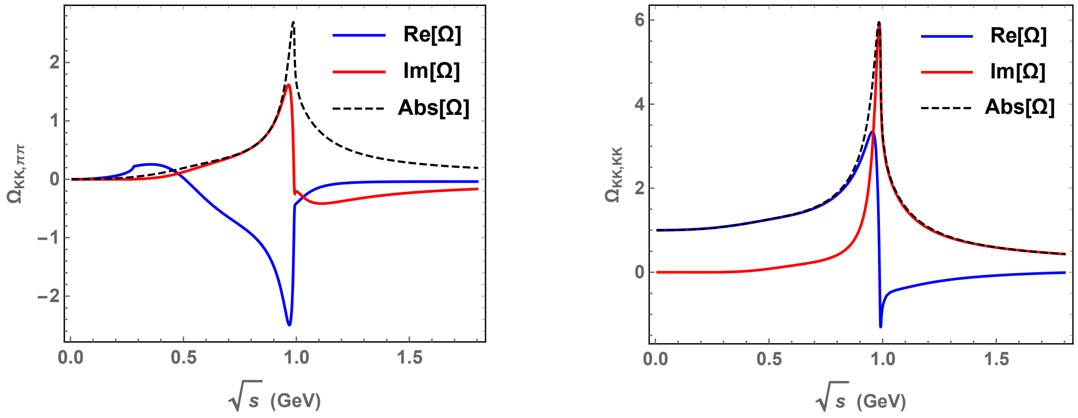

(C) $KK \to \pi\pi$

(D) $KK \to KK$

FIGURE 3.4: The elements of the coupled-channel Omnès function.

left- ($N(s)$) and right-hand ($D(s)$) cuts,

$$t_{ij} = \sum_k D^{-1}_{ik}(s) N_{kj}(s). \tag{3.37}$$

A dispersive representation of the function D can be expressed using the discontinuity along the right-hand cut,

$$D_{ij}(s) = \delta_{ij} - \frac{s}{\pi} \int\limits_{s_{th}}^{\infty} \frac{ds'}{s'} \frac{N_{ij}(s')\sigma_j(s')}{s - s'}. \tag{3.38}$$

The function N can be obtained by writing a once-subtracted DR for

$$\sum_k D_{ik}(s)(t(s) - U(s))_{kj}, \tag{3.39}$$

U_{ij}	$\sqrt{s_E}$ (MeV)	C_0	C_1	C_2	C_3
$U_{11}(s)$	740	17.1(9)	52.1(2.0)	51.1(2.2)	17.2(3.6)
$U_{12}(s)$	740	11.2(1.2)	12.6(2.5)	$\cdots$	$\cdots$
$U_{22}(s)$	1095	70.0(6.5)	−216.2(58.0)	321.0(53.9)	$\cdots$

Table 3.1: Fit parameters C_n determined directly from experimental data and Roy-analyses in a couple-channel formalism from Ref.[96].

where the subtraction constant can be fixed by imposing $t_{ij}(0) = U_{ij}(0)$,

$$N_{ij}(s) = U_{ij}(s) + \frac{s}{\pi}\sum_k \int_{s_{th}}^{\infty} \frac{ds'}{s'} \frac{N_{ik}(s')\sigma_k(s')(U_{kj}(s') - U_{kj}(s))}{s - s'}. \tag{3.40}$$

The function $N(s)$ is expressed in a set of coupled-channel integral equations, which can be computed numerically for a given input $U(s)$. The function $U(s)$ incorporates the contributions of the left-hand cuts combined with subtraction constants from the dispersive integral. The input from the left-hand cuts is parametrized in a model-independent form as an expansion in a suitably constructed conformal mapping variable,

$$U(s) = \sum_{n=0}^{\infty} C_n \xi^n(s), \tag{3.41}$$

where the coefficients C_n can in principle be matched to ChPT at low energy [100]. The function $\xi(s)$ is defined in terms of the point around which the series is expanded (s_E) and the nearest left-hand cut branching point (s_L), thus it is reaction dependent. In the case of the scattering of pions and kaons, the analytic expressions for $\xi(s)$, according to Ref.[96], can be written as

$$\xi(s) = \frac{\sqrt{s - s_L} - \sqrt{s_E - s_L}}{\sqrt{s - s_L} + \sqrt{s_E - s_L}}, \tag{3.42}$$

where the left-hand cuts lie on the real axis and are given by

$$s_L(\pi\pi \to \pi\pi) = s_L(\pi\pi \to K\bar{K}) = 0, \quad s_L(K\bar{K} \to K\bar{K}) = 4(m_K^2 - m_\pi^2). \tag{3.43}$$

The coefficients C_n were determined directly from fitting to Roy analyses for $\pi\pi \to \pi\pi$ [91], $\pi\pi \to K\bar{K}$ [101, 102] and the existing experimental data for these channels (see

Table 3.1). Finally, the Omnès function is obtained from the inverse of the D-function,

$$\Omega_{ij}(s) = D_{ij}^{-1}(s). \tag{3.44}$$

This approach has already been successfully applied for the photon-fusion reactions $\gamma^{(*)}\gamma^{(*)} \to \pi\pi$ in [103–105]. This coupled-channel Omnès function is used to describe the final state interaction of pions and kaons in the reaction $e^+e^- \to J/\psi\,\pi^+\pi^-$ discussed in Chapter 6.

Chapter 4

Kinematics and Observables

In this thesis we analyze three different reactions, $e^+e^- \to \psi(2S)\ \pi^+\pi^-$ (Chapter 5) and $e^+e^- \to J/\psi\ \pi^+\pi^-$ (Chapter 6) and $e^+e^- \to h_c\ \pi^+\pi^-$ (Chapter 7). All these reactions have in common that the initial state consists of an electron-positron pair while the final state consists of two pions and a hidden-charm meson. Therefore, in this chapter we will derive the cross section for these processes and have a closer look at their kinematics. The particular helicity amplitude structures will be detailed in the corresponding chapter for each reaction.

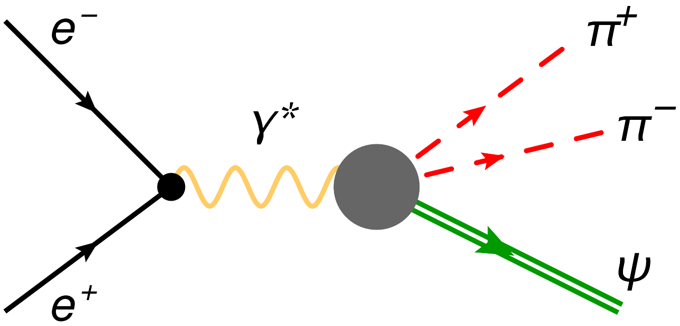

FIGURE 4.1: Diagrammatic representation of the process $e^-(p_a)\,e^+(p_b) \to \gamma^*(p_{\gamma^*}) \to \psi(p_\psi)\,\pi^+(p_{\pi^+})\,\pi^-(p_{\pi^-})$, where $\psi = \psi(2S)$, J/ψ or h_c.

4.1 Cross Section for $e^-\,e^+ \to (c\bar{c}\,) + \pi^+ + \pi^-$

We consider a process with two initial particles with momenta p_a and p_b going to a three-body final state with p_1, p_2 and p_3. First, we derive a general formula for the cross section of this process and later we will adjust the labelling of the momenta to the case at hand for easy identification of the particles. As shown in Fig.4.1, the physical process can be disentangled into two amplitudes, the electron-positron annihilation into a virtual photon and the decay of the virtual photon into the 3-body final state, connected by the virtual photon propagator. Thus, it is convenient to represent the differential cross section in the center of mass frame (CM-frame) of the initial particles

$$d\sigma = \frac{(2\pi)^4}{4q\,|\vec{p}_a|}|\mathcal{H}_{tot}|^2 d\Phi(p_a+p_b;p_1,p_2,p_3)\,. \tag{4.1}$$

The CM-momenta of the initial particles are given by

$$|\vec{p}_a| = |\vec{p}_b| = \frac{1}{2q}\sqrt{[q^2-(m_a+m_b)^2]\cdot[q^2-(m_a-m_b)^2]} \tag{4.2}$$

and q is the e^+e^- CM energy, which is also equal to the energy of the virtual photon

$$q = E_a + E_b. \tag{4.3}$$

Electrons and positrons have the same mass $m_a = m_b = m_e$, therefore the momenta in Eq.(4.2) reduce to

$$|\vec{p}_a| = |\vec{p}_b| = \frac{1}{2}\sqrt{q^2-4m_e^2}\,. \tag{4.4}$$

Consequently, the differential cross section can be rewritten in terms of the virtual photon energy and the electron mass

$$d\sigma = \frac{(2\pi)^4}{2q\sqrt{q^2-4m_e^2}}|\mathcal{H}_{tot}|^2 d\Phi(p_a+p_b;p_1,p_2,p_3)\,. \tag{4.5}$$

The 3-body phase space is defined as

$$\begin{aligned} &d\Phi(p_a+p_b;p_1,p_2,p_3) \equiv d\Phi_3 \\ &= \delta^{(4)}(p_a+p_b-p_1-p_2-p_3)\frac{d^3p_1}{(2\pi)^3 2E_1}\frac{d^3p_2}{(2\pi)^3 2E_2}\frac{d^3p_3}{(2\pi)^3 2E_3}\,, \end{aligned} \tag{4.6}$$

where the conservation of momenta represented by the $\delta^{(4)}$ can be expressed as

$$\delta^{(4)}(p_a+p_b-p_1-p_2-p_3) = \delta^{(3)}(\vec{p}_1+\vec{p}_2+\vec{p}_3)\,\delta^{(0)}(q-E_1-E_2-E_3)\,. \tag{4.7}$$

In Appendix C we show that the 3-body phase space can be rewritten as follows

$$d\Phi_3 = \frac{ds\; dt\; d\cos\theta_s\; d\phi_{23}}{2^5 (2\pi)^8\; q^2} = \frac{ds\; dt\; d\cos\theta_t\; d\phi_{31}}{2^5 (2\pi)^8\; q^2} = \frac{ds\; du\; d\cos\theta_u\; d\phi_{12}}{2^5 (2\pi)^8\; q^2}\,, \tag{4.8}$$

where (θ_s, ϕ_{23}), (θ_t, ϕ_{31}) and (θ_u, ϕ_{12}) are the polar and azimuthal angles related to the s-, t- and u-channel, respectively. The Mandelstam variables are defined as

$$s \equiv (p_2 + p_3)^2 = (q - p_1)^2\,, \tag{4.9}$$

$$t \equiv (p_3 + p_1)^2 = (q - p_2)^2\,, \tag{4.10}$$

$$u \equiv (p_1 + p_2)^2 = (q - p_3)^2\,, \tag{4.11}$$

$$s + t + u = q^2 + p_1^2 + p_2^2 + p_3^2. \tag{4.12}$$

In this thesis we consider the rescattering of pions in the s-channel and the exchange of charged intermediate states in the t- and u-channels. Thus, it is convenient to choose the angles either in the t- or u-channels. For the angles in the t-channel, the differential cross section is obtained when the expression (4.8) is introduced into the Eq.(4.5)

$$\frac{d\sigma}{ds\, dt\, d\cos\theta_t\, d\phi_{31}} = \frac{1}{2^6 (2\pi)^4} \frac{|\mathcal{H}_{tot}|^2}{q^3 \sqrt{q^2 - 4m_e^2}}\,. \tag{4.13}$$

Note that as discussed in Section 2 and given by Eq.(2.18) the cross section for a scattering process 2 → 3 is expressed in terms of five independent kinematic variables. However, since we have azimuthal symmetry around the e^+e^--CM direction, we are left with only four variables, which are two Mandelstam variables and two independent angles.

We want to explicitly split out the electron-positron annihilation, which creates a virtual photon, because it is the same for all the considered processes. On the other hand, the transition $\gamma^*(p_{\gamma^*}) \to \psi(p_\psi)\,\pi^+(p_{\pi^+})\,\pi^-(p_{\pi^-})$ is case dependent and it is analyzed individually later on in this thesis.

The helicity amplitude in Fig.4.1 becomes

$$\mathcal{H}_{\text{tot}} = \mathcal{H}^{\mu}_{ee\gamma^*}\, \frac{(p_{\gamma^*})_\mu (p_{\gamma^*})_\nu / q^2 - g_{\mu\nu}}{q^2}\, \mathcal{H}^{\nu\beta}_{\gamma^*\psi\pi\pi}\, \epsilon^*_\beta(p_\psi, \lambda_\psi)\,, \tag{4.14}$$

where $q^2 = p^2_{\gamma^*}$ and we rewrite the numerator of the propagator as the sum of the polarization vectors of γ^*,

$$\mathcal{H}_{\text{tot}} = \mathcal{H}^{\mu}_{ee\gamma^*} \sum_{\lambda_{\gamma^*}} \frac{\epsilon^*_\mu(p_{\gamma^*}, \lambda_{\gamma^*})\epsilon_\nu(p_{\gamma^*}, \lambda_{\gamma^*})}{q^2} \mathcal{H}^{\nu\beta}_{\gamma^*\psi\pi\pi}\, \epsilon^*_\beta(p_\psi, \lambda_\psi)\,, \tag{4.15}$$

$$\mathcal{H}_{\text{tot}} = \sum_{\lambda_{\gamma^*}} \underbrace{\mathcal{H}^{\mu}_{ee\gamma^*}\, \epsilon^*_\mu(p_{\gamma^*}, \lambda_{\gamma^*})}_{\text{Relativistic Inv.}} \frac{1}{q^2} \underbrace{\epsilon_\nu(p_{\gamma^*}, \lambda_{\gamma^*})\mathcal{H}^{\nu\beta}_{\gamma^*\psi\pi\pi}\, \epsilon^*_\beta(p_\psi, \lambda_\psi)}_{\text{Relativistic Inv.}}\,. \tag{4.16}$$

Notice that now the amplitude $\mathcal{H}_{\text{tot}}$ (4.16) is written in terms of two relativistic invariant terms, which can be treated separately using different frames.

$e^+e^- \to \gamma^*$

In this subsection we analyze the first term of Eq.(4.16), which corresponds to the electron-positron annihilation that creates the off-shell photon

$$\mathcal{H}^{\mu}_{ee\gamma^*}\, \epsilon^*_\mu(q, \lambda_{\gamma^*}) = e\, \bar{v}(p_a, s_a)\gamma^\mu u(p_b, s_b)\, \epsilon^*_\mu(q, \lambda_{\gamma^*}) \equiv \mathcal{H}_{ee\gamma^*}(s_a, s_b, \lambda_{\gamma^*})\,. \tag{4.17}$$

The Dirac spinors u and v are given by

$$u(\vec{p}, 1/2) = \sqrt{p^0 + m_e}\begin{pmatrix} 1 \\ 0 \\ \frac{p_z}{p^0+m_e} \\ \frac{p_x+ip_y}{p^0+m_e} \end{pmatrix}, \qquad u(\vec{p}, -1/2) = \sqrt{p^0 + m_e}\begin{pmatrix} 0 \\ 1 \\ \frac{p_x-ip_y}{p^0+m_e} \\ -\frac{p_z}{p^0+m_e} \end{pmatrix}, \tag{4.18}$$

$$v(\vec{p}, 1/2) = \sqrt{p^0 + m_e}\begin{pmatrix} \frac{p_x-ip_y}{p^0+m_e} \\ -\frac{p_z}{p^0+m_e} \\ 0 \\ 1 \end{pmatrix}, \qquad v(\vec{p}, -1/2) = -\sqrt{p^0 + m_e}\begin{pmatrix} \frac{p_z}{p^0+m_e} \\ \frac{p_x+ip_y}{p^0+m_e} \\ 1 \\ 0 \end{pmatrix}. \tag{4.19}$$

The polarization vector in the CM-frame is given by

$$\epsilon(p_{\gamma^*}, 0) = \begin{pmatrix} 0 \\ 0 \\ 0 \\ 1 \end{pmatrix}, \qquad \epsilon(p_{\gamma^*}, \pm) = \frac{1}{\sqrt{2}}\begin{pmatrix} 0 \\ \mp 1 \\ -i \\ 0 \end{pmatrix}. \tag{4.20}$$

Furthermore, the momentum of e^+ (e^-) in the CM-frame is

$$p^0 = \frac{q}{2} \qquad |\vec{p}| = \frac{1}{2}\sqrt{q^2 - 4m_e^2}. \tag{4.21}$$

In this way, we obtain the following helicity amplitudes

$$|\mathcal{H}_{ee\gamma^*}(\pm 1/2, \pm 1/2, \pm 1)|^2 = 2q^2\, e^2 \quad \text{and} \quad |\mathcal{H}_{ee\gamma^*}(\pm 1/2, \mp 1/2, 0)|^2 = 4m_e^2\, e^2 \tag{4.22}$$

where $\lambda_{\gamma^*} = s_a + s_b$.

4.2 Unpolarized Cross Section

For unpolarized e^+e^- beams and unpolarized targets, we average over the electron and positron spins and sum over polarizations of the final particles. Thus, the unpolarized amplitude squared is given by the square of Eq.(4.16) as follows

$$\begin{aligned} |\mathcal{H}_{\text{tot}}|^2 =& \frac{1}{4}\sum_{s_a s_b}\sum_{\lambda_{\gamma^*}\lambda_\psi}\left[\mathcal{H}^{\mu}_{ee\gamma^*}\, \epsilon^*_\mu(p_{\gamma^*}, \lambda_{\gamma^*})\mathcal{H}^{*\,\mu'}_{ee\gamma^*}\, \epsilon_{\mu'}(p_{\gamma^*}, \lambda_{\gamma^*})\right] \\ & \times\frac{1}{q^4}\cdot\left[\epsilon_\nu(p_{\gamma^*}, \lambda_{\gamma^*})\mathcal{H}^{\nu\beta}_{\gamma^*\psi\pi\pi}\, \epsilon^*_\beta(p_\psi, \lambda_\psi)\epsilon^*_{\nu'}(p_{\gamma^*}, \lambda_{\gamma^*})\mathcal{H}^{*\,\nu'\beta'}_{\gamma^*\psi\pi\pi}\, \epsilon_{\beta'}(p_\psi, \lambda_\psi)\right], \end{aligned} \tag{4.23}$$

where we considered $\lambda_{\gamma^*} = \lambda'_{\gamma^*} = s_a + s_b$. The expression above can be simplified as

$$|\mathcal{H}_{\text{tot}}|^2 = \frac{2}{4}\sum_{\lambda_{\gamma^*}\lambda_\psi}\left[|\mathcal{H}_{ee\gamma^*}(\lambda_{\gamma^*})|^2\, \frac{1}{q^4}\, |\mathcal{H}_{\gamma^*\psi\pi\pi}(\lambda_{\gamma^*}, \lambda_\psi)|^2\right]. \tag{4.24}$$

Using the helicity amplitudes derived in Eq.(4.22), we obtain

$$\begin{aligned} |\mathcal{H}_{\text{tot}}|^2 =& \frac{2}{4}\sum_{\lambda_{\gamma^*}\lambda_\psi}\left[|\mathcal{H}_{ee\gamma^*}(\lambda_{\gamma^*})|^2\, \frac{1}{q^4}\, |\mathcal{H}_{\gamma^*\psi\pi\pi}(\lambda_{\gamma^*}, \lambda_\psi)|^2\right] \\ =& \frac{e^2}{q^2}\sum_{\lambda_\psi}\left[|\mathcal{H}_{\gamma^*\psi\pi\pi}(+1, \lambda_\psi)|^2 + \frac{2m_e^2}{q^2}\, |\mathcal{H}_{\gamma^*\psi\pi\pi}(0, \lambda_\psi)|^2\right]. \end{aligned} \tag{4.25}$$

Notice that due to parity the modulus of the helicity amplitudes for $\lambda_{\gamma^*} = +1$ and $\lambda_{\gamma^*} = -1$ is equal

$$|\mathcal{H}_{\gamma^*\psi\pi\pi}(+1, \lambda_\psi)| = |\mathcal{H}_{\gamma^*\psi\pi\pi}(-1, \lambda_\psi)|\,. \tag{4.26}$$

Moreover, since $q^2 > (4 \text{ GeV})^2 \gg m_e^2 \approx (0.5 \text{ MeV})^2$, we can consider the limit of $m_e^2 \to 0$ and thus disregard the second term in Eq.(4.26) with $\lambda_{\gamma^*} = 0$. Therefore the differential cross section becomes

$$\frac{d\sigma}{ds\, dt\, d\cos\theta_t\, d\phi_{31}} = \frac{e^2}{2^6 (2\pi)^4\, q^6} \left[\sum_{\lambda_\psi} |\mathcal{H}_{\gamma^* \psi\pi\pi}(+1, \lambda_\psi)|^2 \right]. \tag{4.27}$$

In Section 2.9 we showed that the helicity amplitude in Eq.(4.27) can be derived in terms of sequential two-body decays. Recalling Eq.(2.112) below and relabelling it accordingly, we can write

$$\mathcal{H}_{\gamma^* \psi\pi\pi}(\lambda_{\gamma^*}, \lambda_\psi) \equiv H^{1\, \lambda_{\gamma^*}}_{\lambda_\psi}(s, t, \cos\theta_s, \phi_{23}) = \sum_{\bar{\lambda}} D^{1\, *}_{\lambda_{\gamma^*} \bar{\lambda}}(0, \theta_s, \phi_{23})\, H_{\bar{\lambda}\, \lambda_\psi}(s, t), \tag{4.28}$$

where we relabelled $M \to \lambda_{\gamma^*}$ and $\lambda_1 \to \lambda_\psi$. Notice that the angular part is factored out in the Wigner D-function and the term $H_{\bar{\lambda}\, \lambda_\psi}(s, t)$ depends only on the Mandelstam variables s and t. We can also use a similar relation as shown in Eq.(2.110) to express the angles in the s-channel $(\phi_s, \theta_s, \phi_{23})$ in terms of the angles in the t-channel $(\phi_t, \theta_t, \phi_{31})$ by using the following expression,

$$D^{J\, *}_{\lambda_{\gamma^*} \bar{\lambda}}(\phi_s, \theta_s, \phi_{23}) = \sum_{\nu} D^{J\, *}_{\lambda_{\gamma^*} \nu}(\phi_t, \theta_t, \phi_{31})\, d^J_{\nu \bar{\lambda}}(\bar{\theta}_{st}), \tag{4.29}$$

where $\bar{\theta}_{st}$ is the reverse rotation of $\bar{\theta}_{ts}$, that is $\bar{\theta}_{st} = -\bar{\theta}_{ts}$, which is given in Appendix D. Therefore, the helicity amplitude in Eq.(4.28) becomes

$$H^{1\, \lambda_{\gamma^*}}_{\lambda_\psi}(s, t, \cos\theta_t, \phi_{31}) = \sum_{\bar{\lambda}} \sum_{\nu} D^{1\, *}_{\lambda_{\gamma^*} \nu}(\phi_t, \theta_t, \theta_{31})\, d^1_{\nu \bar{\lambda}}(\bar{\theta}_{st})\, H_{\bar{\lambda}\, \lambda_\psi}(s, t). \tag{4.30}$$

In order to obtain the invariant mass distributions ($d\sigma/ds$ and $d\sigma/dt$), we need to integrate the differential cross section in Eq.(4.27) over the angles ϕ_{31} and $d\cos\theta_t$,

$$\begin{aligned} &\int_{-1}^{+1} \mathrm{d}\cos\theta_t \int_0^{2\pi} d\phi_{31} |H_{M\lambda_\psi}(s, t, \cos\theta_t, \phi_{31})|^2 = \\ &\int_{-1}^{+1} \mathrm{d}\cos\theta_s \int_0^{2\pi} d\phi_{23} |H_{M\lambda_\psi}(s, t, \cos\theta_s, \phi_{23})|^2 = \sum_{\bar{\lambda}} \frac{4\pi}{3} |H_{\bar{\lambda}\, \lambda_\psi}(s, t)|^2, \end{aligned} \tag{4.31}$$

where we used the following orthogonality relations of the Wigner D-functions,

$$\int_0^{2\pi} d\alpha \int_{-1}^{+1} d\cos\beta \int_0^{2\pi} d\gamma\, D^{j'}_{m'k'}(\alpha,\beta,\gamma) D^{j\,*}_{mk}(\alpha,\beta,\gamma) = \frac{8\pi^2}{2j+1}\delta_{m'm}\delta_{k'k}\delta_{j'j}. \tag{4.32}$$

Furthermore, we considered that the Wigner rotation matrices are unitary,

$$\sum_m D^{j}_{mk'}(\alpha,\beta,\gamma) D^{j\,*}_{mk}(\alpha,\beta,\gamma) = \delta_{k'k}. \tag{4.33}$$

Therefore, after performing the angular integrals the differential cross section becomes

$$\frac{d\sigma}{ds\,dt} = \frac{e^2}{2^5(2\pi)^3\,q^6}\frac{1}{3}\left[\sum_{\bar\lambda\,\lambda_\psi} |H_{\bar\lambda\,\lambda_\psi}(s,t)|^2\right]. \tag{4.34}$$

The double differential cross section in Eq.(4.34) has the same analytical form as the one for a simple 3-body decay without considering the production process. This indicates that by integrating over the angular variables the information about the production mechanism is lost. Notice that the quantity in square brackets in Eq.(4.34) is Lorentz invariant, which means that we can calculate it in any frame. For convenience, in the next chapters we calculate it in the $\pi\pi$-CM with the momenta of ψ and γ^* travelling towards the positive direction of the z-axis. This requires the following simple change $\bar\lambda = \lambda_1$ and $\lambda_\psi = -\lambda_2$, since in the derivation of the sequential decays the momenta of particle corresponding to ψ was defined travelling towards the negative direction of the z-axis 2.9.

Chapter 5

$e^+e^- \to \psi(2S)\,\pi^+\pi^-$

The reaction $e^+e^- \to \pi^+\pi^-\psi(2S)$ was first measured by the Belle collaboration using the initial state radiation technique [106, 107]. A clear evidence of a charged intermediate state at 4.05 GeV was detected in the $\psi\pi^\pm$ invariant mass distribution. Recently, the BESIII Collaboration made a high statistics measurement of the same reaction at different e^+e^- CM energies q [108]. At $q = 4.416$ GeV, a peak was also observed in the data, which according to an experimental estimate would correspond to a charged charmonium structure with a mass around 4.032 GeV. However, the total decay width of this new state was not determined due to unresolved discrepancies between the phenomenological fit model and the data. Moreover, it was noticed that a small variation around e^+e^- center-of-mass (CM) energy $q = 4.226$ GeV could change significantly the line shape of the invariant mass distributions. This calls for a new analysis that can improve the current description for the Dalitz plot projections for all e^+e^- CM energies for this process.

In this chapter, we use the dispersion theory, introduced in Chapter 2, to provide a physical description of recent BESIII data on the reaction $e^+e^- \to \psi(2S)\,\pi^+\,\pi^-$ [108]. Similar approaches have been successful in the literature in recent years, see for instance Refs. [76, 109–112] for different applications. In our analysis, we explicitly take into account the effects of charged exotic intermediate states in the t- and u-channels, which are necessary to explain the sharp peaks in the $\psi\pi$ invariant mass distribution. This assumption also implies that we test whether the intermediate states can be explained as a resonance. In addition, the $\pi\pi$ final state interaction (FSI) is accounted for through a single-channel Omnès formalism which requires the $\pi\pi$ phase shift as input, as discussed in Chapter 3. The theoretical framework for this reaction is explained in detail in Sections 5.1 and 5.2. Within this approach we fit the experimental invariant mass distributions measured by the BESIII Collaboration [108] at four different e^+e^-

CM energies and show our results in Section 5.3. This work led to a publication in Physics Letters B [1].

5.1 Dispersive Formalism

In this section we construct a single-channel dispersive formalism to describe the mass distributions for the $e^+e^- \to \pi^+\pi^-\psi(2S)$ process. Since we need to work in an isospin and angular momentum basis, we first need to investigate the possible quantum numbers in the reaction. Because of charge conjugation and parity conservation in the process $\gamma^*(1^{--}) \to \psi(2S)(1^{--}) + \pi(0^-) + \pi(0^-)$, the $\pi\pi$-system can only take even values of the total angular momentum J and the isospin values $I_{\pi\pi} = 0, 2$. Since the photon can only couple to isoscalars or isovectors and the isospin of $\psi(2S)$ is zero, we conclude that only $I_{\pi\pi} = 0$ is possible. In the following we omit the isospin index for simplicity, keeping in mind that the transformation coefficient between particle and isospin bases can be absorbed in the overall normalization of the Dalitz plot.

Under the assumption that left-hand cuts for the reaction with charged and neutral pions are the same, corresponding to the dominance of Z_c mechanism, the cross section for $e^+e^- \to \psi(2S)\,\pi^0\pi^0$ differs from the one with the charged pions only by the overall symmetry factor of 1/2, as it was indeed observed recently in Ref. [113].

The kinematics for the process $e^-\,e^+ \to \gamma^* \to \psi(2S)\,\pi^+\,\pi^-$ were explained in Chapter 4 and for the cross section we derived the following expression

$$\frac{d^2\sigma}{ds\,dt} = \frac{e^2}{2^5(2\pi)^3\,q^6} \cdot \frac{1}{3}\left[\sum_{\lambda_1\lambda_2} |\mathcal{H}_{\lambda_1\lambda_2}|^2\right]. \tag{5.1}$$

The quantity in the squared brackets in Eq.(5.1) is Lorentz invariant, therefore for convenience in our formalism, we use the kinematics in the CM frame of the two final pions for the helicity amplitude $\mathcal{H}_{\lambda_1\lambda_2}$. Notice that in the $\pi\pi$-CM frame the helicities λ_1 and λ_2 can be interpreted as the helicity of γ^* and $\psi(2S)$, respectively.

We define $z \equiv \cos\theta_s$ as the cosine of the angle between the p_{π^+} and the p_ψ momenta,

$$\begin{aligned} t(s,z) &= \frac{1}{2}(q^2 + m_\psi^2 + 2m_\pi^2 - s) + \frac{k(s)}{2}\,z, \\ u(s,z) &= \frac{1}{2}(q^2 + m_\psi^2 + 2m_\pi^2 - s) - \frac{k(s)}{2}\,z, \end{aligned} \tag{5.2}$$

where

$$k(s) = \frac{1}{s}\sqrt{\lambda(s,q^2,m_\psi^2)\,\lambda(s,m_\pi^2,m_\pi^2)}, \tag{5.3}$$

with $\lambda(a,b,c) = a^2+b^2+c^2-2(ab+bc+ca)$ being the Källen function. Consequently, z can be written in terms of t and u

$$z = \frac{t-u}{k(s)}. \tag{5.4}$$

Similarly as in Eq.(4.12), we choose the Mandelstam variables in terms of the three-body final state

$$\begin{aligned} s &= (p_{\pi^+} + p_{\pi^-})^2 \equiv M_{\pi\pi}^2, \\ t &= (p_\psi + p_{\pi^+})^2 \equiv M_{\psi\pi^+}^2, \\ u &= (p_\psi + p_{\pi^-})^2 \equiv M_{\psi\pi^-}^2, \end{aligned} \tag{5.5}$$

which satisfy $s+t+u = q^2 + m_\psi^2 + 2m_\pi^2$. Consequently, one Mandelstam variables can be expressed in terms of the others.

The helicity amplitude $\mathcal{H}_{\lambda_1\lambda_2}$ contains the physical information of the subprocess $\gamma^* \to \psi(2S)\,\pi^+\pi^-$, necessary to describe the shape of the invariant mass distribution of the reaction. We ignore for now any potential kinematic constraints on the helicity amplitudes. Later in the next section, we show that they happen sufficiently far away from the physical region or are very weak so that their impact on the dispersive integral can be ignored. The expansion of the amplitude in a sum of partial wave series in the s-channel reads

$$\mathcal{H}_{\lambda_1\lambda_2}(s,t,u) = \sum_{J\ \text{even}}^{\infty} (2J+1) h_{\lambda_1\lambda_2}^{(J)}(s)\, d_{\Lambda,0}^{(J)}(\theta_s), \tag{5.6}$$

where $\Lambda = \lambda_1 - \lambda_2$, $d_{\Lambda,0}^{(J)}$ is a Wigner rotation function and θ_s is the scattering angle in the $\pi\pi$-CM frame. The partial wave amplitudes have contributions from the left- and right-hand cut, which can be explicitly separated into two terms,

$$\mathcal{H}_{\lambda_1\lambda_2}(s,t,u) = \sum_{J\ \text{even}}^{\infty} (2J+1) h^{(J),L}_{\lambda_1\lambda_2}(s)\, d^{(J)}_{\Lambda,0}(\theta_s) + \sum_{J\ \text{even}}^{\infty} (2J+1) h^{(J),R}_{\lambda_1\lambda_2}(s)\, d^{(J)}_{\Lambda,0}(\theta_s), \quad (5.7)$$

where the term $h^{(0),L}_{\lambda_1\lambda_2}(s)$ contains the left-hand cuts and the term $h^{(0),R}_{\lambda_1\lambda_2}(s)$ has only right-hand cuts by definition. For s-wave (J=0), the helicity amplitude becomes simply

$$h^{(0)}_{\lambda_1\lambda_2}(s) = h^{(0),L}_{\lambda_1\lambda_2}(s) + h^{(0),R}_{\lambda_1\lambda_2}(s) = \int_L \frac{ds'}{\pi} \frac{\text{Disc}\, h^{(0)}_{\lambda_1\lambda_2}(s')}{s'-s-i\epsilon} + \int_R \frac{ds'}{\pi} \frac{\text{Disc}\, h^{(0)}_{\lambda_1\lambda_2}(s')}{s'-s-i\epsilon}. \quad (5.8)$$

The unitarity equation in the elastic approximation can be written as

$$\begin{aligned} \text{Disc}\, h^{(0)}_{\lambda_1\lambda_2}(s) &\equiv \frac{1}{2\,i}(h^{(0)}_{\lambda_1\lambda_2}(s+i\epsilon) - h^{(0)}_{\lambda_1\lambda_2}(s-i\epsilon)) \\ &= t^{(0)*}(s)\,\rho(s)\, h^{(0)}_{\lambda_1\lambda_2}(s)\,\theta(s>4m_\pi^2), \end{aligned} \quad (5.9)$$

where $t^{(0)}(s)$ is the $\pi\pi$ amplitude, and $\rho(s) = \lambda^{1/2}(s, m_\pi^2, m_\pi^2)/s$ is the phase space factor. The solution of Eq.(5.8) can be written using the Muskhelishvili-Omnès formalism, explained in Section 5.8. As result, we obtain

$$h^{(0),R}_{\lambda_1\lambda_2}(s) = \Omega^{(0)}(s) \left\{ a + bs - \frac{s^2}{\pi} \int_{4m_\pi^2}^{\infty} \frac{ds'}{s'^2} \frac{\text{Disc}\,(\Omega^{(0)}(s'))^{-1}\, h^{(0),L}_{\lambda_1\lambda_2}(s')}{s'-s} \right\}. \quad (5.10)$$

Note that we introduced two subtractions (which are functions of the photon virtuality q^2) in order to reduce the sensitivity to the high energy region and the effects of additional unknown left-hand cuts, such as possible D-meson loops or contact interactions [110, 112]. The final expression for the total helicity amplitude is obtained by using Eq.(5.10) and Eq.(5.7) together,

$$\begin{aligned} \mathcal{H}_{\lambda_1\lambda_2}(s,t,u) = \mathcal{H}^L_{\lambda_1\lambda_2} + \Omega^{(0)}(s) \times& \\ \left\{ a + bs - \frac{s^2}{\pi} \int_{4m_\pi^2}^{\infty} \frac{ds'}{s'^2} \frac{\text{Disc}\,(\Omega^{(0)}(s'))^{-1}\, h^{(0),L}_{\lambda_1\lambda_2}(s')}{s'-s} \right\}&, \end{aligned} \quad (5.11)$$

where

$$\mathcal{H}^{L}_{\lambda_1\lambda_2} = \sum_{J\ \mathrm{even}}^{\infty} (2J+1) h^{(J),L}_{\lambda_1\lambda_2}(s)\, d^{(J)}_{\Lambda,0}(\theta_s) \tag{5.12}$$

Notice that we sum over all possible total angular momenta for the the left-hand cut part of the amplitude, while we include the $\pi\pi$-rescattering in the s-channel only for s-wave in the right-hand part.

5.2 Left-Hand Cuts

5.2.1 Invariant amplitudes and kinematic constraints

In the general form, the hadron tensor $\mathcal{H}^{\mu\nu}$ can be decomposed into a complete set of Lorentz structures as discussed in Refs. [103, 105, 114–118],

$$\mathcal{H}^{\mu\nu} = \sum_{i=1}^{5} F_i L_i^{\mu\nu}, \tag{5.13}$$

where F_i are the invariant amplitudes and $L_i^{\mu\nu}$ are given by

$$L_1^{\mu\nu} = - p^{\nu}_{\gamma^*} p^{\mu}_{\psi} + (p_{\gamma^*} \cdot p_{\psi}) g^{\mu\nu} \tag{5.14}$$

$$\begin{aligned} L_2^{\mu\nu} = &\left[-\Delta^2 (p_{\gamma^*} \cdot p_{\psi}) + 2(p_{\gamma^*} \cdot \Delta)(p_{\psi} \cdot \Delta)\right] g^{\mu\nu} + \Delta^2 p^{\nu}_{\gamma^*} p^{\mu}_{\psi} \\ &+ 2(p_{\gamma^*} \cdot p_{\psi}) \Delta^{\mu}\Delta^{\nu} - 2(p_{\psi} \cdot \Delta) p^{\nu}_{\gamma^*} \Delta^{\mu} - 2(p_{\gamma^*} \cdot \Delta) p^{\mu}_{\psi} \Delta^{\nu} \end{aligned} \tag{5.15}$$

$$\begin{aligned} L_3^{\mu\nu} =&(t-u)\Bigg\{ \left[m_\psi^2 (p_{\gamma^*} \cdot \Delta) + q^2 (p_{\psi} \cdot \Delta)\right] \left(g^{\mu\nu} - \frac{p^{\nu}_{\gamma^*} p^{\mu}_{\psi}}{(p_{\gamma^*} \cdot p_{\psi})}\right) \\ &+ \left(\Delta^{\mu} - \frac{(p_{\gamma^*} \cdot \Delta)}{(p_{\gamma^*} \cdot p_{\psi})} p^{\mu}_{\psi}\right) \left[-m_\psi^2 p^{\nu}_{\gamma^*} + (p_{\gamma^*} \cdot p_{\psi}) p^{\nu}_{\psi}\right] \\ &- \left(\Delta^{\nu} - \frac{(p_{\psi} \cdot \Delta)}{(p_{\gamma^*} \cdot p_{\psi})} p^{\nu}_{\gamma^*}\right) \left[q^2 p^{\mu}_{\psi} - (p_{\gamma^*} \cdot p_{\psi}) p^{\mu}_{\gamma^*}\right] \Bigg\} \end{aligned} \tag{5.16}$$

$$L_4^{\mu\nu} = q^2 m_\psi^2 g^{\mu\nu} + (p_{\gamma^*} \cdot p_{\psi}) p^{\mu}_{\gamma^*} p^{\nu}_{\psi} - q^2 p^{\mu}_{\psi} p^{\nu}_{\psi} - m_\psi^2 p^{\mu}_{\gamma^*} p^{\nu}_{\gamma^*} \tag{5.17}$$

$$L_5^{\mu\nu} = \left(q^2\Delta^\mu - (p_{\gamma^*}\cdot\Delta)p_{\gamma^*}^\mu\right)\left(m_\psi^2\Delta^\nu - (p_\psi\cdot\Delta)p_\psi^\nu\right)\,,$$

where Δ^μ is given by

$$\Delta^\mu = (p_{\pi^+} - p_{\pi^-})^\mu\,. \tag{5.18}$$

For the S-wave, the F_2, F_3 and F_5 functions vanish and F_1 and F_2 can be expressed in terms of $h_{++}^{(0)}$ and $h_{00}^{(0)}$ as

$$\begin{aligned} F_1 &= \frac{4q\,m_\psi\,h_{00}^{(0)}(s) - 2h_{++}^{(0)}(s)(q^2+m_\psi^2-s)}{q^4-2q^2(m_\psi^2+s)+(m_\psi^2-s)^2}\,,\\ F_4 &= \frac{4q\,m_\psi\,h_{++}^{(0)}(s) - 2h_{00}^{(0)}(s)(q^2+m_\psi^2-s)}{q\,m_\psi\,((q-m_\psi)^2+s)((q+m_\psi)^2-s)}\,. \end{aligned} \tag{5.19}$$

Since invariant amplitudes are free from any kinematic singularities by definition, one can conclude that the helicity amplitudes are correlated at the kinematic points $s = (q \pm m_\psi)^2$,

$$h_{++}^{(0)}(s) \pm h_{00}^{(0)}(s) \sim \mathcal{O}(s-(q\pm m_\psi)^2)\,. \tag{5.20}$$

5.2.2 Z_c exchange mechanism

In the dispersive representation given by Eq.(5.11), we approximate the left-hand cut contribution by the exchange of intermediate charmoniumlike charged states in the t and u channels. Based on the experimental data, the mechanism $\gamma^*(q^2) \to \pi + (Z_c \to \psi(2S)+\pi)$ is assumed to be the dominant one. The amplitudes for the process can be written in a general form as

$$\mathcal{H}_{\lambda_1\lambda_2}^{Z_c} = (V_{Z_c\psi\pi})^{\beta\nu}\,S_{\nu\mu}(Q_z)\,(V_{\gamma^*\pi Z_c})^{\mu\alpha}\,\epsilon_\alpha(p_{\gamma^*},\lambda_1)\,\epsilon_\beta^*(p_\psi,\lambda_2), \tag{5.21}$$

where $S_{\nu\mu}(Q_z)$ is the axial meson propagator. We adopt the vertex[1] from [120],

$$(V_{Z_c\psi\pi})^{\beta\nu} = C_{Z_c\psi\pi}\,\left[g^{\beta\nu}\,(p_\psi\cdot Q_z) - p_\psi^\nu Q_z^\beta\right], \tag{5.22}$$

$$(V_{\gamma^*\pi Z_c})^{\mu\alpha} = \mathcal{F}_{\gamma^*\pi Z_c}(q^2)\,\left[g^{\alpha\mu}\,(p_{\gamma^*}\cdot Q_z) - p_{\gamma^*}^\mu Q_z^\alpha\right], \tag{5.23}$$

where $Q_z = (p_{\gamma^*} - p_\pi)$. The form factor $\mathcal{F}_{\gamma^*\pi Z_c}(q^2)$ in Eq.(5.23) has a physical meaning only for the on-shell pion and Z_c meson. Below we will consider only the Z_c pole contribution, which is well in agreement with Eq.(5.23). In our formalism we will perform an independent fit at each e^+e^- CM energy q, without any specific assumptions for $\mathcal{F}_{\gamma^*\pi Z_c}(q^2)$. Having enough such energy values, at which one can perform a detailed fit to the data, allows one in principle to reconstruct the line shape of the $e^+e^- \to \psi(2S)\,\pi^+\pi^-$ process. In such way one can e.g. test if a description in terms of two Breit-Wigner distributions $Y(4220)$ and $Y(4390)$ as in Ref. [108] is an accurate representation of the cross section.

Due to parity, the helicity amplitudes can be reduced from 9 to 5 independent ones: $\mathcal{H}_{++}$, $\mathcal{H}_{+-}$, $\mathcal{H}_{+0}$, $\mathcal{H}_{0+}$ and $\mathcal{H}_{00}$. We observe that $\mathcal{H}_{+-}^{Z_c} = \mathcal{H}_{+0}^{Z_c} = \mathcal{H}_{0+}^{Z_c} \approx 0$ compared to $\mathcal{H}_{++}^{Z_c}$ and $\mathcal{H}_{00}^{Z_c}$, which confirms our assumption that the process is dominated by the S-wave. Also, for our particular kinematics the approximation $|\mathcal{H}_{++}^{Z_c}| \approx |\mathcal{H}_{00}^{Z_c}|$ can be made with less than 1% error in the physical region (similar observations were also made in Refs. [109, 110]). Therefore,

$$\sum_{\lambda_1\lambda_2} |\mathcal{H}_{\lambda_1\lambda_2}^{Z_c}|^2 \approx 2\,|\mathcal{H}_{++}^{Z_c}|^2 + |\mathcal{H}_{00}^{Z_c}|^2 \approx 3\,|\mathcal{H}_{++}^{Z_c}|^2, \tag{5.24}$$

and we can ignore the effects of the kinematical constraints given by Eq.(5.20). The expression of the helicity amplitude $\mathcal{H}_{++}^{Z_c}$ in terms of the invariant amplitudes $F_i^{Z_c}(s,t)$

---

[1] In general there are two vertex structures for the axial-vector-pseudoscalar transition. The different choices used in the literature were e.g. reviewed in Ref.[119]. As we only need the on-shell vertices for our purpose, we can conveniently choose the second vertex structure of the form:

$$(V_{Z_c\psi\pi}^{(2)})^{\beta\nu} = C_2\,p_\pi^\nu\,\left(Q_z^\beta - \frac{p_\psi\cdot Q_z}{p_\psi^2}p_\psi^\beta\right),$$

and an analogous expression for the second $V_{\gamma^*\pi Z_c}^{(2)}$ vertex. We checked that by including the second vertex structures with the same order of magnitude of the couplings, only leads to a very small difference for the total unpolarized result. One reason for the small relative contribution with the above choice of vertex structure 2 is the suppression due to the pion four-momentum. Therefore for the purpose of the unpolarized observable, the use of one effective coupling (vertices in Eq.(5.22) and Eq.(5.23)) can be applied and its value adjusted accordingly.

is given by

$$\begin{aligned}\mathcal{H}^{Z_c}_{++}(s,t) &= \frac{s-q^2-m_\psi^2}{2}\,F_1(s,t) - q^2 m_\psi^2\,F_4(s,t)\\ &+ (t-u)^2\,\frac{s(q^2+m_\psi^2)-(m_\psi^2-q^2)^2}{2\,\lambda(s,q^2,m_\psi^2)}\,F_2(s,t)\\ &+ (t-u)^2\,\frac{q^2+m_\psi^2}{2}\,F_3(s,t)\,,\end{aligned} \tag{5.25}$$

where

$$\begin{aligned}F_1^{Z_c} &= -\frac{\mathcal{F}_{\gamma^*\pi Z}\,C_{Z\psi\pi}}{8}\left(\frac{4\,t+q^2+m_\psi^2}{t-m_Z^2}+\frac{4\,u+q^2+m_\psi^2}{u-m_Z^2}\right),\\ F_2^{Z_c} &= -\frac{\mathcal{F}_{\gamma^*\pi Z}\,C_{Z\psi\pi}}{8}\left(\frac{1}{t-m_Z^2}+\frac{1}{u-m_Z^2}\right),\\ F_3^{Z_c} &= \frac{\mathcal{F}_{\gamma^*\pi Z}\,C_{Z\psi\pi}}{4\,(t-u)}\left(\frac{1}{t-m_Z^2}-\frac{1}{u-m_Z^2}\right),\\ F_4^{Z_c} &= -\frac{\mathcal{F}_{\gamma^*\pi Z}\,C_{Z\psi\pi}}{4}\left(\frac{1}{t-m_Z^2}+\frac{1}{u-m_Z^2}\right),\\ F_5^{Z_c} &= 0\,.\end{aligned} \tag{5.26}$$

Due to the polynomial ambiguity of the p.w. amplitudes, we will consider only the pole contribution. Based on the fixed-s Mandelstam representation one can show that the pole contribution corresponds to fixing $t=m_Z^2$ and $u=m_Z^2$ in the numerators of Eq.(5.26). This procedure is in line with the definition of the on-shell transition form factor $\mathcal{F}_{\gamma^*\pi Z_c}(q^2)$ and does not change the amplitude in the physical region.

5.2.3 Anomalous threshold

Depending on the kinematics of the reaction, left- and right- hand cuts may overlap leading to an additional, anomalous piece in the dispersive integral of Eq.(5.11). The left-hand branch points of partial wave amplitudes Eq.(5.19) can be determined by the endpoint singularities of the t- and u-channel projection integrals

$$L(s) \equiv \int_{-1}^{+1}\frac{dz}{t-m_z^2} = \int_{-1}^{+1}\frac{dz}{u-m_z^2} = -\frac{2}{k(s)}\log\left(\frac{\chi(s)+1}{\chi(s)-1}\right), \tag{5.27}$$

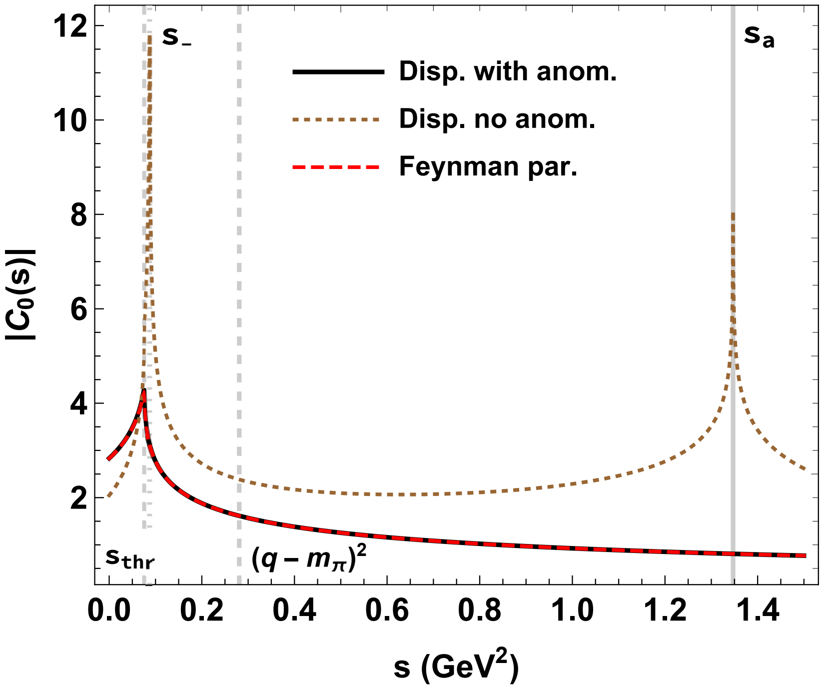

FIGURE 5.1: Comparison of the absolute values of the scalar triangle loop function $C_0(q^2, m_\psi^2, s, m_\pi^2, m_z^2, m_\pi^2)$ calculated numerically using Feynman parameters (dashed red line) and dispersively with (solid black line) or without (dotted brown line) anomaly piece given in Eq.(5.29). The result is illustrated for $q = 4.226$ GeV and $Z_c(3900)$ as intermediate state.

where $\chi(s)$ is given by

$$\chi(s) = \frac{2m_z^2 - q^2 - m_\psi^2 - 2m_\pi^2 + s}{k(s)} \,. \tag{5.28}$$

In this way, we find for the left-hand branch points

$$s_\pm = \frac{1}{2}\left[q^2 + m_\psi^2 + 2m_\pi^2 - m_z^2 - \frac{(q^2 - m_\pi^2)(m_\psi^2 - m_\pi^2)}{m_z^2}\right] \pm \frac{k(m_z^2)}{2\, m_z^2}.$$

When $q^2 > 2m_\pi^2 + 2m_z^2 - m_\psi^2$, the branch point s_- moves from the unphysical (square-root) Riemann sheet onto the physical sheet and requires the proper deformation of the integration contour [121–123] (see also [124] where a general spectral representation is established for the arbitrary masses case). Effectively, it corresponds to including an additional piece to Eq.(5.28), which is related to the discontinuity of $L(s)$ on the anomalous cut

$$L(s) \to L(s) \underbrace{-i\frac{4\,\pi}{k(s)}\,\theta(s_- < s < s_a)}_{\text{anomalous piece}}\,, \tag{5.29}$$

$$s_a = 2m_\pi^2 + m_\psi^2 + q^2 - 2m_z^2\,,$$

and making the analytical continuation $q^2 \to q^2 + i\epsilon$ [76, 125]. The location of s_a is determined by the condition that the imaginary part of $L(s)$ changes sign. To cross-check whether this prescription is correct, we consider a toy model of scalar fields and calculate a triangle loop function. In Fig. 5.1 two results are shown: the direct calculation via Feynman parameters and the result of a dispersive representation. The exact agreement is achieved only when the anomalous piece in Eq.(5.29) is taken into account.

We note, that the considered e^+e^- center-of-mass energies satisfy the condition $q^2 > (m_Z + m_\pi)^2$. It implies that Z_c can be produced on-shell, which means that we have to account for the finite width of Z_c in the rescattering (dispersive) part. The correct implementation requires modeling the propagator using a spectral representation, i.e., it should have sound analyticity properties, such as exhibiting a pole on the unphysical Riemann sheet and the right-hand cuts starting at $\pi J/\psi$ and $D\bar{D}^*$ thresholds. This analysis is beyond the scope of this work due to the lack of experimental information. We checked, however, on the example of the toy model that a naive implementation of the finite width hardly affects the results of the dispersive integral due the narrowness of Z_c. Therefore, for the rescattering part, we neglect the width of Z_c, while in the evaluation of the first two terms of Eq.(5.11), we include the finite width of Z_c to Eq.(5.26).

5.3 Results and Discussion

In the previous section, we described our theoretical approach, which consists in using a charged exotic state as an intermediate particle and the dispersion theory to account for the two-pion final state interaction, as shown in Eq.(5.11). With that, we perform a simultaneous fit of the experimental invariant mass distributions $M^2_{\psi\pi^\pm}$ and $M^2_{\pi^+\pi^-}$ at different e^+e^--CM energies $q = 4.226;\ 4.258;\ 4.358;\ 4.416$ GeV. From the total cross section normalization, as given in Ref. [108], we extract the normalized mass distributions by assuming a constant detector efficiency.

q (GeV)	4.226	4.258	4.416	q (GeV)	4.358
$\lvert e\,\mathcal{F}_{\gamma^*\pi Z_c}\,C_{Z_c\psi\pi}\rvert^2$ (GeV^{-4})	$3.7(5)\cdot 10^{-6}$	$1.3(3)\cdot 10^{-6}$	$2.0(4)\cdot 10^{-6}$	$\lvert e\,\mathcal{F}_{\gamma^*\pi Z_c}\,C_{Z_c\psi\pi}\rvert^2$ (GeV^{-4})	-
$\lvert a/\mathcal{F}_{\gamma^*\pi Z_c}\,C_{Z_c\psi\pi}\rvert$ (GeV^2)	$1.09(25)\cdot 10^{3}$	$0.15\cdot b$	$2.02(24)\cdot 10^{3}$	a/b (GeV^2)	$-0.165(4)$
ϕ_a (rad)	5.60(20)	2.61(25)	2.28(18)	ϕ_a (rad)	-
$\lvert b/\mathcal{F}_{\gamma^*\pi Z_c}\,C_{Z_c\psi\pi}\rvert$	$7.4(16)\cdot 10^{3}$	$8.2(14)\cdot 10^{3}$	$9.5(10)\cdot 10^{3}$	$\lvert b\rvert^2$ (GeV^{-4})	$3.59(19)\cdot 10^{2}$
ϕ_b (rad)	1.98(14)	5.40(19)	5.57(15)	ϕ_b (rad)	-
χ^2_{red}	1.16	1.01	1.38	χ^2_{red}	0.83

TABLE 5.1: Fit parameters entering Eq.(5.11) for four different e^+e^--CM energies q.

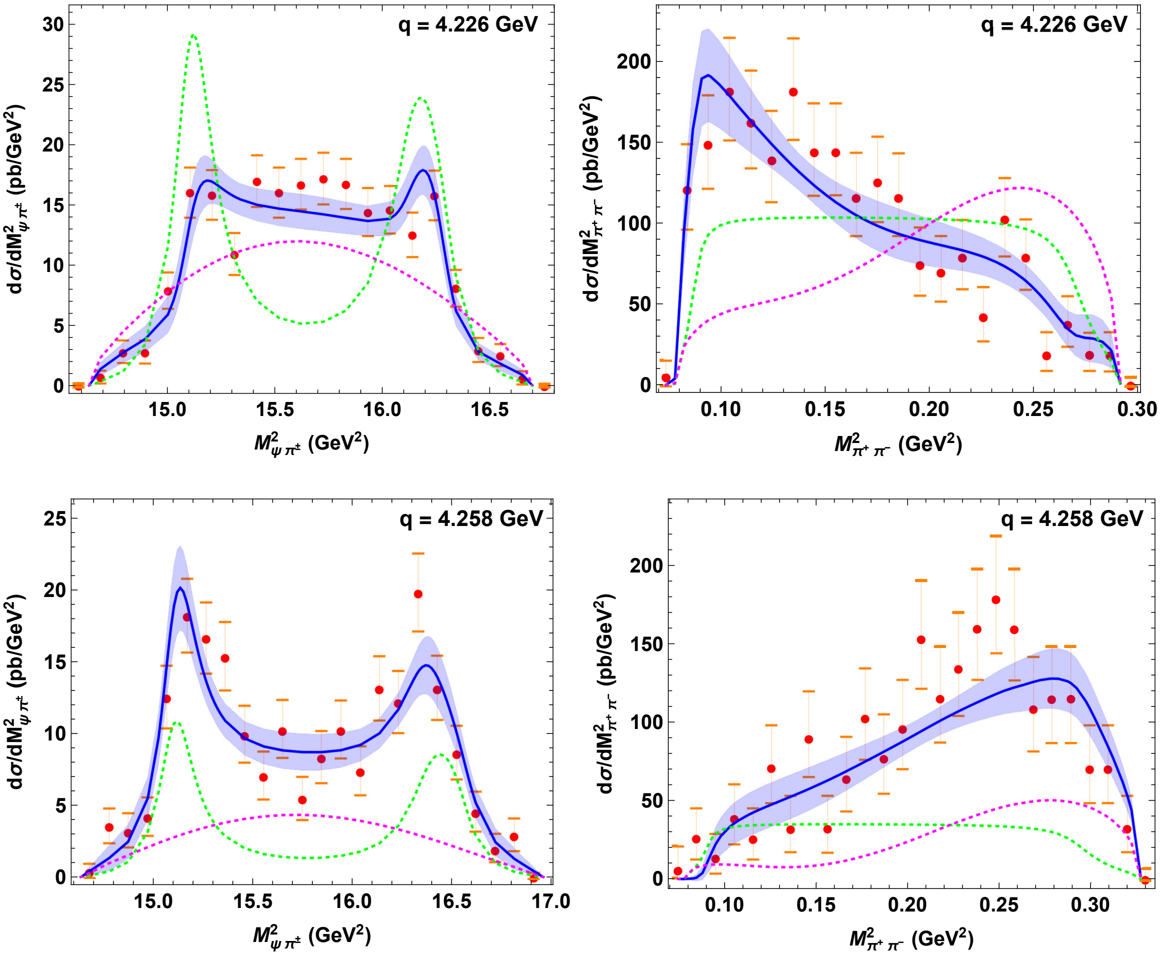

FIGURE 5.2: Fits for $q = 4.226$ GeV and 4.258 GeV including the intermediate state $Z_c(3900)$. The red dots are the data points from BESIII [108] normalized as explained in the text. The blue curves are the fit performed with two subtractions, where the purple bands are calculated by propagating the statistical error of the parameters with 95% confidence level. The green dotted curves are the contribution of only the intermediate state $Z_c(3900)$ and the magenta dotted curves are the contribution from the $\pi\pi$-FSI (i.e. when $C_{Z_c\psi\pi} = 0$).

q (GeV)	$\lvert a/b\rvert$ (GeV^2)	ϕ_a/π	ϕ_b/π	$\chi^2_{\rm red}$
4.226	0.15(5)	1.78(6)	0.63(4)	1.16
4.258	0.15	0.83(8)	1.71(6)	1.01
4.358	0.165(4)	-	-	0.83
4.416	0.21(3)	0.72(6)	1.77(5)	1.38

TABLE 5.2: Comparison of the complex subtraction constants of Eq.(5.11) $a = |a|e^{i\phi_a}$ and $|b|e^{i\phi_b}$ for four different e^+e^--CM energies q.

For each energy q we consider initially two complex subtraction constants, $|a|, \phi_a$ and $|b|, \phi_b$ respectively, and a global normalization, which contains the product of the coupling constants $\mathcal{F}_{\gamma^*\pi Z} C_{Z\psi\pi}$. The subtraction constants are complex due to the specific analytic structure of the Z_c exchange left-hand cut which overlaps with the unitarity cut (see Eq.(5.28)). All the fit parameters are supposed to depend on q. However, for nearby values of q we do not expect a large variation in the parameter values. Despite using the same expression to fit the data, the parameter values are completely driven by the experimental distribution, which exhibits different features for each e^+e^--CM energies q. The results of the fits are shown in Tables 5.1 and 5.2.

At $q = 4.226$ GeV we achieve a very good description of the experimental data for both invariant mass distributions, considering the already established $Z_c(3900)$ as the intermediate state, with $m_{Z_c} = 3.8866$ GeV and $\Gamma_{Z_c} = 28.1$ MeV from Ref. [37]. As one can see in Fig. 5.2, this result is an improvement over the phenomenological description in Ref. [108], where the $M^2_{\psi\pi}$ and $M^2_{\pi\pi}$ mass distributions could not be fitted simultaneously. For $q = 4.258$ GeV we consider the same assumptions as for the $q = 4.226$ GeV case and also obtain a good description of the data. However, the fit is not sensitive to the value of the first subtraction constant a. Therefore, we fix $a(q = 4.258)$ by constraining the ratio of the subtraction constants to be the same as in the lower $q = 4.226$ GeV, i.e. $a/b_{q=4.258} = a/b_{q=4.226}$ and obtain an excellent reduced chi-squared of $\chi^2_{\rm red} \equiv \chi^2/N_{\rm d.o.f} = 1.01$. At $q = 4.358$ GeV we observe that the best fit does not require an intermediate Z_c state in the left-hand cuts. The fit with real values for two subtraction constants multiplied by the $\pi\pi$ Omnès function perfectly describe the data, as shown in Fig. 5.3. In other words, this implies that for $q = 4.358$ GeV the left-hand cuts are dominated by the contact interaction which are absorbed in the subtraction

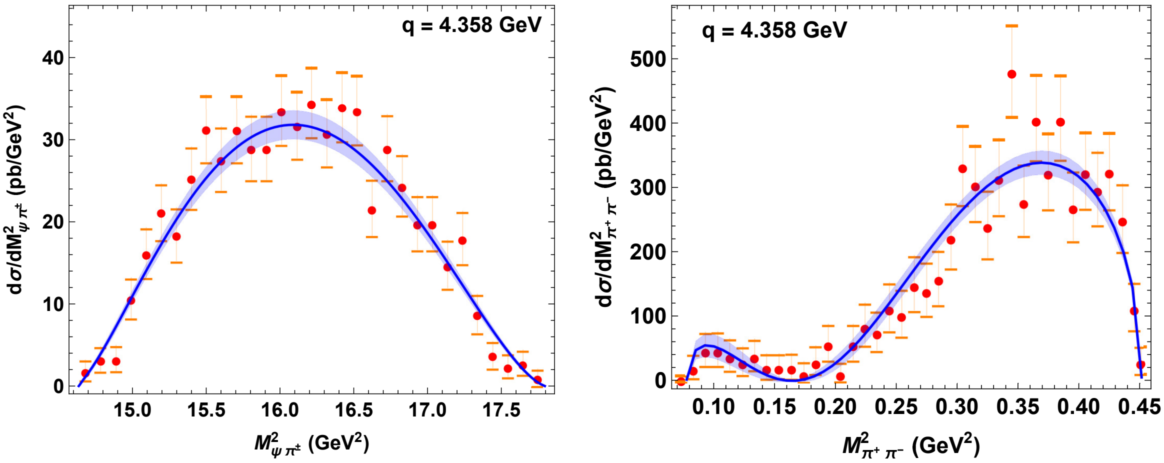

Figure 5.3: Fit for $q = 4.358$ GeV without Z_c intermediate state, i.e. considering the contribution from the $\pi\pi$-FSI.

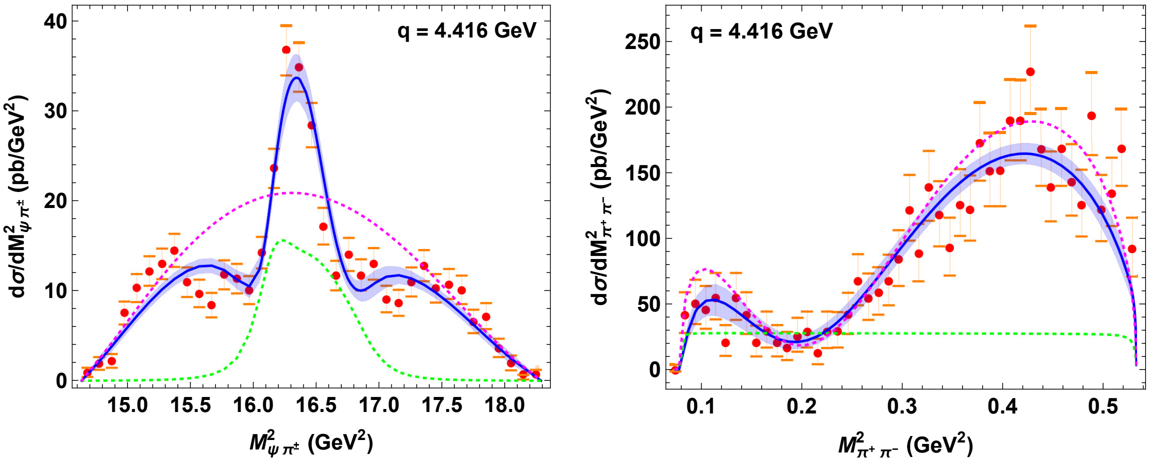

Figure 5.4: Fit for $q = 4.416$ GeV including the heavier Z_c intermediate state.

constants in the present framework.

For $q = 4.416$ GeV, we test the experimental claim of a possible observation of a heavier charged intermediate state [108]. Its parameters were not well established due to unresolved discrepancies between a model fit and the data. In Fig. 5.5, we analyze the dependence of the χ^2_{red} on the mass and the width of the possible heavier Z_c state. For the best χ^2_{red} we obtain an accurate description of the pronounced enhancement in the data (see Fig. 5.4) for the mass $m_{Z_c} = 4.016(4)$ GeV and the width $\Gamma_{Z_c} = 52(10)$ MeV. However, we notice that the χ^2_{red} distribution is wide and smooth. Therefore, we cannot completely rule out that the signal seen at this energy corresponds to $Z_c(4020)$

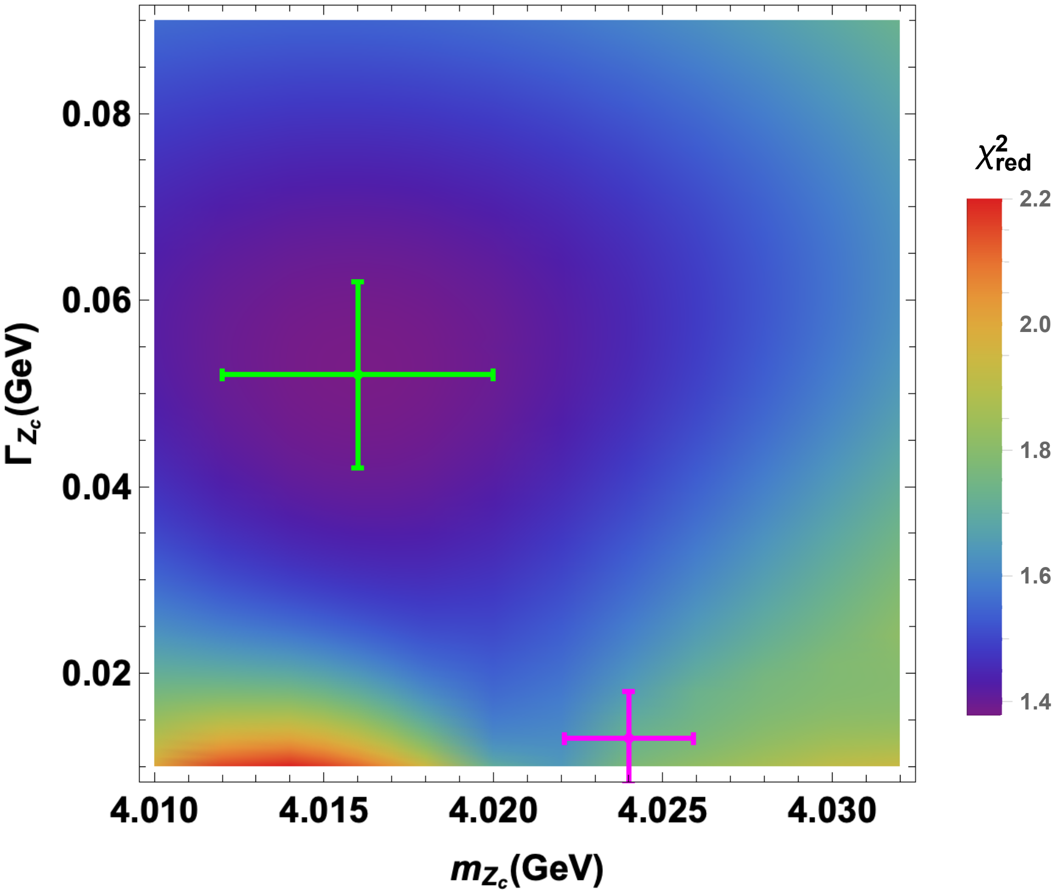

FIGURE 5.5: $\chi^2_{\rm red}$ as a function of the mass and width of the heavier intermediate Z_c state at $q = 4.416$ MeV. The minimum of $\chi^2_{\rm red}$ is indicated by a green cross, with its estimated uncertainty. The PDG average of $Z_c(4020)$ state [37] is indicated by a magenta cross.

($m = 4.024(2)$ GeV and $\Gamma = 13(5)$ MeV according to PDG [37]) observed in the reactions $e^+e^- \to D^*\bar{D}^*\pi$ [126, 127] and $e^+e^- \to h_c\pi\pi$ [128, 129].

The invariant mass distributions of the neutral counterpart $e^+e^- \to \psi(2S)\pi^0\pi^0$ at the same e^+e^--CM energies, were measured experimentally in Ref. [113]. As we pointed out above, due to isospin symmetry the cross section for $e^+e^- \to \psi(2S)\ \pi^0\pi^0$ differs from the one with the charged pions only by the overall symmetry factor of 1/2. However, we do not include this data in our fits since it has lower statistics and does not bring additional constraints on the fit. Future larger statistical samples are desired for both charged and neutral decay channels, to investigate how the already established $Z_c(3900)$ state contributes to $q = 4.416$ GeV.

5.4 Summary

In this chapter, we presented an amplitude analysis of the reaction $e^+e^- \to \psi(2S)\,\pi^+\pi^-$ at different e^+e^--CM energies q. The final state interaction of the two pions is treated using the dispersion theory and we studied quantitatively the contribution of the charged exotic mesons as intermediate states. We observed that the $Z_c(3900)$ state plays an important role to explain the invariant mass distribution at both $q = 4.226$ and $q = 4.258$ GeV. To explain the sharp narrow structure at $q = 4.416$ GeV, a heavier charged state is needed instead, with $m_{Z_c} = 4.016(4)$ GeV and $\Gamma_{Z_c} = 52(10)$ MeV. The latter is not necessarily a new state since its mass is compatible with the already known $Z_c(4020)$. For $q = 4.358$ GeV no intermediate Z_c state is necessary for left-hand cuts in order to describe both $\psi\pi$ and $\pi\pi$ line shapes. It points to another left-hand contribution which we absorbed in the subtraction constants. We also conclude that the $\pi\pi$-FSI is the main mechanism to describe the $\pi\pi$ invariant mass distribution for all four e^+e^--CM energies.

Chapter 6

$e^+e^- \to J/\psi\,\pi^+\pi^-$

This work is a continuation of the formalism presented in Chapter 5, where for the first time a dispersive amplitude analysis was applied to describe $e^+e^- \to \psi(2S)\pi^+\pi^-$ Dalitz plot projections [108, 113]. In our current analysis, the recent BESIII [51] data on $e^+e^- \to J/\psi\pi^+\pi^-$ play the central role. We present a simultaneous description of the $\pi^+\pi^-$ and $\pi^\pm J/\psi$ invariant mass distributions by providing a rigorous dispersive treatment of the $\pi\pi$ final state interactions. We account for $Z_c(3900)$ as an explicit degree of freedom in the t- and u-channels and unitarize the $\pi\pi$ final state interaction on the base of the Muskhelishvili-Omnès formalism. Other possible left-hand cut contributions are absorbed in the subtraction constants which we determine from a combined fit to the $e^+e^- \to J/\psi\pi^+\pi^-$ Dalitz plot data and the total cross section data for $e^+e^- \to J/\psi K^+K^-$. Due to the relatively large physical region of the $\pi\pi$ invariant mass, we also extend our previous analysis in Chapter 5 to the coupled-channel in the $\pi\pi$ S-wave and include the D-wave. Allowing for a minimum number of parameters, which enter in the form of subtraction constants, and assuming the absence of Z_{cs} at $q = 4.23$ GeV and $q = 4.26$ GeV, we provide a prediction for the invariant mass distribution for the process $e^+e^- \to J/\psi\ K^+K^-$. Note that due to the strange quark mass, it is reasonable to assume that the strange partner of $Z_c(3900)$ would have a heavier mass (in particularly, Ref. [130] predicts a mass of 3.97 ± 0.08 GeV) and therefore Z_{cs} cannot be seen as peak in the $K\bar{K}$ invariant mass distribution for $q = 4.23 - 4.26$ GeV.

In our analysis we do not aim at a description of the full $e^+e^- \to J/\psi\pi^+\pi^-$ cross section as a function of q^2 and instead implement the q^2-dependence model independently by applying our formalism for each q-value separately. In Ref.[131], two possible resonant structures were seen in $e^+e^- \to J/\psi\pi^+\pi^-$ total cross section, which were interpreted as effects generated due to the Y(4230) and Y(4360) vector exotic states. The study of these resonance structures is beyond the scope of this analysis. Rather, we want to use the available Dalitz plot projection data to make a simultaneous description of both $\pi^+\pi^-$ and $\pi^\pm J/\psi$ invariant mass distributions and obtain a prediction of the K^+K^- and $K^\pm J/\psi$ invariant mass distributions. This is different from the analysis performed in Ref.[112], which focused only on the $\pi^+\pi^-$ invariant mass distribution to get insights into the structure of the $Y(4260)$ state from the light-quark perspective. Though the analysis of the $\pi\pi$ final state interaction is similar in spirit to ours, there are several technical differences, which we will point out along this chapter.

We start with the theoretical framework, which we extend to a coupled-channel FSI, since the energy region is large and rescattering of pions and kaons has to be handled simultaneously. In Sec.6.2, we present the results of our fits, which describe the $J/\psi\pi$ and $\pi\pi$ invariant mass distributions at two different e^+e^- CM energies, $q = 4.230$ GeV and $q = 4.260$ GeV. Moreover, with the coupled-channel formalism we can also predict the $J/\psi K$ and $K\bar{K}$ line shape for the same energies. We summarize our findings in Sec.6.3. This work led to a publication in Physical Review D [2].

6.1 Dispersive Formalism

In this section, we extend the dispersive formalism to a coupled-channel FSI in order to account for the rescattering between both pions and kaons, which generates the most important singularities at low energies in the s-channel. The partial wave (p.w.) expansion reads

$$\begin{aligned} \mathcal{H}_{I,\lambda_1\lambda_2}(s,t) &= \sum_{J=0}^{\infty}(2J+1)\, d^{(J)}_{\Lambda,0}(\theta_s)\, h^{(J)}_{I,\lambda_1\lambda_2}(s)\,, \\ \mathcal{K}_{I,\lambda_1\lambda_2}(s,t) &= \frac{1}{\sqrt{2}}\sum_{J=0}^{\infty}(2J+1)\, d^{(J)}_{\Lambda,0}(\theta_s)\, k^{(J)}_{I,\lambda_1\lambda_2}(s)\,, \end{aligned} \tag{6.1}$$

where I is the isospin, $\Lambda = \lambda_1 - \lambda_2$ and $d^{(J)}_{\Lambda,0}$ is the Wigner rotation function. In Eq.(6.1), $k^{(J)}_{I,\lambda_1\lambda_2}(s)$ is the p.w. amplitude of the total helicity amplitude $\mathcal{K}_{++}(s,t)$ for $\gamma^*(q) \to J/\psi\, K\bar{K}$. We note, that in the p.w. expansion of the $\gamma^*(q) \to J/\psi\, K\bar{K}$ process we include an extra factor $1/\sqrt{2}$ in contrast to $\gamma^*(q) \to J/\psi\,\pi\pi$ in order to match our normalization for the hadronic p.w. amplitudes, which ensures the same unitarity relations for the identical and non-identical particles. For better readability, below we will consistently suppress the isospin indices, and retrieve them at the beginning of Section 5.3. On account of causality, the p.w. amplitudes should have contributions from the left- and right-hand cuts,

$$\begin{aligned} h^{(J)}_{\lambda_1\lambda_2}(s) &= h^{(J),L}_{\lambda_1\lambda_2}(s) + h^{(J),R}_{\lambda_1\lambda_2}(s)\,, \\ k^{(J)}_{\lambda_1\lambda_2}(s) &= k^{(J),L}_{\lambda_1\lambda_2}(s) + k^{(J),R}_{\lambda_1\lambda_2}(s)\,, \end{aligned} \tag{6.2}$$

where the branch cut due to the two-pion interaction starts at $s = 4\,m_\pi^2$, while for the two-kaon starts at $s = 4\,m_k^2$. The cuts associated with the crossed channel exchange terms, i.e. $h^{(J),L}_{\lambda_1\lambda_2}(s)$, are approximated by the charged Z_c exchanges, motivated by the experimental data [51], where the $Z_c(3900)$ axial-vector state and its kinematic reflection show up as clear peaks in the $\pi J/\psi$ projection for both e^+e^--CM energies $q = 4.23$ GeV and $q = 4.26$ GeV. According to the mechanism $\gamma^*(q^2) \to \pi^\mp + (Z_c^\pm \to J/\psi + \pi^\pm)$, the helicity amplitude has analytical structure as Eq.(5.21) for $\gamma^*(q^2) \to \pi^\mp + (Z_c^\pm \to \psi(2S) + \pi^\pm)$ discussed in the previous chapter, because all the particles have the same J^{PC} quantum numbers. Analogously, $k^{(J),L}_{\lambda_1\lambda_2}(s)$ would be generated by the exchange of the strange partner of $Z_c(3900)$, the Z_{cs}, with the following mechanism $\gamma^*(q^2) \to K^\mp + (Z_{cs}^\pm \to J/\psi + K^\pm)$. However, since the mass of Z_{cs} is expected to be heavier than $Z_c(3900)$ (for instance see Ref.[130]), there is not enough energy to produce Z_{cs} at $q = 4.23 - 4.26$ GeV. Therefore, we set $k^{(J),L}_{\lambda_1\lambda_2}(s) = 0$.

As shown in Chapter 5, the S-wave the p.w. helicity amplitudes are correlated at the kinematic points $s = (q \pm m_\psi)^2$ (see Eq.(5.20)), while for the D-wave the kinematic correlations between different p.w. helicity amplitudes are more complicated and can be found in Ref.[105]. Even though the kinematic set up is different from the process $\gamma^*(q^2) \to \pi^\mp + (Z_c^\pm \to \psi(2S) + \pi^\pm)$ (Chapter 5), we observe that these constraints have a negligible impact on the results, since the sum in Eq.(5.1) in the physical region can be written in terms of $\mathcal{H}_{++}$ only, i.e.

$$\sum_{\lambda_1\lambda_2} |\mathcal{H}_{\lambda_1\lambda_2}|^2 \approx 3\,|\mathcal{H}_{++}|^2\,. \tag{6.3}$$

Under this approximation it is enough to take into account only the so-called centrifugal barrier factor for $J = 2$

$$h^{(2)}_{++}(s) \sim \mathcal{O}\left(\gamma(s)\right)\,, \tag{6.4}$$

$$\gamma(s) \equiv (s - 4m_\pi^2)(s - (q - m_\psi)^2)\,,$$

which comes from the properties of the Legendre polynomials entering p.w. expansion in Eq.(6.1). We note, however, while Eq.(6.4) is exact for $s = 4m_\pi^2$, a zero at $s = (q - m_\psi)^2$ is only approximate and typically a few MeV away. This is related to the approximation made in Eq.(6.3), which we will discuss further on.

The discontinuity across the branch cut in the s-channel in the S-wave is given by

$$\begin{bmatrix} \text{Disc}\, h_{++}^{(0)}(s) \\ \text{Disc}\, k_{++}^{(0)}(s) \end{bmatrix} = t^{(0)*}(s)\,\rho(s) \begin{bmatrix} h_{++}^{(0)}(s) \\ k_{++}^{(0)}(s) \end{bmatrix} . \tag{6.5}$$

The two-body phase space $\rho(s)$ is given by

$$\rho(s) = \frac{1}{16\,\pi} \begin{bmatrix} \sigma_{\pi\pi}\,\theta(s - 4m_\pi^2) & 0 \\ 0 & \sigma_{KK}\,\theta(s - 4m_K^2) \end{bmatrix} , \tag{6.6}$$

where $\sigma_{\alpha\alpha}(s) = \lambda^{1/2}(s, m_\alpha^2, m_\alpha^2)/s$, with $\alpha = \pi$ or K. The $\{\pi\pi, K\bar{K}\}$ coupled-channel scattering amplitude $t(s)$ is normalized as $\text{Disc}\,(t^{(0)}(s))^{-1} = -\rho(s)$. For the S-wave the standard Muskhelishvili-Omnès representation for the left-hand cut subtracted p.w. amplitude is given by (modulo subtractions)

$$\begin{bmatrix} h_{++}^{(0),R} \\ k_{++}^{(0),R} \end{bmatrix} = -\Omega^{(0)} \int_{4m_\pi^2}^{\infty} \frac{ds'}{\pi} \frac{\text{Disc}\,(\Omega^{(0)}(s'))^{-1}}{s' - s} \begin{bmatrix} h_{++}^{(0),L}(s') \\ k_{++}^{(0),L}(s') \end{bmatrix} , \tag{6.7}$$

where the coupled-channel Omnès function (with $1 = \pi\pi$ and $2 = K\bar{K}$)

$$\Omega^{(0)}(s) = \begin{bmatrix} \Omega_{11}^{(0)}(s) & \Omega_{12}^{(0)}(s) \\ \Omega_{21}^{(0)}(s) & \Omega_{22}^{(0)}(s) \end{bmatrix} , \tag{6.8}$$

satisfies the following unitarity relation

$$\text{Disc}\,\Omega^{(J)}(s) = t^{(J)*}(s)\,\rho(s)\,\Omega^{(J)}(s) . \tag{6.9}$$

Since the tail of the $f_2(1270)$ resonance could overlap with the physical region, we include D-wave single-channel $\pi\pi$-rescattering. As discussed previously, we factor out the known threshold factor and write a dispersion relation for $h_{++}^{(2),R}(s)\,(\Omega^{(2)}(s))^{-1}/\gamma(s)$

which leads to

$$h_{++}^{(2),R}(s) = \gamma(s)\,\Omega^{(2)}(s) \times \left\{ -\int_{4m_\pi^2}^{\infty} \frac{ds'}{\pi} \frac{\text{Disc}\,(\Omega^{(2)}(s'))^{-1}}{(s'-s)} \frac{h_{++}^{(2),L}(s')}{\gamma(s')} \right\}, \tag{6.10}$$

where under the dispersive integral we slightly adjusted a zero of $\gamma(s')$ at $s' = (q-m_\psi)^2$ to match exactly a zero of $h_{++}^{(2),L}(s')$, which is few MeV away. One can notice, that the overall threshold factor $\gamma(s)$ is also needed to compensate the singularities of $z = \cos\theta_s$ (see Eq.(5.4) in Chapter 4) of the full amplitude $\mathcal{H}_{++}^{R}(s,t)$ at the boundaries of the Dalitz plot (i.e. at $s = 4m_\pi^2$ and $s = (q-m_\psi)^2$). This is different from Ref.[112] where in the dispersive representation no threshold factors were taken into account in the D-wave.

In our formalism, we are accounting for the $\pi\pi$ rescattering effects only in S- and D-waves, and beyond that (for $J > 2$) the p.w. amplitudes in Eq.(6.2) are approximated by the first term, $h_{\lambda_1\lambda_2}^{(J),L}(s)$. In other words, we keep the cross channel p.w. expansion to all orders. That is crucial to get the description of the full Dalitz plot, where there are peaks structures in both $\pi\pi$ and $\pi J/\psi$ systems. The final result for the total helicity amplitude can be written as

$$\begin{aligned} \mathcal{H}_{++}(s,t) &= \mathcal{H}_{++}^{L}(s,t) + \sum_{J=0}^{2}(2J+1)\,P_J(z)\,h_{++}^{(J),R}(s), \\ \mathcal{K}_{++}(s,t) &= k_{++}^{(0),R}(s), \end{aligned} \tag{6.11}$$

where the sum goes only over even J values due to Bose symmetry of two pions and C-parity conservation and we consider only the rescattering of kaons in the S-wave.

6.1.1 Triangle Singularities

In the representation given in Eq.(6.7), the left-hand cut overlaps with the right-hand cut and requires special treatment in the dispersive formalism. In the previous chapter about $\gamma^*(q^2) \to \psi(2S)\pi\pi$ [1] such an overlap required a distortion of the integration path which was performed by including an additional anomalous piece [121–123]. For the processes considered in the present chapter, the overlap of the left and right-hand cuts does not introduce anomalous thresholds, but still require the proper analytical

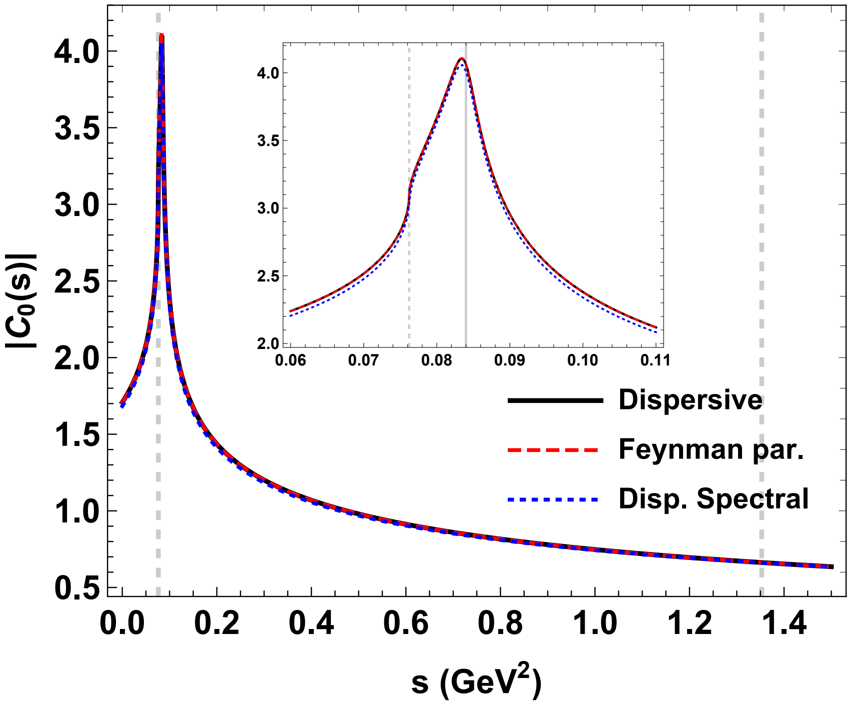

FIGURE 6.1: Comparison of the absolute values of the scalar triangle loop function $C_0(q^2, m_\psi^2, m_\pi^2, m_Z^2, m_\pi^2)$ calculated numerically using Feynman parameters (dashed red line) with a dispersive evaluation (solid black line) at $q = 4.23$ GeV. The vertical dashed lines indicate the kinematically allowed decay region, while the solid gray line in the inset is exactly at the position of the triangle singularity.

continuation for the energy variable $q^2 \to q^2 + i\epsilon$ [76, 125] due to the presence of the so-called triangle singularity [79, 132, 133] associated with $Z_c\pi\pi$ loop. Indeed, for $q = 4.23$ GeV and $q = 4.26$ GeV the exchange of the $Z_c(3900)$ state in the triangle loop can be on-shell, satisfying the Coleman-Norton conditions $q^2 > (m_Z + m_\pi)^2$ and $m_Z^2 > (m_\psi + m_\pi)^2$ [80]. This implies that the branch point s_- associated with the left-hand cut

$$\begin{aligned} s_- =& \frac{1}{2}\left[q^2 + m_\psi^2 + 2m_\pi^2 - m_Z^2 - \frac{(q^2 - m_\pi^2)(m_\psi^2 - m_\pi^2)}{m_Z^2}\right] \\ & - \frac{\kappa(m_Z^2)}{2\,m_Z^2}\,, \end{aligned} \tag{6.12}$$

is located just above the two pion threshold but infinitesimally below the real axis [46]. We note, that the $q^2 \to q^2 + i\,\epsilon$ continuation guarantees that the branching point never crosses the unitarity cut and the dispersive representations of Eqs. (6.7) and (6.10) are

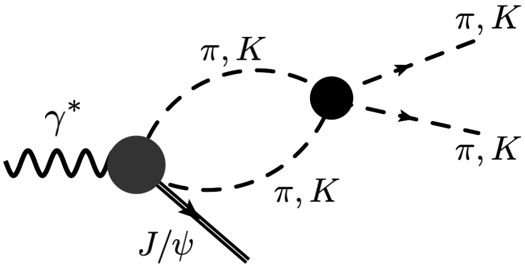

FIGURE 6.2: Diagrammatic representation of the final state interaction of the process $\gamma^* \to J/\psi\, \pi\pi\, (K\bar{K})$.

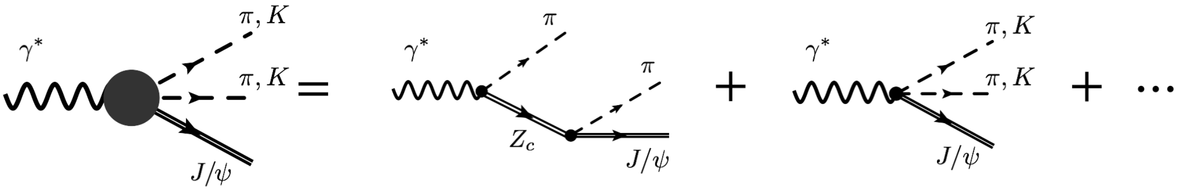

FIGURE 6.3: The physical meaning of the left vertex of Fig.6.2.

correct. Due to the finite resonance width, however, the effect of the triangle singularity smears out, since the singular point is shifted further away from the physical region.

There are different ways of accounting for the width of the $Z_c(3900)$ state. Since the width of the $Z_c(3900)$ meson is relatively small ($\Gamma_Z = 28.2$ MeV) [37], we follow here a pragmatic approach by implementing the finite width in the denominators of Eq.(5.26). In this case, it is possible to cross-check our dispersive implementation on an example of a toy model of scalar fields with a constant (equal to unity) interaction between pions. As one can see in Fig.6.1, the result of the dispersive calculation and the calculation via Feynman parameters in perturbation theory gives numerically the same results. For illustrative purpose, we also show in Fig.6.1 the result based on using the spectral representation of the Z_c propagator [76], but accounting for just one channel $\pi J/\psi$ as it was done in Ref.[112]. As expected the difference is negligible. Due to the narrowness of the $Z_c(3900)$ state one can also observe in Fig.6.1 that the peak is still relatively sharp. However, the inclusion of the unitarization through the Muskhelishvili-Omnès representation smears it out in the Dalitz plot.

6.2 Results and Discussion

For the S-wave contribution we write a twice-subtracted dispersive representation. Due to the coupled-channel there are in total four subtraction constants. For the D-wave we allow for one subtraction. Even though the dispersive integrals are formally convergent with less subtractions they acquire significant corrections from the integration over large s. Therefore, we implement over-subtracted dispersion relations in order to reduce the sensitivity to the high energy region and the effects of additional unknown left-hand cuts, such as possible D-meson loops or contact interaction [110, 112]. To check on the physical importance of the latter, we will also compare in the following for the S-wave contribution the fitted subtraction constants with the sum rule result which one would obtain from a once-subtracted dispersive formalism.

For the S- and D-waves we diagrammatically show the contributions in our formalism in Fig.6.2 (with the input from Fig.6.3). For all higher partial waves, we take the contribution of the pure Z_c diagram only (first term on the *rhs* of Fig.6.3). Since the dispersion relations in Eqs. (6.7) and (6.10) are written for $I = 0$ we need to encode the transformation coefficients between isospin and the physical amplitudes (see Eqs. 3.9 and 3.10),

$$\mathcal{H}_{++} = \frac{1}{\sqrt{3}}\,\mathcal{H}_{0,++}\,, \qquad \mathcal{K}_{++} = \frac{1}{\sqrt{2}}\,\mathcal{K}_{0,++}\,. \tag{6.13}$$

Therefore, for $e^+e^- \to J/\psi\,\pi^+\pi^-$ one obtains

$$\begin{aligned}
\mathcal{H}_{++}(s,t) = \frac{1}{\sqrt{3}}\Bigg[&\mathcal{H}^{Z_c}_{0,++}(s,t) \\
&+ \Omega^{(0)}_{11}\left\{a + b\,s - \frac{s^2}{\pi}\int\limits_{4m_\pi^2}^{\infty}\frac{ds'}{s'^2}\,\frac{\mathrm{Disc}\,(\Omega^{(0)}(s'))^{-1}_{11}}{s'-s}\,h^{(0),Z_c}_{0,++}(s')\right\} \\
&+ \Omega^{(0)}_{12}\left\{c + d\,s - \frac{s^2}{\pi}\int\limits_{4m_\pi^2}^{\infty}\frac{ds'}{s'^2}\,\frac{\mathrm{Disc}\,(\Omega^{(0)}(s'))^{-1}_{21}}{s'-s}\,h^{(0),Z_c}_{0,++}(s')\right\} \\
&+ 5\,P_2(z)\,\gamma(s)\,\Omega^{(2)} \\
&\quad\times\left\{e - \frac{s}{\pi}\int\limits_{4m_\pi^2}^{\infty}\frac{ds'}{s'}\,\frac{\mathrm{Disc}\,(\Omega^{(2)}(s'))^{-1}}{s'-s}\,\frac{h^{(2),Z_c}_{0,++}(s')}{\gamma(s')}\right\}\Bigg],
\end{aligned} \tag{6.14}$$

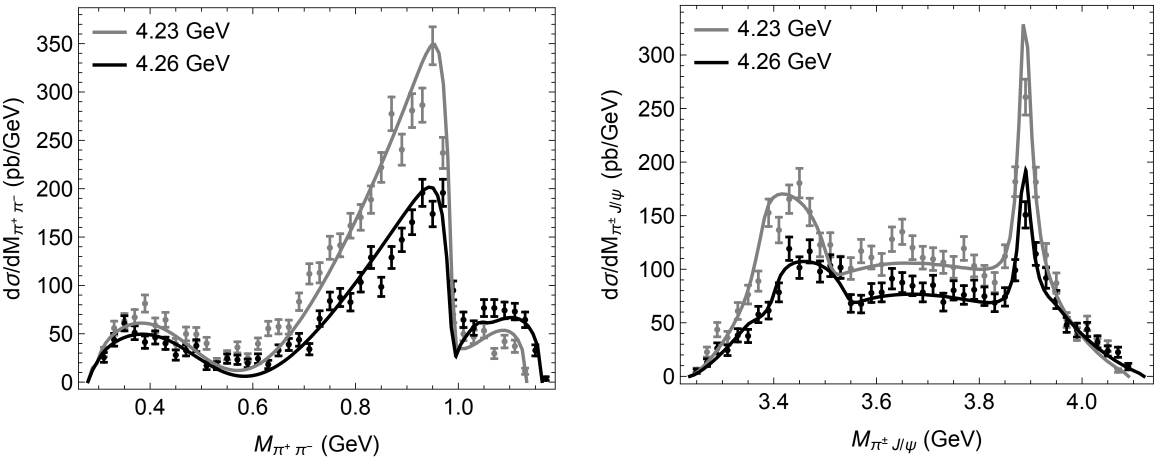

FIGURE 6.4: The most economical fit with four real parameters at $q = 4.23$ GeV and $q = 4.26$ GeV (see Fit 1 in Table 6.1). The BESIII data is taken from Ref.[51], which was normalized to the total cross section given in Ref.[131].

where $\mathcal{H}^{Z_c}_{0,++}(s,t)$ is a pure Z_c-exchange and we put $h^{(J),L}_{0,++}(s) = h^{(J),Z_c}_{0,++}(s)$ and $k^{(J),L}_{0,++}(s) = 0$ according to the discussion given above. We note that the partial wave amplitudes $h^{(J),Z_c}_{0,++}(s)$ were properly modified due to the presence of logarithmic singularity (see Section 2.8). For the $e^+e^- \to J/\psi\, K^+K^-$ there is only a S-wave contribution corresponding to

$$\begin{aligned}
&\mathcal{K}_{++}(s,t) = \qquad\qquad (6.15)\\
&\frac{\Omega^{(0)}_{21}}{2}\left\{a + b\,s - \frac{s^2}{\pi}\int\limits_{4m_\pi^2}^{\infty}\frac{ds'}{s'^2}\frac{\text{Disc}\,(\Omega^{(0)}(s'))^{-1}_{11}}{s'-s}\,h^{(0),Z_c}_{0,++}(s')\right\}\\
&+\frac{\Omega^{(0)}_{22}}{2}\left\{c + d\,s - \frac{s^2}{\pi}\int\limits_{4m_\pi^2}^{\infty}\frac{ds'}{s'^2}\frac{\text{Disc}\,(\Omega^{(0)}(s'))^{-1}_{21}}{s'-s}\,h^{(0),Z_c}_{0,++}(s')\right\}
\end{aligned}$$

We perform a simultaneous fit to the $\pi^+\pi^-$ and $\pi^\pm J/\psi$ invariant mass distributions [51] together with the total cross section data for $\sigma(J/\psi K^+K^-)$ [134]. To ensure that the $e^+e^- \to J/\psi K^+K^-$ total cross section constraint is well accounted for and contributes realistically to the total χ^2, we re-scale its error by the amount of experimental data points above the $K\bar{K}$ threshold in the $\pi\pi$ distributions. In our fits we therefore minimize

$$\chi^2_{tot} = \frac{1}{N_{dof}}\left(\chi^2_{\pi\pi} + \chi^2_{\pi\psi} + \chi^2_{KK}\right)\,, \qquad (6.16)$$

where

$$\begin{aligned}
\chi^2_{\pi\pi} &= \sum_{i=1}^{N_{\pi\pi}} \left(\frac{d\sigma_i^{\rm Th}/dM_{\pi\pi} - d\sigma_i^{\rm Exp}/dM_{\pi\pi}}{\Delta(d\sigma_i^{\rm Exp}/dM_{\pi\pi})} \right)^2 , \\
\chi^2_{\pi\psi} &= \sum_{i=1}^{N_{\pi\psi}} \left(\frac{d\sigma_i^{\rm Th}/dM_{\pi\psi} - d\sigma_i^{\rm Exp}/dM_{\pi\psi}}{\Delta(d\sigma_i^{\rm Exp}/dM_{\pi\psi})} \right)^2 , \\
\chi^2_{KK} &= \left(\frac{\sigma(J/\psi K^+K^-)^{\rm Th} - \sigma(J/\psi K^+K^-)^{\rm Exp}}{\Delta\sigma(J/\psi K^+K^-)^{\rm Exp}/\sqrt{2\,N_{KK}}} \right)^2 ,
\end{aligned} \tag{6.17}$$

with

$$N_{dof} = N_{\pi\pi} + N_{\pi\psi} + 2\,N_{KK} - N_{\rm par}\,. \tag{6.18}$$

The number of data-points are: $\{N_{\pi\pi}, N_{\pi\psi}, N_{KK}\} = \{42,\ 42,\ 7\}$ for $q = 4.23$ GeV and $\{N_{\pi\pi}, N_{\pi\psi}, N_{KK}\} = \{44,\ 43,\ 8\}$ for $q = 4.26$ GeV. Note that in the $\pi\pi$ and $\pi\psi$ data sets we omitted the bins that cross the boundary of the Dalitz plot.

Due to an overlap of left- and right-hand cuts, the subtraction constants (a, b, c, d, e) can in principle be complex, which together with the product $\mathcal{F}_{\gamma^*\pi Z}\, C_{Z\psi\pi}$ leaves us with eleven parameters for each e^+e^- center-of-mass energy to describe the data. We definitely do not want to over-fit the data and describe some variations in the data that could just be statistical noise. Therefore, we decided to start with the most economical fit in which we fit four parameters as described in the following, and will then compare it with our best fit which has seven parameters. The summary of the fit results is given in Table 6.1.

We start with the case when all the subtraction constants are real in the S-wave while for the D-wave we use an unsubtracted dispersive representation. It turns out that the fitted value of the c parameter is consistent with zero and therefore it is justified to ignore it for this initial fit. This leaves us with four real parameters. Even though this parameterization is not perfect, it provides a good description of the data as shown in Fig.6.4. In particular, in the $\pi\pi$ mass distribution the dip structure around the $K\bar{K}$ threshold comes out naturally in our formalism due to the $f_0(980)$ resonance. In addition, the PDG [37] averaged mass and the width of $Z_c(3900)$, $m_Z = 3.8872(23)$ GeV and $\Gamma_Z = 28.2(2.6)$ MeV, seem to be in good agreement with the data for the $\pi\psi$ mass distribution. Furthermore, it is worth to mention an interesting observation:

	$q = 4.23$ GeV		$q = 4.26$ GeV	
	Fit 1	Fit 2	Fit 1	Fit 2
$\|e\,\mathcal{F}_{\gamma^*\pi Z}\,C_{Z\psi\pi}\|^2 \times 10^7$	5.8(4)	3.4(3)	2.9(2)	1.3(2)
$\tilde{a} \times 10^{-3}$	3.3(1)	3.9(2)	4.1(2)	5.3(4)
ϕ_a(rad)	–	-0.50(2)	–	-0.33(2)
$\tilde{b} \times 10^{-3}$	-9.2(4)	-11.2(6)	-11.2(5)	-15.8(1.2)
ϕ_b(rad)	–	-0.20(2)	–	–
$\tilde{c} \times 10^{-3}$	–	–	–	4.6(6)
$\tilde{d} \times 10^{-3}$	-4.0(1)	-5.0(3)	-4.3(2)	-11.6(1.0)
$\tilde{e} \times 10^{-2}$	fixed to sum rule	8.1(1.1)	fixed to sum rule	3.1(2.5)
$\sigma(J/\psi K^+K^-)^{\text{Exp}}$ [pb]	5.3(1.0)		3.1(6)	
$\sigma(J/\psi K^+K^-)^{\text{Th}}$ [pb]	4.4(5)	5.2(2)	2.9(4)	3.0(3)
χ^2_{tot}	3.4	1.7	2.5	1.3

TABLE 6.1: Fit parameters entering Eqs.(6.14) and (6.15) which were adjusted to reproduce the empirical $\pi\pi$ and $\pi J/\psi$ invariant mass distributions together with the cross section $\sigma(J/\psi K^+K^-)$ at e^+e^- center-of-mass energies $q = 4.23$ GeV and $q = 4.26$ GeV. Tildes on top of a subtraction constants indicate that they are given relative to the couplings constants entering $h^{(J),Z_c}_{0,++}$, for instance $\tilde{a} \equiv a/(\mathcal{F}_{\gamma^*\pi Z}\,C_{Z\psi\pi})$. For easier comparison of the fits with real subtraction constants ($\phi_i = 0$) and the fits with complex subtraction constants ($\phi_i \neq 0$), we restricted ϕ_i in the region $(-\pi/2, \pi/2)$, i.e. allowing to have ± signs in front of the absolute value. Errors on fit parameters are shown in brackets.

if we fit only the $\pi\psi$ invariant mass distribution for $q = 4.23$ GeV or $q = 4.26$ GeV, the post-diction for the $\pi\pi$ distribution reproduces very well the major features of the data[1]. This implies that our framework has the correct ingredients in the simultaneous description of the data. As seen from the parameter values of Fit 1 in Table 6.1, we also find that they do not vary much between $q = 4.23$ GeV and $q = 4.26$ GeV. This is in accordance with our expectation since the considered e^+e^- center-of-mass energies are different only by 30 MeV. Therefore, the parameters of Fit 1 determine the starting values of our improved fit.

---

[1] The opposite is not true, because by fitting only the $\pi\pi$ distribution it is hard to constrain well the parameters of the Z_c state and the post-diction of the $\pi\psi$ distribution is then only qualitative.

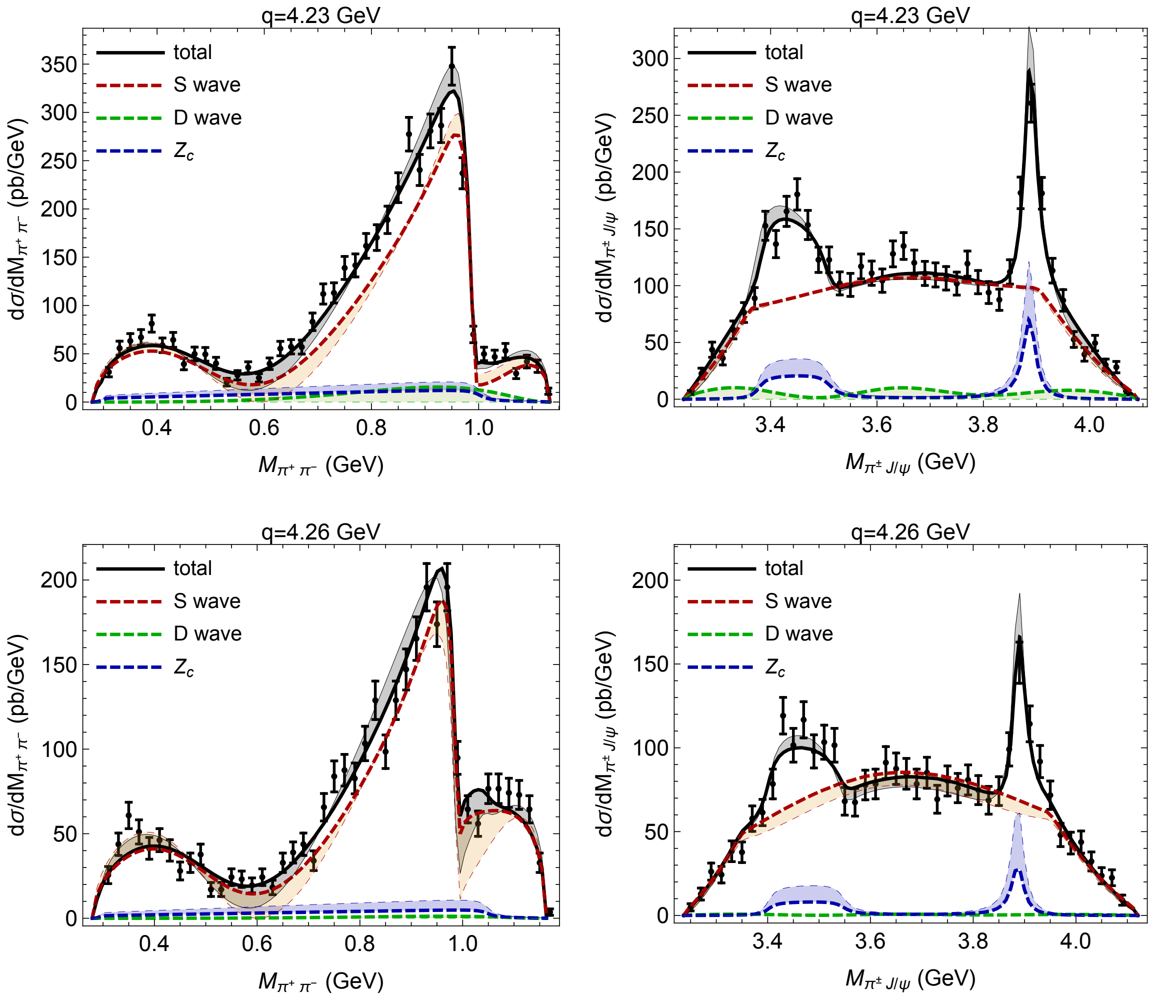

FIGURE 6.5: The black curves are the total fit results. The individual contributions from the pure $Z_c(3900)$-exchange, the $\pi\pi$ re-scattering in the S and D waves are indicated by blue, red and green curves, respectively. On a practical level, these curves correspond to the first, second plus third and forth term of Eq.(6.14), as explained in the text. The shaded bands indicate the spread between Fit 1 (thin curves) and Fit 2 (thick curves) results. The BESIII data is taken from Ref.[51], which was normalized to the total cross section given in Ref.[131].

A significant improvement over Fit 1 can be obtained by adding a phase to the parameter a and to a lesser extent also to the parameter b, since the subtraction constants a and b are mainly responsible for the description of the data below the $K\bar{K}$ threshold. The region above $K\bar{K}$ threshold is a bit more complicated since the parameters c and d play a significant role there. Due to the absence of the $K\bar{K}$ mass distribution data, we keep the subtraction constants c and d real. From the analysis of different fits we found that for $q = 4.23$ GeV a small non-zero value of the phase ϕ_b allows to improve the fit more, while for $q = 4.26$ GeV the parameter c plays a more prominent role. In

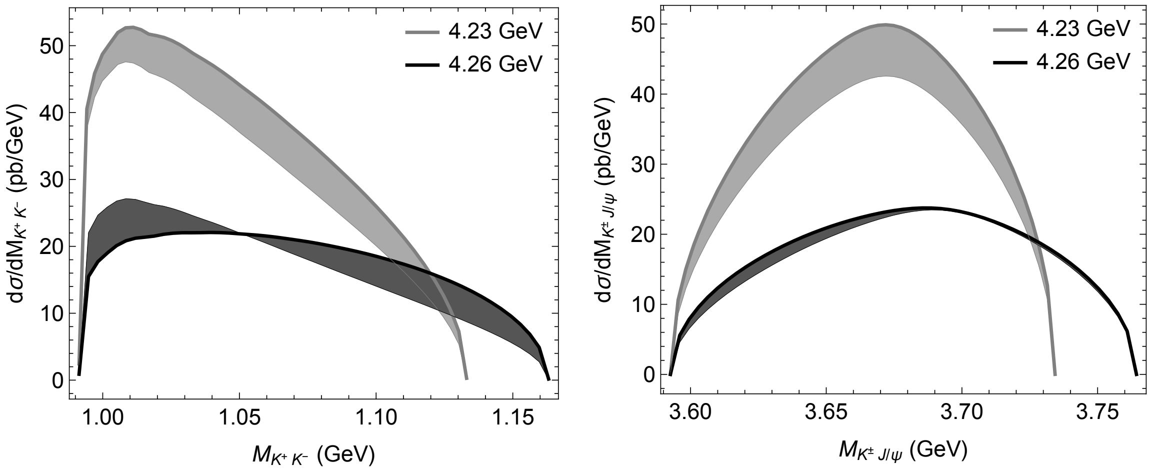

FIGURE 6.6: Theoretical predictions of the K^+K^- and $K^\pm J/\psi$ invariant mass distributions of the $e^+e^- \to J/\psi K^+K^-$ reaction for e^+e^- center-of-mass energies $q = 4.23$ and $q = 4.26$ GeV. The shaded bands indicate the spread between Fit 1 (thin curves) and Fit 2 (thick curves) results.

addition, we allow for one subtraction in the D-wave, which may differ from the unsubtracted sum rule value. As a result, we decided to limit ourselves to the following "best" fit scenario with seven parameters: for $q = 4.23$ GeV we consider the product $\mathcal{F}_{\gamma^*\pi Z}\, C_{Z\psi\pi}, a, \phi_a, b, \phi_b, d$, and e as fit parameters, while for $q = 4.26$ GeV we consider the product $\mathcal{F}_{\gamma^*\pi Z}\, C_{Z\psi\pi}, a, \phi_a, b, c, d$, and e as fit parameters.

The resulting parameters and χ^2 are collected in Table 6.1 in the column Fit 2 and shown in Fig.6.5, where we also show contributions from the individual terms in Eq.(6.14). We see that our results are in very good agreement with the data. As a conservative error estimate we show in Fig.6.5 the spread between Fit 1 (our most economical fit) and Fit 2 (our best fit) results. We found that the remaining parameters, beyond the seven parameters considered, have a rather small effect on the $\pi\pi$ and $\pi\psi$ distributions and can be determined only if very precise data is available.

It is instructive to compare the fitted values of the $\tilde{b}$, $\tilde{d}$ and $\tilde{e}$ parameters from table 6.1 with the sum rule (SR) estimates resulting from a once-less subtracted dispersion relation. Such framework implies e.g. for the parameter b the relation

$$b^{SR} = -\int\limits_{4m_\pi^2}^{\infty} \frac{ds'}{\pi} \frac{\text{Disc}\,(\Omega^{(0)}(s'))^{-1}_{21}}{s'^2}\, h^{(0),Z_c}_{0,++}(s'), \tag{6.19}$$

	$q = 4.23$ GeV	$q = 4.26$ GeV
$(\tilde{b}^{\rm SR}\times 10^{-3}, \phi_b)$	(-0.6,0.9)	(-0.6,1.0)
$(\tilde{d}^{\rm SR}\times 10^{-3}, \phi_d)$	(-0.3,1.0)	(-0.3,1.0)
$(\tilde{e}^{\rm SR}\times 10^{-2}, \phi_e)$	(-0.07,-0.9)	(-0.06,-0.7)

TABLE 6.2: Sum rules for fit parameters $\tilde{b}$, $\tilde{d}$ and $\tilde{e}$, obtained as explained in Eq.(6.19).

and analogous relations for d and e. Using our Z_c pole model for the left-hand cut we obtain the sum rules for the parameters, shown in Table 6.2. For $\tilde{b}$ and $\tilde{d}$ are approximately 20 times smaller in magnitude (and even more for $\tilde{e}$) than the fitted values. This implies that besides the direct production of the Z_c (first term in Eq.(6.14)), which is responsible for the peak regions in the $\pi\psi$ distribution, the two pions are predominantly produced directly in the transition from the Y state to the J/ψ state through a contact term and subsequently rescatter. Our analysis thus shows that the rescattering of the two pions happens predominantly without going through the $Z_c(3900)$ state. In comparison, the dispersive analysis in Ref.[112] indicates that the left-hand cut contributions from Z_c are as significant as the chiral contact interaction and the D-wave contribution is comparable to the S-wave contribution in almost the whole phase space. Apart from a different treatment of the D-wave rescattering in a dispersive formalism (as discussed following Eq.(6.10)), it is hard to compare both approaches since we do not imply any particular dynamics on the contact interaction. The main aim of the present work is to perform a data-driven analysis of both Dalitz projections, in contrast to Ref.[112].

Since we obtained a simultaneous and accurate description of the BESIII data for the $\pi^+\pi^-$ and $\pi^\pm J/\psi$ invariant mass distributions, we find it justified to predict the K^+K^- mass distribution. As one can see in Fig.6.6, the obtained shape has a rapid rise just above the threshold, which is quite different from the pure phase space, i.e. when $\mathcal{K}_{++}(s,t)$ is replaced by a constant. This behavior is due to $f_0(980)$ resonance and we expect to see it in future experimental measurements. For completeness, we also provide the prediction to $K^\pm J/\psi$ mass distribution, which is just a pure phase space in our approximation.

Angular Distributions

Within our formalism, we can also determine angular distributions of $Z_c^{\pm}(3900)$ and J/ψ in the process $e^+e^- \to Z_c^{\pm}\pi^{\mp}$ and $Z_c^{\pm} \to J/\psi\pi^{\mp}$. The angular distributions of J/ψ can be obtained from Eq.(5.1) in the following way

$$\frac{d\sigma}{d\cos\theta_{J/\psi}} = \int_{t_i}^{t_f} dt\, \frac{d^2\sigma}{ds\, dt}\, \frac{ds}{d\cos\theta_{J/\psi}}, \tag{6.20}$$

where $\theta_{J/\psi}$ is the polar angle of J/ψ in the Z_c rest frame (see Fig.D.1), t_i and t_f are the integration limits of t, which will be discussed later. The kinematic invariant s can be expressed in terms of $\cos\theta_{J/\psi}$ as

$$s = q^2 + m_{J/\psi}^2 - 2E_{\gamma^*}E_{J/\psi} + 2|\vec{p}_{\gamma^*}||\vec{p}_{J/\psi}|\cos\theta_{J/\psi}, \tag{6.21}$$

where the energies and momenta in the t-channel are given by

$$\begin{aligned} E_{J/\psi} &= \frac{t + m_{J/\psi}^2 - m_\pi^2}{2\sqrt{t}}, \quad |\vec{p}_{J/\psi}| = \frac{1}{2\sqrt{t}}\,\lambda^{1/2}(t, m_{J/\psi}^2, m_{\pi^+}^2), \\ E_{\gamma^*} &= \frac{t + q^2 - m_\pi^2}{2\sqrt{t}}, \quad |\vec{p}_{\gamma^*}| = \frac{1}{2\sqrt{t}}\,\lambda^{1/2}(t, q^2, m_\pi^2). \end{aligned} \tag{6.22}$$

Analogously, the angular distributions of $Z_c^{\pm}(3900)$ can be obtained from Eq.(4.27)

$$\frac{d\sigma}{d\cos\theta_{Z_c^{\pm}}} = \int_0^{2\pi} d\phi_{31} \int_{s_i(t)}^{s_f(t)} ds \int_{t_i}^{t_f} dt\, \frac{d\sigma}{ds\, dt\, d\cos\theta_{Z_c^{\pm}}\, d\phi_{31}}, \tag{6.23}$$

where θ_{Z_c} is the polar angle of Z_c in the e^+e^--CM frame [2] and $s_i(t)$ and $s_f(t)$ are the integration limits of $M_{\pi^+\pi^-}^2$ in the Dalitz region (see Chapter 2.3). With Eqs. (6.20) and (6.23) we can use our formalism to calculate the angular distributions for the e^+e^--CM energies $q = 4.23$ and 4.26 GeV. The angular distribution for J/ψ shown in Fig.6.7 exhibits a similar behaviour for both energies, where the shaded region shows the spread between fit 1 and fit 2. The orange lines give only the Z_c contributions, which is a constant, as for axial-vector quantum numbers, the $Z_c \to \pi\psi$ decay is in a relative S-wave. The difference between the blue and orange bands in Fig.6.7 thus reveals that the line shape is dominated by the $\pi\pi$-FSI.

---

[2] The angle $\theta_{Z_c^+}$ corresponds to θ_t and $\theta_{Z_c^-}$ corresponds to θ_u, depicted in Fig.2.9. Notice that due to the isospin symmetry the angular distributions for Z_c^+ and Z_c^- are equivalent.

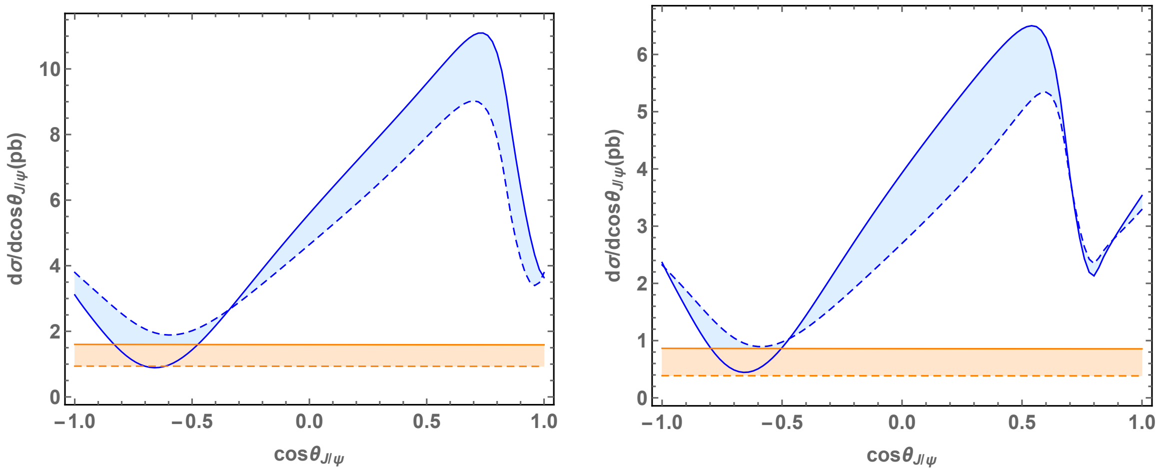

FIGURE 6.7: Angular distribution of J/ψ at e^+e^--CM energies $q = 4.23$ GeV (left panel) and $q = 4.26$ GeV (right panel), for $m_{J/\psi}$ around the mass of $Z_c(3900)$. The solid lines represent fit 1 and the dashed lines fit 2, where the parameters are given in Table 6.1. The blue curves show the results of all contributions while the orange ones show the contributions of the $Z_c(3900)$ only.

In order to compare our results to the experimental data from Ref.[51], shown in the top panels of Fig.6.8, we need to average the e^+e^--CM energies q. In addition to that, the experimental angular distributions are not efficiency corrected, which means that correcting the data points according to the energy efficiency of the detectors could change the line shape of the angular distributions. This fact prohibits us at this point from directly comparing the experimental points to our results. Nonetheless, we can perform a qualitative comparison between the outcome obtained using the formalism developed in this thesis and the experimental data. For the angular distribution of Z_c shown in the bottom left panel of Fig.6.8, we observe a constant behavior, which is compatible with the shape of the experimental data. Even though the curves shown in Fig.6.7 are not symmetric around zero, we consider the angular distribution of J/ψ in terms of the modulus of $\cos\theta_{J/\psi}$ in order to compare with the experimental analysis. Our results shown in the bottom right panel of Fig.6.8, exhibit a similar behavior as the experimental data, with a drop towards the maximum values of $\cos\theta_{J/\psi}$. We use the integration limits around the Z_c mass, with $t_i = (3.86\text{ GeV})^2$ and $t_f = (3.91\text{ GeV})^2$. We notice that our results are very sensitive to these integration limits and recommend for futures comparisons to integrate over the whole range of the Dalitz plot and compare at fixed values of e^+e^--CM energy q.

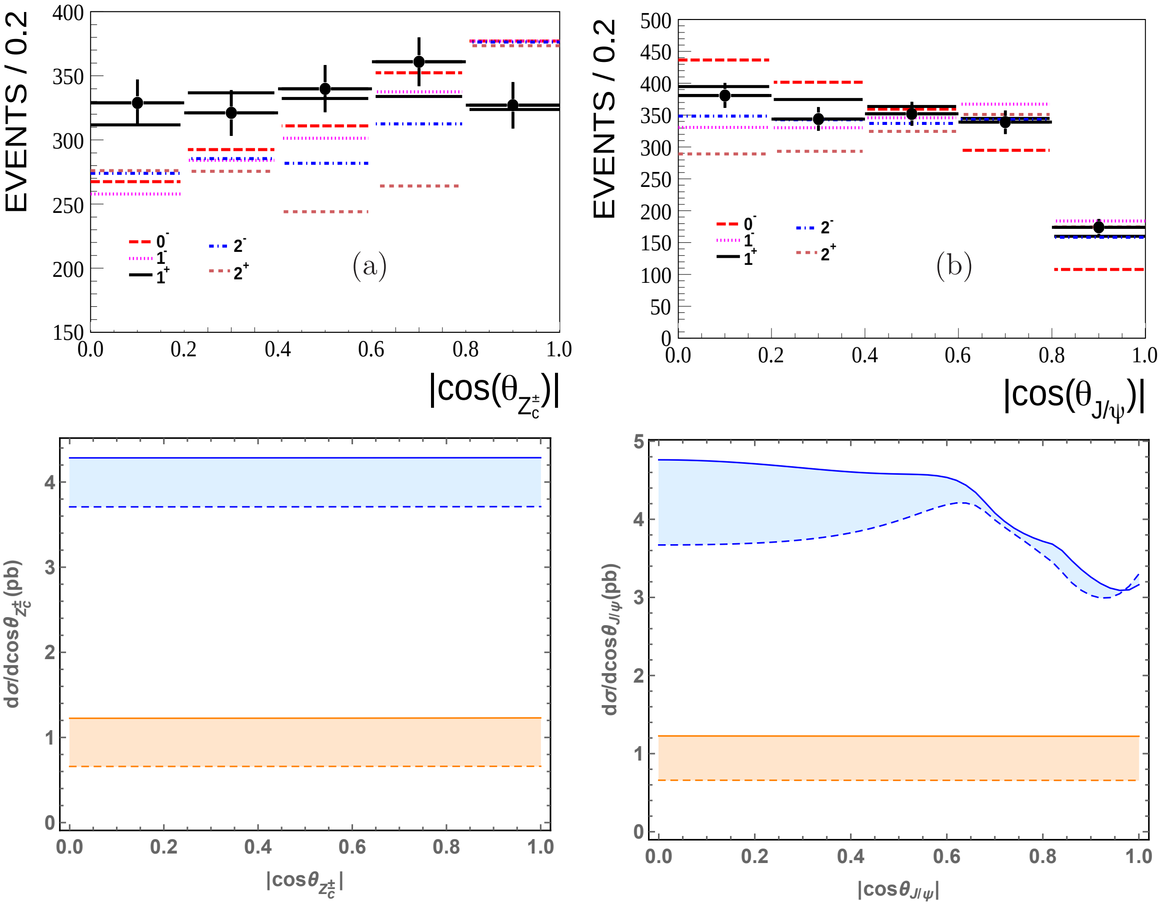

FIGURE 6.8: Angular distribution of $Z_c^\pm$ (left panels) and J/ψ (right panels), for $m_{J/\psi}$ around the mass of $Z_c(3900)$. The top panels show the combined experimental data compared to fit results with different J^P hypotheses from BESIII analysis [51]. The bottom panels show the outcome of our formalism, assuming the $Z_c(3900)$ is an axial-vector state, where the solid lines represent fit 1 and the dashed lines fit 2, with fit parameters given in Table 6.1. The blue curves show the results of all contributions while the orange ones show the contributions of the $Z_c(3900)$ only.

6.3 Summary

In this chapter, we provided a quantitative and simultaneous description of the $\pi^+\pi^-$ and $\pi^\pm J/\psi$ invariant mass distributions of the recent BESIII data on $e^+e^- \to J/\psi\ \pi^+\pi^-$ together with the total cross sections $\sigma(J/\psi K^+K^-)$ at e^+e^- center-of-mass energies $q = 4.23$ GeV and $q = 4.26$ GeV. A crucial element of our analysis is the well established charged exotic state $Z_c(3900)$, which we account for explicitly in t- and u-channels. The final state interaction of the two pions in the S- and D-waves is treated using the dispersion theory. For the S-wave, we consider coupled-channel unitarity since the kinematical region goes beyond the inelastic channel $K\bar{K}$ and the effect from the $f_0(980)$ resonance impacts significantly the observables. On the other hand, for the D-wave a single-channel Omnès approach is adopted since the lowest resonance in that channel, the $f_2(1270)$ tensor resonance, decays predominantly into two pions. The final amplitudes depend on a set of subtraction constants, which have been fitted to the BESIII data. A simultaneous description of $\pi^+\pi^-$ and $\pi^\pm J/\psi$ mass distributions together with the cross sections $\sigma(J/\psi K^+K^-)$ is achieved through a four-parameter fit. We showed that the latter can be further improved by adding phases to the subtraction constant and allowing for one subtraction in the D-wave contribution. We found that the resulting seven parameter fit yields a very good description of the $\pi^+\pi^-$ and $\pi^\pm J/\psi$ mass distributions together with the cross sections $\sigma(J/\psi K^+K^-)$. Our dispersive formalism shows that besides the direct production of the Z_c, responsible for the peak regions in the $\pi\psi$ distributions, the two pions are predominantly produced through a contact term in the transition from the Y state to the J/ψ state and subsequently rescatter. For the $e^+e^- \to J/\psi\, K\bar{K}$ we provided the first theoretical prediction for the two-kaon invariant mass distribution, which is significantly different from the pure phase space.

Moreover, we determined the angular distributions of J/ψ and $Z_c(3900)$ which have qualitatively the same behavior as the experimental data. However, the distributions of J/ψ are not symmetric around zero and very sensitive to the integration limits. A more significant cross check could be achieved by comparing the distributions at fixed e^+e^--CM energies and for the full interval from -1 to 1 of $\cos\theta_{J/\psi}$.

The constructed amplitudes provide powerful tools to analyze future data by the BESIII and Belle II Collaborations. It can also be readily applied to study e^+e^- annihilation into $\Upsilon(nS)\pi^+\pi^-$, where charged bottomonia like $Z_b^\pm$ states have been observed.

Chapter 7

$e^+e^- \to h_c\,\pi^+\pi^-$

In Chapters 5 and 6, we focused on the charged exotic state $Z_c^\pm(3900)$, which appear as sharp structures in the $\psi(2S)\pi^\pm$ and $J/\psi\pi^\pm$ mass spectra of the reactions $e^+e^- \to \psi(2S)\,\pi^+\pi^-$ and $e^+e^- \to J/\psi\,\pi^+\pi^-$. In this chapter we study the Dalitz plot projections of the process $e^+e^- \to h_c\,\pi^+\pi^-$. This reaction is of special interest because a narrow charged exotic state was also observed in the $h_c\pi^\pm$ mass spectrum by the BESIII collaboration in 2013 [128]. The distinct structure was observed around 4.02 GeV, which was therefore named $Z_c^\pm(4020)$. Similar to the $Z_c(3900)$, the $Z_c(4020)$ is a triplet (isospin 1), since the neutral spin partner was found in $e^+e^- \to h_c\pi^0\pi^0$ [129]. In the same mass region an exotic structure was detected in the processes $e^+e^- \to (D^*\bar{D}^*)^\pm\pi^\mp$ [126] and $e^+e^- \to (D^*\bar{D}^*)^0\pi^0$ [127]. It has been discussed whether these two structures can be considered the same state, however in order to do so, a consistent study in needed to determine their quantum numbers.

In this chapter, we study the invariant mass distributions of the process $e^+e^- \to h_c\,\pi^+\,\pi^-$ at e^+e^--CM energies $q = 4.23$ and 4.26 GeV. The experimental data used in the analyses was obtained from a private communication with the BESIII collaboration. The distributions for the combined data for all measured energies can be found in Ref.[128]. Analogous to the reaction $e^+e^- \to \psi(2S)\,\pi^+\,\pi^-$ studied in Chapter 5, we use the single channel approach for the $\pi\pi$ final state interaction (FSI), since the physical region lies below the $K\bar{K}$ threshold. In this way, the contributions of the $\pi\pi$ rescattering are taken into account through the single channel Omnès formalism, which uses as input the $\pi\pi$ phase shift as discussed in Chapter 3. We consider explicitly the charged exotic state $Z_c(4020)$ as an exchange intermediate state in the t- and u-channels. In addition, we also compare whether the $Z_c(3900)$ can improve the physical description of the invariant distributions. We explain the dispersive formalism for this particular process in Section 7.1 and the description of the invariant mass distributions are shown in Section 7.2. This project is the beginning of a formalized collaboration between the theory group in Mainz with the BESIII collaboration for studying exotic states in e^+e^- collisions.

7.1 Dispersive Formalism

In this section we study the invariant mass distributions of $e^+e^- \to h_c\,\pi^+\pi^-$ using a single-channel dispersive formalism, similar to the one discussed in Chapter 5 for the $e^+e^- \to \psi(2S)\,\pi^+\pi^-$. However, the quantum numbers of the charmonium in the final state are different, which requires some adjustments in the approach. The J^{PC} quantum numbers for the current case are

$$\gamma^*(1^{--}) \to h_c(1^{+-})\,\pi^+(0^-)\,\pi^-(0^-), \tag{7.1}$$

where J is the total angular momentum, P is the parity and C is the charge conjugation. Considering charge conjugation and parity conservation in the process we observe that there must be an odd relative angular momentum between h_c and the pion-pair. Notice that the $\pi\pi$ system cannot be in an odd wave state, such as a relative P-wave, because this violates C-symmetry. Since the phase space of this reaction is small, we can assume that the $\pi\pi$ is in S-wave in our dispersive formalism for the final state interaction. Analogous to Chapter 5, because the isospin of the pion-pair is zero, we omit the isospin index for simplicity.

The double differential cross section for the process

$$e^-(p_1)\,e^+(p_2) \to \gamma^*(p_{\gamma^*}) \to h_c(p_{h_c})\,\pi^+(p_{\pi^+})\,\pi^-(p_{\pi^-}) \tag{7.2}$$

is the same as for the previous process given in Eq.(5.1), with the helicity amplitudes $\mathcal{H}_{\lambda_1\lambda_2}$ defined in the usual way,

$$\begin{aligned} \langle \pi\pi h_c(\lambda_2)|\,\mathcal{T}\,|\gamma^*(\lambda_1)\rangle &= (2\pi)^4\,\delta(p_{\gamma^*} - p_{h_c} - p_{\pi^+} - p_{\pi^-})\,\mathcal{H}_{\lambda_1\lambda_2}, \\ \mathcal{H}_{\lambda_1\lambda_2} &\equiv \mathcal{H}^{\mu\nu}\epsilon_\mu(p_{\gamma^*},\lambda_1)\,\epsilon^*_\nu(p_{h_c},\lambda_2)\,, \end{aligned} \tag{7.3}$$

where $\lambda_1(\lambda_2)$ denote the $\gamma^*(h_c)$ helicities, respectively. Notice that as explained in

Chapter 5, the quantity $\sum_{\lambda_1\lambda_2} |\mathcal{H}_{\lambda_1\lambda_2}|^2$ is Lorentz invariant and it is convenient to calculate it in the $\pi\pi$-CM in our formalism. Thus, we choose the following Mandelstam variables

$$\begin{aligned} s &= (p_{\pi^+} + p_{\pi^-})^2 \equiv M^2_{\pi^+\pi^-} \,, \\ t &= (p_{h_c} + p_{\pi^+})^2 \equiv M^2_{h_c\pi^+} \,, \\ u &= (p_{h_c} + p_{\pi^-})^2 \equiv M^2_{h_c\pi^-}, \end{aligned} \tag{7.4}$$

which satisfy $s + t + u = q^2 + m^2_{h_c} + 2m^2_\pi$.

7.1.1 Final State Interaction

The amplitudes in Eq.(7.3) encode the physics which describes the invariant mass distributions. In Chapters 5 and 6, we derived a dispersive formalism for these amplitudes. In summary, the helicity amplitude can be parametrized in terms of the exchange of charged intermediate mesons ($\mathcal{H}^{Z_c}_{\lambda_1\lambda_2}$) and the final state interaction of pions ($\mathcal{H}^{\text{FSI}}_{\lambda_1\lambda_2}$), as given by

$$\mathcal{H}_{\lambda_1\lambda_2} = \mathcal{H}^{Z_c}_{\lambda_1\lambda_2} + \mathcal{H}^{\text{FSI}}_{\lambda_1\lambda_2}. \tag{7.5}$$

The amplitudes $\mathcal{H}^{Z_c}_{\lambda_1\lambda_2}$ are discussed in the next section. The term corresponding to the $\pi\pi$ final state interaction can be expressed as

$$\mathcal{H}^{\text{FSI}}_{\lambda_1\lambda_2} = f_c(s)\,\Omega(s)\,\tilde{a}, \tag{7.6}$$

where $\tilde{a}$ is a fitting parameter and $f_c(s)$ is the centrifugal barrier factor,

$$f_c(s) = \frac{\sqrt{(q^2 - (\sqrt{s} + m_{h_c})^2)(q^2 - (\sqrt{s} - m_{h_c})^2)}}{2q}, \tag{7.7}$$

which takes into account the relative angular momentum $l = 1$ between the system of two pions and h_c. In Eq.(7.6), $\Omega(s)$ is the Omnès function for S-wave and isospin 0, which is given in Eq.(3.29). Notice that in contrast to Eqs.(5.10) and (6.14) for the FSI in the previous chapters, we do not include the rescattering contribution through Z_c in Eq.(7.6), since we observed that its contributions are small and can be neglected.

7.1.2 Exchange Mechanism

In our representation, we approximate the left-hand cut contribution by the exchange of intermediate charmoniumlike charged states in the t and u channels. Based on the experimental data, the mechanism $\gamma^*(q^2) \to \pi^\pm + (Z_c^\mp \to h_c + \pi^\mp)$ is assumed to be the dominant one. Assuming Z_c as an axial-vector state, the amplitudes for the process can be written in a general form as,

$$\mathcal{H}^{Z_c}_{\lambda_1\lambda_2} = (V_{Z_c h_c \pi})^{\beta\nu}\, S_{\nu\mu}(Q_z)\, (V_{\gamma^*\pi Z_c})^{\mu\alpha}\, \epsilon_\alpha(p_{\gamma^*},\lambda_1)\, \epsilon^*_\beta(p_{h_c},\lambda_2), \tag{7.8}$$

where $S_{\nu\mu}(Q_z)$ is the axial meson propagator,

$$S_{\nu\mu}(Q_z) = \frac{-g^{\nu\mu} + Q_z^\nu Q_z^\mu/m_z^2}{Q_z^2 - m_z^2 + i m_z \Gamma_z} \tag{7.9}$$

and the vertices

$$(V_{Z_c h_c \pi})^{\beta\nu} = -2\, C_{Z_c h_c \pi}\, \epsilon^{\beta\nu}{}_{\rho\delta}\, p^\rho_{h_c} Q^\delta_z, \tag{7.10}$$

$$(V_{\gamma^*\pi Z_c})^{\mu\alpha} = \mathcal{F}_{\gamma^*\pi Z_c}(q^2)\, \left[g^{\alpha\mu}\,(p_{\gamma^*}\cdot Q_z) - p^\mu_{\gamma^*} Q^\alpha_z\right], \tag{7.11}$$

where $Q_z = (p_{\gamma^*} - p_\pi)$. The form factor $\mathcal{F}_{\gamma^*\pi Z_c}(q^2)$ in Eq.(7.11) has a physical meaning only for the on-shell pion and Z_c meson. The absolute value squared of the total amplitude is obtained by the sum of the squares of each helicity amplitude, that means

$$|\mathcal{H}_{tot}|^2 = \sum_{\lambda_{\gamma^*}\lambda_{h_c}} |\mathcal{H}_{\lambda_{\gamma^*}\lambda_{h_c}}|^2. \tag{7.12}$$

Due to parity, the helicity amplitudes can be reduced from 9 to 5 independent ones: $\mathcal{H}_{++}$, $\mathcal{H}_{+-}$, $\mathcal{H}_{+0}$, $\mathcal{H}_{0+}$ and $\mathcal{H}_{00}$. We observe that $\mathcal{H}^{Z_c}_{+-} = \mathcal{H}^{Z_c}_{00} = 0$, while $\mathcal{H}^{Z_c}_{+0}$ and $\mathcal{H}^{Z_c}_{0+}$ are very small compared to $\mathcal{H}^{Z_c}_{++}$. Therefore, for our particular kinematics we use the following approximations, which simplifies our formalism,

$$\sum_{\lambda_1\lambda_2} |\mathcal{H}^{Z_c}_{\lambda_1\lambda_2}|^2 \approx 2\,|\mathcal{H}^{Z_c}_{++}|^2 \quad \to \quad \sum_{\lambda_1\lambda_2} |\mathcal{H}_{\lambda_1\lambda_2}|^2 \approx 2\,|\mathcal{H}_{++}|^2. \tag{7.13}$$

This approximation avoids facing issues with the effects of kinematic constraints, except for the centrifugal factor, which we explicitly took out in Eq.(7.7). As a result, the use of the invariant amplitude formalism is not necessary, as discussed in the previous chapters.

7.2 Results and Discussion

The experimental data for the process $e^+e^- \to h_c\,\pi^+\,\pi^-$, measured by the BESIII collaboration [128], is shown in Fig.7.1. The data is however combined for all measured energies in the range from 3.900 to 4.420 GeV. In our formalism the fit parameters are e^+e^--CM energy (q) dependent, therefore in order to analyse the process we need the data sets for individual q energies. We obtained the experimental data for the mass distributions $\pi^+\pi^-$ and $h_c\pi^\pm$ at $q = 4.23$ GeV and $q = 4.26$ GeV, through private communications. These are the energies with the highest statistics, furthermore the reactions $e^+e^- \to \psi(2S)\,\pi^+\,\pi^-$ and $e^+e^- \to J/\psi\,\pi^+\,\pi^-$ were also studied at these energies, which enables us to compare the three different reactions at the same e^+e^--CM energy. In this section we show the results of our fits, however we cannot disclose the data for the individual energies.

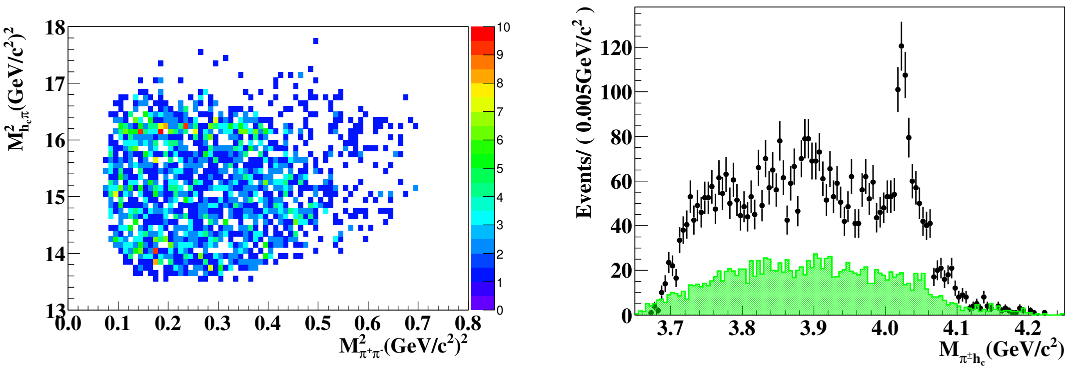

FIGURE 7.1: Experimental data of the process $e^+e^- \to h_c\,\pi^+\,\pi^-$ measured by the BESIII collaborations Ref.[128]. The left panel exhibits the Dalitz plot events, summed over the e^+e^--CM energy range from 3.900 to 4.420 GeV. On the right hand side, the black dots represent the corresponding $M_{\pi^\pm h_c}$ distribution, where the green histograms display the normalized sideband background region.

As already explained in the previous sections, our theoretical formalism consists in using explicitly the charged exotic states as intermediate particles and including the $\pi\pi$-FSI through a single channel dispersive approach. To account for the sharp structures in the $h_c\pi^\pm$ invariant mass distributions we consider explicitly the charged exotic state $Z_c(4020)$ as the intermediate state in the t- and u-channels. In addition, we also compare whether including the $Z_c(3900)$ can improve the physical description of the invariant distributions. Therefore the helicity amplitude given in Eq.(7.5) expressed in terms of the $Z_c(3900)$ and $Z_c(4020)$ exchange and the $\pi\pi$-FSI is given by

$$\mathcal{H}_{++}(s,t) = \mathcal{H}_{++}^{Z_c(4020)}(s,t) + g\,\mathcal{H}_{++}^{Z_c(3900)}(s,t) + f_c(s)\,\Omega(s)\,\tilde{a}. \tag{7.14}$$

The Z_c-exchange amplitude $\mathcal{H}_{++}^{Z_c}$ is obtained from Eq.(5.21),

$$\mathcal{H}_{++}^{Z_c} = \frac{N_r(s,t)}{t - m_z^2 + im_z\Gamma_z} + \frac{N_r(s,u)}{u - m_z^2 + im_z\Gamma_z}, \tag{7.15}$$

with the numerators given by

$$\begin{aligned} N_r(s,t) =& \frac{1}{8\sqrt{\lambda\left(s,q^2,m_{h_c}^2\right)}}\Big\{\lambda\left(s,q^2,m_{h_c}^2\right)\left(\Sigma_m + 2(m_\pi^2 + q^2 - s)\right) \\ &+ (\Sigma_m - 2t - s)\left[(q^2 - m_{h_c}^2)\left(\Sigma_m - 2t - 4q^2\right) + (5q^2 + 3m_{h_c}^2)s - 2s^2\right]\Big\}, \end{aligned} \tag{7.16}$$

where

$$\Sigma_m = 2m_\pi^2 + m_{h_c}^2 + q^2 \tag{7.17}$$

Notice that the parameter g is the ratio between the coupling constants of $Z_c(3900)$ and $Z_c(4020)$. Consequently, for the fits without $Z_c(3900)$ one can simply set g to zero. The coupling constants of $Z_c(4020)$ can be factored out with the normalization factor in the cross section as shown below,

$$\frac{d^2\sigma}{ds\,dt} = \frac{N_1}{2^5(2\pi)^3q^6}\,\frac{1}{3}\,2\,|\mathcal{H}_{++}(s,t)|^2\,f_{\text{pb}}, \tag{7.18}$$

where $N_1 = |eC_{Z_ch_c\pi}\mathcal{F}_{\gamma^*\pi Z_c}|^2$, $a = \tilde{a}/C_{Z_ch_c\pi}\mathcal{F}_{\gamma^*\pi Z_c}$ and considering the cross section conversion factor from GeV^{-2} to pb, $f_{\text{pb}} = 389.379\cdot 10^6$ pb/GeV^2.

With Eqs.(7.14) and (7.18) we are able to simultaneously fit the $M_{\pi^+\pi^-}$ and $M_{h_c\pi^\pm}$ mass distributions at $q = 4.23$ GeV and $q = 4.26$ GeV. We investigate two scenarios, a two-parameter fit, considering only the $Z_c(4020)$ as an intermediate state and a three-parameter fit, including not only the $Z_c(4020)$ but also $Z_c(3900)$. Both fits take into account the single channel $\pi\pi$-FSI. The line shape of the invariant mass distribution

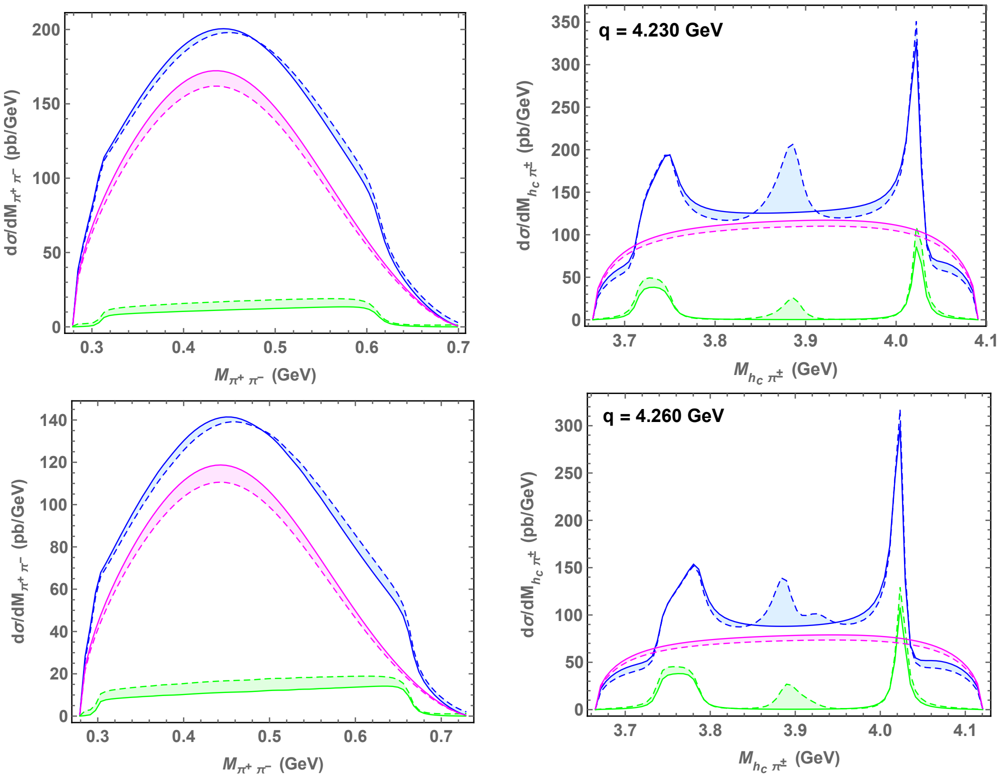

FIGURE 7.2: Dalitz projections at e^+e^--CM energies $q = 4.23$ GeV (top panels) and $q = 4.26$ GeV (bottom panels). The solid lines represent fit 1 (without $Z_c(3900)$) and the dashed lines fit 2 (with $Z_c(3900)$), where the shaded area indicates the spread between the fits. The blue curves show the results using all fit parameters, with parameters given in Table 7.1. The combined contributions of the $Z_c(4020)$ and $Z_c(3900)$ is displayed by the green curves, while the $\pi\pi$-FSI is shown by the magenta curves.

obtained with our fits are shown in Fig.7.2, which also displays the individual contribution of the Z_c-background and $\pi\pi$-FSI. The parameter $N_1(q)$ is a global normalization which contains the coupling constants of $Z_c(4020)$ and the parameter $\tilde{a}(q)$ adjusts the contribution of the pions re-scattering. Both parameters are energy q dependent, but because of the small energy difference of 0.03 GeV, we expect the parameters to have similar values. This behavior is consistent with our fit results given in Table 7.1. The parameter g is the ratio between the coupling constants of $Z_c(4020)$ and $Z_c(3900)$ and is compatible with 1, which means that both charged exotic states evenly contribute to the fit in the second scenario. The inclusion of the $Z_c(3900)$ in our fits provides an equally good fit result or even a slight improvement, as can be seen by the χ^2_{red} values. This observation leads to the conclusion that we cannot rule out the existence of the $Z_c(3900)$ in this process at these energies.

Using the parameters in Table 7.1, we can also provide a prediction for the angular

q (GeV)	Scenario	$N_1 \cdot 10^6$ (GeV^{-4})	$\tilde{a} \cdot 10^{-3}$ (GeV^2)	g	χ^2_{red}
4.23	Only $Z_c(4020)$	5.4 (1.2)	-1.68 (21)	-	1.95
	$Z_c(4020) + Z_c(3900)$	6.9 (1.3)	-1.44 (17)	0.93 (21)	1.82
4.26	Only $Z_c(4020)$	5.5 (1.2)	-1.29 (16)	-	1.18
	$Z_c(4020) + Z_c(3900)$	6.6 (1.3)	-1.14 (14)	1.08 (32)	1.14

TABLE 7.1: Fit parameters entering in Eqs.(7.18) and (7.14) for the two different e^+e^--CM energies q. We use $m_{z_1} = 4.024$ GeV, $m_{z_2} = 3.8884$ GeV, $\Gamma_{z_1} = 13$ MeV and $\Gamma_{z_2} = 28.3$ MeV.

distribution of h_c, analogously as done in Chapter 6 for the process $e^+e^- \to J/\psi\,\pi^+\pi^-$. Therefore the Eq.(6.20) becomes

$$\frac{d\sigma}{d\cos\theta_{h_c}} = \int_{t_i}^{t_f} dt\, \frac{d^2\sigma}{ds\,dt}\, \frac{ds}{d\cos\theta_{h_c}}, \tag{7.19}$$

where θ_{h_c} is the polar angle of h_c in the Z_c rest frame (see Fig.D.1) and the s dependence on $\cos\theta_{h_c}$ is the same as given in Eq.(6.21). As discussed previously the integral in Eq.(7.19) is very sensitive to the integration limits of t, therefore in this case we integrate over the full Dalitz plot range, $t_i = (m_{h_c} + m_\pi)^2$ and $t_f = (q - m_\pi)^2$. Our prediction for the angular distribution of h_c at energies $q = 4.23$ GeV and $q = 4.26$ GeV is displayed in Fig.7.3, assuming the $Z_c(4020)$ to be an axial-vector. This result can be used to determine the quantum numbers of $Z_c(4020)$ by comparing with future experimental data.

7.3 Summary

In this chapter, we studied the invariant mass distribution of the process $e^+e^- \to h_c\,\pi^+\,\pi^-$ at $q = 4.23$ GeV and $q = 4.26$ GeV. To account for the pions rescattering we use a single channel Omnès approach, considering a relative angular momentum $l = 1$ between the pion-pair and the h_c. We considered explicitly the charged exotic state $Z_c(4020)$ as intermediate state in the t- and u-channel and investigated two scenarios with and without including the $Z_c(3900)$. For both cases we find that our fits describe the experimental data very well, which leads to the conclusion that it is not possible to rule out the presence of the $Z_c(3900)$ at these e^+e^--CM energies. Additionally,

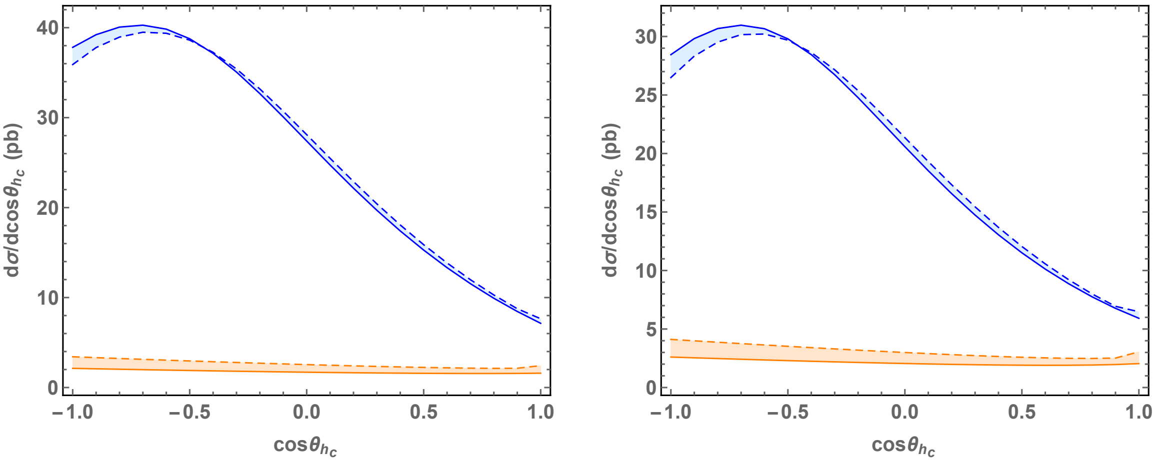

FIGURE 7.3: Angular distribution of h_c at e^+e^--CM energies $q = 4.23$ GeV (left panel) and $q = 4.26$ GeV (right panel), under the assumption that the Z_c states are axial vectors. The solid lines represent fit 1 (without $Z_c(3900)$) and the dashed lines fit 2 (with $Z_c(3900)$), where the parameters are given in Table 7.1. The blue curves show the results using all fit parameters while the orange ones show the contributions of the Z_c only.

we predict the angular distributions of h_c, assuming the $Z_c(4020)$ to be an axial-vector, which can be utilized to cross-check this quantum number by comparison to forthcoming data.

Chapter 8

Conclusions and Perspectives

In this thesis we analyzed the impact of intermediate exotic states and $\pi\pi$ FSI based on the dispersion theory. Despite the fact that we focused on specific processes where electron and positron annihilate into two pions and a hidden-charm meson, our formalism can be extended to other reactions, with the main requirement of having high statistical invariant mass distributions for each center of mass energy.

First, we studied the reaction $e^+e^- \to \psi(2S)\,\pi^+\pi^-$ at four different e^+e^--CM energies q. We assume charged exotic mesons are created as intermediate states

$$e^+e^- \to \gamma^* \to Z_c^\pm\,\pi^\mp \to \psi(2S)\,\pi^+\,\pi^-,$$

and additionally, we considered the rescattering of pions within a single-channel dispersive approach.

For the energies $q = 4.226$ GeV and $q = 4.258$ GeV, we find that the established exotic state $Z_c(3900)$ is essential to explain the peaks in the invariant mass distributions. This is the first scientific work to show that the decay $Z_c(3900) \to \psi(2S)\,\pi$ is possible.

For $q = 4.358$ GeV, our approach indicated that no intermediate Z_c state is needed to describe both $\psi\pi$ and $\pi\pi$ line shapes. Taking only the $\pi\pi$ FSI into account, without Z_c as a left-hand cut, is sufficient to explain the experimental data well.

For the highest energy $q = 4.416$ GeV, we studied in detail whether a new heavier charged state is necessary to explain the sharp narrow structure. A scan search was performed to determine which mass and width for the intermediate state gives the best description of the invariant mass distributions at this energy. The best description of the experimental data was obtained with the following values:

$$\begin{aligned} m_{Z_c} &= 4.016(4)\ \text{GeV}, \\ \Gamma_{Z_c} &= 52(10)\ \text{MeV}. \end{aligned}$$

We observed that the known state $Z_c(4020)$ has a compatible mass, which implies that the charged charmonium-like structure observed at this energy might not necessarily be a new state.

Finally, we conclude that for all the e^+e^--CM energies in the process $e^+e^- \to \psi(2S)\,\pi^+\pi^-$, while the presence of an intermediate state must be carefully analyzed for each q, the $\pi\pi$ FSI is always the main mechanism to describe the $\pi\pi$ invariant mass distribution.

Next, we analyzed the reaction $e^+e^- \to J/\psi\,\pi^+\pi^-$ at at e^+e^--CM energies $q = 4.23$ GeV and $q = 4.26$ GeV. We applied a similar formalism as previously,

$$e^+e^- \to \gamma^* \to Z_c^\pm(3900)\,\pi^\mp \to J/\psi\,\pi^+\,\pi^-,$$

where the well established charged exotic state $Z_c(3900)$ is taken into account explicitly in t- and u-channels as well as the $\pi\pi$ FSI. For this process specifically at these energies, the phase space is much larger than in our previous case, going beyond the first relevant inelastic threshold in the $\pi\pi$ region. This fact asks for a coupled-channel formalism where pions and kaons are treated together in a matrix equation. Consequently, both reactions $e^+e^- \to J/\psi\,\pi^+\pi^-$ and $e^+e^- \to J/\psi\,K^+K^-$ must be analysed in a combined approach. Thus, we describe the $\pi^+\pi^-$ and $\pi^\pm J/\psi$ invariant mass distributions simultaneously at both energies using the total cross sections $\sigma(J/\psi K^+K^-)$ as a constraint in our fits. Note that the experimental data for $J/\psi K$ and $K\bar{K}$ line shapes currently is not available.

In addition to the S-wave, we also include the D-wave $\pi\pi$ FSI within our dispersive formalism. For the D-wave though, a single-channel Omnès approach is adopted, given that the nearest resonance in that channel is the $f_2(1270)$ tensor resonance, which decays predominantly into two pions.

We consider different scenarios by analyzing the importance of the subtraction constants. Our simplest case, a four-parameter fit, can simultaneously describe the $\pi^+\pi^-$ and $\pi^\pm J/\psi$ mass distributions well, together with the cross-sections $\sigma(J/\psi K^+K^-)$. The fits can be further improved by adding phases to the subtraction constant and allowing for one subtraction in the D-wave contribution.

The peaks in the $\pi\psi$ distributions are explained by the direct production of the $Z_c(3900)$, in other words, the $Z_c(3900)$ is necessary to describe the data. However by themselves they do not yield a good description of the $\pi\pi$ mass distributions. Our findings show that the dominant term to explain the $\pi\pi$ mass distribution results from a contact term between the virtual photon and the three final states, with the subsequent $\pi\pi$ rescattering.

Furthermore, our approach also provides predictions for the invariant mass distributions in the reaction $e^+e^- \to J/\psi\, K\bar{K}$, since we used a coupled-channel formalism with pions and kaons. At these energies there is no exotic state in the strange sector, due to the fact that the energy is not high enough to create an intermediate state with a mass slightly larger than $Z_c(3900)$. Consequently, our predictions are dominated by contact terms together with Omnès functions for pions and kaons. The obtained mass distribution is significantly different from the pure phase space due to the $f_0(980)$ resonance and we expect to see it in future experimental measurements.

We also applied our dispersive formalism for the process $e^+e^- \to h_c\,\pi^+\pi^-$ at at e^+e^--CM energies $q = 4.23$ GeV and $q = 4.26$ GeV. In this case, we considered the charged exotic meson $Z_c(4020)$ as the intermediate state,

$$e^+e^- \to \gamma^* \to Z_c^\pm(4020)\,\pi^\mp \to h_c\,\pi^+\,\pi^-.$$

Additionally, we investigate whether the $Z_c(3900)$ improves the physical description. Due to the small phase space, we used a single-channel Omnès approach for the $\pi\pi$ FSI. We obtained equally good descriptions of the experimental data including only the $Z_c(4020)$ as well as including both $Z_c(4020)$ and $Z_c(3900)$ as intermediate states. This leads to the conclusion that we cannot rule out the presence of $Z_c(3900)$ in this process at these energies. Furthermore, we provide predictions for the angular distributions of h_c at both e^+e^--CM energies, under the assumption that the $Z_c(4020)$ state is an axial-vector. This result can be used in conjunction with forthcoming data to experimentally determine the quantum number of the respective exotic state.

For all the process analyzed in this thesis, we observed that the inclusion of the $Z_c(3900)$ as an intermediate state results in a good description of the experimental data at e^+e^--CM energies $q = 4.23$ GeV and $q = 4.26$ GeV. This finding can be interpreted as an indication that the $Z_c(3900)$ has the following decay modes:

$$Z_c(3900) \to \psi(2S)\pi^\pm\,, \quad Z_c(3900) \to J/\psi\pi^\pm\,, \quad Z_c(3900) \to h_c\pi^\pm\,.$$

The dispersive formalism applied in this thesis is a powerful tool to analyze final state interactions in the experimental data. The minimal requirement of our approach is the information about the phase shifts or the amplitudes of the outgoing states and the Dalitz data of three body decays.

We can extend our formalism to analyse the total cross section of the three reactions studied in this thesis. The experimental data is shown in Fig.8.1. It is possible to reconstruct the line shape of the total cross sections if our formalism is applied to enough different energy values q. In this way, one could investigate whether the experimental assumption of two exotic Y states (1^{--}) is an accurate representation for describing the enhancements in the data.

Another possible extension of the formalism proposed in this thesis is to investigate the existence of strange exotic states (Z_{cs}). This can be immediately implemented by analysing reactions such as $e^+e^- \to (c\bar{c})\,K^+K^-$ at energies higher than 4.5 GeV in order to have enough energy to create the strange partner of $Z_c(3900)$, the lightest charged exotic state measured so far. Evidence of Z_{cs} states was observed very recently by the BESIII collaboration in the reaction $e^+e^- \to K^+(D_s^- D^{*0} + D_s^{*-} D^0)$ [136] and the LHCb collaboration in the reaction $B^+ \to J/\psi\phi K^+$ [137]. This findings could consolidate the hypothesis that the charged exotic states have indeed a substructure containing four quarks.

So far, we have only focused on charmonium states, however the formalism can also be applied to the bottomonium sector. Since the quantum numbers of the particles in the process $e^+e^- \to \Upsilon(nS)\pi^+\pi^-$, where charged bottomonium Z_b states were found [138],

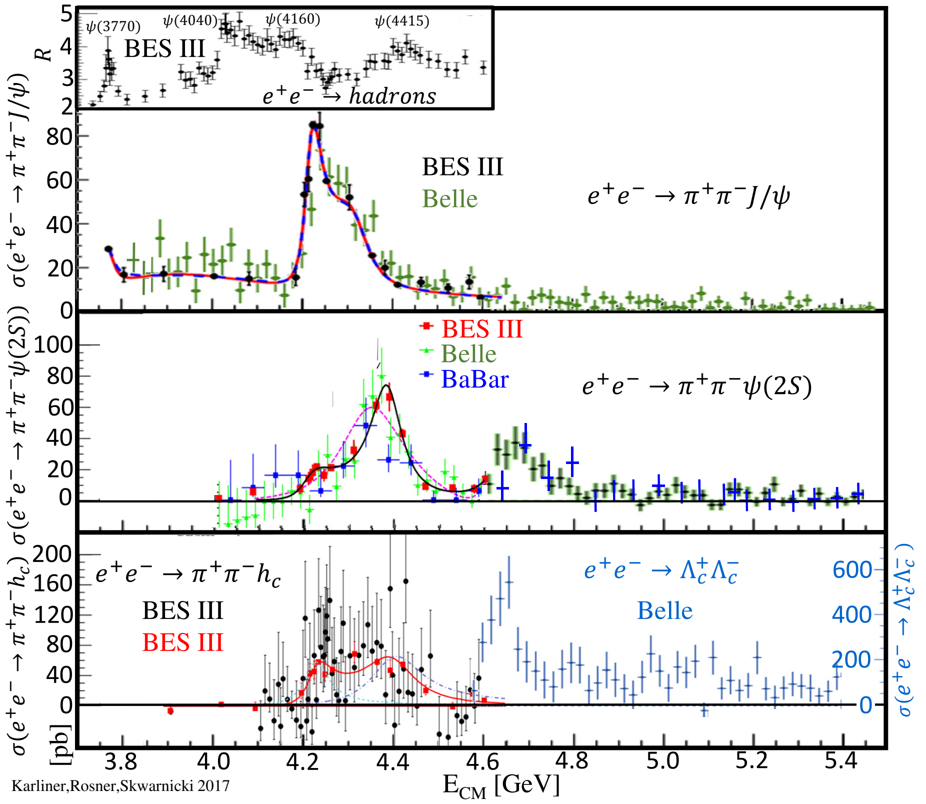

Karliner,Rosner,Skwarnicki 2017

FIGURE 8.1: Experimental data for the total cross section for the processes $e^+e^- \to J/\psi\,\pi^+\pi^-$ (top), $e^+e^- \to \psi(2S)\,\pi^+\pi^-$ (middle) and $e^+e^- \to h_c\,\pi^+\pi^-$ (bottom). This summary plot was extracted from Ref.[135].

are the same, we could perform an analogous analysis for this reaction. Moreover, this formalism provides a powerful tools to analyze the upcoming data from the Belle II Collaboration.

Due to the success of this work, we started a collaboration with the BESIII-Experiment to apply our approach for the complete data sample and new measurements of the reactions $e^+e^- \to \psi(2S)\,\pi^+\pi^-$, $e^+e^- \to J/\psi\,\pi^+\pi^-$, $e^+e^- \to J/\psi\,K\bar{K}$ and $e^+e^- \to h_c\,\pi^+\pi^-$ at e^+e^- CM energies in the range from 4.0 GeV to 4.6 GeV. This will improve the determination of the masses, widths and the quantum numbers as well as the production and decay mechanism of the exotic resonances, therefore providing a better understanding of their nature.

Appendix A

Inverse Amplitude Method

In this appendix we derive the inverse amplitude method (IAM), based on Ref.[90, 92, 139–141]. The IAM is a unitarization technique, which enlarges the range of validity of ChPT using the appropriate cut structure. Since the method works for every partial wave amplitude, the indices for isospin (I) and angular momentum (J) are omitted for simplicity. We will apply the IAM to the $\pi\pi$-scattering in Chapter 3, this allows us to determine the phase shift at low energy.

In the previous sections we saw that the initial and final states of a scattering process can be related with the S-matrix Eq.(2.40). The conservation of flux ensures that the S-matrix is unitary. From that, one can see that the scattering amplitude $t(s)$ is complex. Therefore, from Eq.(2.11), we can obtain the elastic unitary equation

$$\mathrm{Im}[t(s)] = \sigma(s)|t(s)|^2. \tag{A.1}$$

A similar equation can be written for the inverse amplitude. First, we observe that the imaginary part of the inverse of $t(s)$ can be written as

$$\mathrm{Im}\left[\frac{1}{t(s)}\right] = \mathrm{Im}\left[\frac{t(s)^*}{|t(s)|^2}\right] = \frac{-\mathrm{Im}\left[t(s)\right]}{|t|^2}. \tag{A.2}$$

Comparing Eq.(A.2) with Eq.(A.1), one gets the unitary equation for the inverse of the amplitude

$$\mathrm{Im}\left[\frac{1}{t(s)}\right] = -\sigma(s). \tag{A.3}$$

The ChPT amplitude only satisfies the unitarity condition in Eq.(A.1) perturbatively,

$$\begin{aligned} \mathrm{Im}\,[t_{\mathrm{LO}}] &= 0, \\ \mathrm{Im}\,[t_{\mathrm{NLO}}] &= \sigma\, |t_{\mathrm{LO}}|^2, \end{aligned} \tag{A.4}$$

with $t = t_{\mathrm{LO}} + t_{\mathrm{NLO}} + \cdots$. We can write a DR for the ChPT leading order (t_{LO}) and next to leading order (t_{NLO}) amplitudes as

$$t_{\mathrm{LO}}(s) = \sum_{l=0}^{k} a_l s^l, \tag{A.5}$$

$$t_{\mathrm{NLO}}(s) = \sum_{l=0}^{k} b_l s^l + \frac{s^k}{\pi} \int \frac{ds'}{s'^k} \frac{\mathrm{Im}\,[t_{\mathrm{NLO}}]}{s' - s - i\epsilon} + I_{LC}\,[t_{\mathrm{NLO}}]\,, \tag{A.6}$$

where k is the number of subtractions to obtain a convergent integral and I_{LC} is the left cut contribution. Since the inverse amplitude t^{-1} has the same analytic structure as t, up to possible pole terms due to zeros of t, we define a function

$$G(s) \equiv t_{\mathrm{LO}}^2 / t, \tag{A.7}$$

which also shares the same analytic structure. In this way, the dispersion relation for $G(s)$ is given by

$$G(s) = \sum_{l=0}^{k} g_l s^l + \frac{s^k}{\pi} \int \frac{ds'}{s'^k} \frac{\mathrm{Im}\,[G(s)]}{s' - s - i\epsilon} + I_{LC}\,[G(s)] + I_{\mathrm{PC}}, \tag{A.8}$$

where I_{PC} stands for possible pole contributions. The imaginary part of G(s) is simply

$$\mathrm{Im}\,[G(s)] = t_{\mathrm{LO}}^2 \frac{-\mathrm{Im}\,[t(s)]}{t^2} = t_{\mathrm{LO}}^2(-\sigma) = -\mathrm{Im}\,[t_{\mathrm{NLO}}]\,. \tag{A.9}$$

Consequently, if we rewrite the subtraction constants as

$$\sum_{l=0}^{k} g_l s^l = \sum_{l=0}^{k} a_l s^l - \sum_{l=0}^{k} b_l s^l, \tag{A.10}$$

$G(s)$ can be expressed as

$$G(s) \simeq t_{\mathrm{LO}}(s) - t_{\mathrm{NLO}}(s), \tag{A.11}$$

where the pole contribution was neglected and $I_{LC}\left[G(s)\right] = -I_{LC}\left[t_{\text{NLO}}\right]$ was considered. Therefore, from the definition of $G(s)$ in Eq.(A.7), we obtain the total amplitude

$$t(s) \simeq \frac{|t_{\text{LO}}(s)|^2}{t_{\text{LO}}(s) - t_{\text{NLO}}(s)}. \tag{A.12}$$

Adler Zeros

The IAM as summarized in Eq.(A.12) is a very successful unitarization technique, which only depends on the effective chiral constants up to a given order (in our case NLO) without any additional parameters or further approximations. However, the standard IAM fails to correctly reproduce the position where the amplitude is zero, the so-called Adler zeros, which is required by chiral symmetry [142, 143]. Furthermore, spurious poles emerge below threshold for the scalar waves (J=0). Despite the fact that this does not produce significant effects in the physical region, one can use a simple modification in the IAM that corrects the subthreshold region of the partial wave amplitudes [92, 94]. The modified inverse amplitude method (mIAM) is given by the following expression

$$t(s) = \frac{|t_{\text{LO}}(s)|^2}{t_{\text{LO}}(s) - t_{\text{NLO}}(s) + A^{\text{mIAM}}(s)}, \tag{A.13}$$

where

$$\begin{aligned} A^{\text{mIAM}}(s) = \left(\frac{t_{\text{LO}}(s)}{t'_{\text{LO}}(s_{\text{LO}})}\right)^2 \Bigg(& \frac{t_{\text{NLO}}(s_{\text{LO}})}{(s - s_{\text{LO}})^2} - \frac{(s_{\text{LO}} - s_A)}{(s - s_{\text{LO}})(s - s_A)} \times \\ & \left[t'_{\text{LO}}(s_{\text{LO}}) - t'_{\text{NLO}}(s_{\text{LO}}) + \frac{t_{\text{NLO}}(s_{\text{LO}}) t''_{\text{LO}}(s_{\text{LO}})}{t'_{\text{LO}}(s_{\text{LO}})}\right]\Bigg), \end{aligned} \tag{A.14}$$

with the Adler zero $s_A = s_{\text{LO}} + s_{\text{NLO}} + \mathcal{O}(p^6)$, thus $t_{\text{LO}}(s_{\text{LO}}) = 0$ and $t_{\text{LO}}(s_{\text{LO}} + s_{\text{NLO}}) + t_{\text{NLO}}(s_{\text{LO}} + s_{\text{NLO}}) = 0$. For the $\pi\pi$ scattering we have $t''_{\text{LO}}(s_{\text{LO}}) = 0$ and $t_{\text{LO}}(s)/t'_{\text{LO}}(s_{\text{LO}}) = s - s_{\text{LO}}$, which simplifies Eq.(A.14) for this case,

$$A^{\text{mIAM}}(s) = t_{\text{NLO}}(s_{\text{LO}}) - \frac{(s_{\text{LO}} - s_A)(s - s_{\text{LO}})}{(s - s_A)} \left[t'_{\text{LO}}(s_{\text{LO}}) - t'_{\text{NLO}}(s_{\text{LO}})\right]. \tag{A.15}$$

Appendix B

Triangle Loop Calculation

In this appendix we calculate in detail the triangle loop diagram using the Feynman parameterization and dispersion relations.

Triangle loop via Feynman parameterization

Feynman parameterization provides a general expression for rewriting a product of propagators

$$\frac{1}{D_1 \cdots D_n} = \Gamma(n) \int_0^1 dx_1 \cdots \int_0^1 dx_n \frac{\delta(1 - x_1 - \cdots - x_n)}{(x_1 D_1 + \cdots + x_n D_n)^n}. \tag{B.1}$$

For three propagators the equation above becomes

$$\frac{1}{D_1 D_2 D_3} = \Gamma(3) \int_0^1 da \int_0^{1-a} db \frac{1}{[a\, D_1 + b\, D_2 + (1 - a - b) D_3]^3}. \tag{B.2}$$

The triangle diagram shown in Fig.2.8 leads to the following choice

$$D_1 = (q + P_s)^2 - M_d^2, \tag{B.3}$$

$$D_2 = (q + P_a)^2 - \mu^2, \tag{B.4}$$

$$D_3 = q^2 - M_c^2. \tag{B.5}$$

For convenience, we rewrite the last term of equation (B.2) as

$$\frac{1}{[a\, D_1 + b\, D_2 + (1 - a - b) D_3]^3} = \frac{1}{(q^2 - 2qP - \Sigma)^3}, \tag{B.6}$$

where P and Σ are specific for each diagram, which in our case are given by

$$P = \frac{1}{2}(-2aP_s - 2bP_a), \tag{B.7}$$

$$\Sigma = -aM_c^2 + aM_d^2 - aP_s^2 - bM_c^2 + b\mu^2 - bP_a^2 + M_c^2. \tag{B.8}$$

Considering only scalar particles and using the dimensional regularization, see for example Ref.[144], we can solve a general D-dimensional integral for a a loop with N propagators using the Feymanm parametrization,

$$\int \frac{d^Dq}{(2\pi)^D} \frac{1}{(q^2 - 2qP - \Sigma)^N} = i\frac{\mu^{4-D}}{(4\pi)^{D/2}}(-1)^N(\Sigma + P^2)^{D/2-N}\frac{\Gamma(N - D/2)}{\Gamma(N)}, \tag{B.9}$$

where μ is the renormalization mass scale and Γ is the Gamma function. Consequently for $N \to 3$ and $D \to 4$, this reads

$$\int \frac{d^Dq}{(2\pi)^D} \frac{1}{(q^2 - 2qP - \Sigma)^3} = \frac{-i}{2(4\pi)^2}\frac{1}{\Sigma + P^2}. \tag{B.10}$$

Thus, the scalar triangle loop amplitude in the Eq.(2.88) gets

$$\mathcal{T} = \Gamma(3)\int_0^1 da \int_0^{1-a} db \frac{1}{2(4\pi)^2}\frac{1}{\Sigma + P^2} \tag{B.11}$$

where the first integration in db can be performed analytically and the last one in da numerically.

Triangle loop via Dispersion Relation

We start by looking the Eq.(2.88), which is the scalar triangle loop amplitude,

$$\mathcal{T} = -i\int \frac{d^4q}{(2\pi)^4} \frac{1}{q^2 - M_c^2} \frac{1}{(q + P_s)^2 - M_d^2} \frac{1}{(q + P_a)^2 - \mu^2}.$$

We calculate the discontinuity of the amplitude using the Cutkosky's "cutting" rule, which means that we use on-shell propagators, see Fig.2.8,

$$\begin{aligned} Disc\,\mathcal{T} = \frac{-i}{2i}\int \frac{d^4q}{(2\pi)^4} & (2\pi i)\delta(q^2 - M_c^2)\theta(-q_0) \\ & \times (2\pi i)\delta((q + P_s)^2 - M_d^2)\theta(q_0 + P_s^0)\frac{1}{(q + P_a)^2 - \mu^2}. \end{aligned} \tag{B.12}$$

We can rewrite the delta functions as

$$\begin{aligned}\delta(q^2-M_c^2) &= \frac{\delta(q_0-\sqrt{\vec{q}^{\,2}+M_c^2})}{2q_0},\\ \delta((q+P_s)^2-M_d^2) &= \frac{1}{2\sqrt{s}}\delta\left(q^0-\frac{M_d^2-M_c^2-s}{2\sqrt{s}}\right)\end{aligned} \tag{B.13}$$

and with $d^4q = dq_0\,\vec{q}^{\,2}d\vec{q}\,d\Omega$, we integrate over dq_0 and $d\vec{q}$, obtaining

$$Disc\,\mathcal{T} = \frac{1}{64\pi^2}\frac{\lambda^{1/2}(s,M_c^2,M_d^2)}{s}\int d\Omega\frac{1}{t-\mu^2}, \tag{B.14}$$

where we used that $t=(q+P_a)^2$ and

$$\begin{aligned} q^0 &= \frac{M_d^2-M_c^2-s}{2\sqrt{s}},\\ |\vec{q}| &= \frac{1}{2\sqrt{s}}\sqrt{(M_d^2-M_c^2-s)^2-4s\,M_c^2} = \frac{1}{2\sqrt{s}}\lambda^{1/2}(s,M_c^2,M_d^2).\end{aligned} \tag{B.15}$$

The term below can be expanded as

$$t-\mu^2 = M_c^2+M_a^2-\mu^2+2q^0P_a^0-2|\vec{q}|\cdot|\vec{P}_a|\cdot\cos\theta. \tag{B.16}$$

Defining $\mathcal{X}$ as

$$\mathcal{X} = \frac{M_a^2+M_c^2-\mu^2+2q^0P_a^0}{2\,|\vec{q}|\cdot|\vec{P}_a|} \tag{B.17}$$

and solving the integral $d\Omega = d\phi\,d\cos\theta$ in the Eq.(B.14), considering azimuthal symmetry in $d\phi$ we have

$$Disc\,\mathcal{T} = \frac{1}{64\pi}\frac{\lambda^{1/2}(s,M_c^2,M_d^2)}{s}\frac{1}{|\vec{q}|\cdot|\vec{P}_a|}\log\left(\frac{\mathcal{X}+1}{\mathcal{X}-1}\right). \tag{B.18}$$

The P_a components in the M_aM_b center of mass are

$$|\vec{P}_a| = \frac{1}{2\sqrt{s}}\lambda^{1/2}(s,M_a^2,M_b^2), \tag{B.19}$$

$$P_a^0 = \sqrt{M_a^2+\frac{1}{4s}\lambda(s,M_a^2,M_b^2)}. \tag{B.20}$$

Consequently, the scalar product is

$$|\vec{q}| \cdot |\vec{P}_a| = \frac{1}{4s} \lambda^{1/2}(s, M_a^2, M_b^2)\, \lambda^{1/2}(s, M_c^2, M_d^2). \tag{B.21}$$

Therefore, the final expression for the discontinuity of the amplitude $\mathcal{T}$ is

$$Disc\, \mathcal{T} = \frac{1}{16\pi} \frac{1}{\lambda^{1/2}(s, M_a^2, M_b^2)} \log\left(\frac{\mathcal{X}+1}{\mathcal{X}-1}\right). \tag{B.22}$$

In this way, we can relate the amplitude $\mathcal{T}$ with its imaginary part/discontinuity using the dispersion relation below, which comes from the Cauchy theorem for analytic functions,

$$\mathcal{T} = \int\limits_{(M_c+M_d)^2}^{\infty} \frac{ds'}{\pi} \frac{Disc\, \mathcal{T}(s')}{s'-s}. \tag{B.23}$$

Appendix C

3-Body Phase Space

In this appendix we derive the 3-body phase space used in the derivation of the cross section of a process of a collision of two initial particles creating three final ones. First, we define Mandelstam variables s, t and u,

$$s \equiv (p_2 + p_3)^2 = (q - p_1)^2 \,, \tag{C.1}$$

$$t \equiv (p_3 + p_1)^2 = (q - p_2)^2 \,, \tag{C.2}$$

$$u \equiv (p_1 + p_2)^2 = (q - p_3)^2 \,, \tag{C.3}$$

which satisfy the constraint

$$s + t + u = q^2 + p_1^2 + p_2^2 + p_3^2. \tag{C.4}$$

The three-body phase space is defined as

$$\begin{aligned} & d\Phi(p_a + p_b; p_1, p_2, p_3) \equiv d\Phi_3 \\ & = \delta^{(4)}(p_a + p_b - p_1 - p_2 - p_3) \left[\frac{d^3p_1^*}{(2\pi)^3 2E_1^*}\right] \left[\frac{d^3p_2}{(2\pi)^3 2E_2}\right] \left[\frac{d^3p_3^*}{(2\pi)^3 2E_3^*}\right] \,, \end{aligned} \tag{C.5}$$

where the quantities in squared brackets are Lorentz invariant, which means they are frame independent. For convenience, the momenta and energy with a superscript * are defined in the center of mass frame of the particles 1 and 3 (t-channel frame) and the ones without a superscript * are defined in the rest frame of the decaying particle which coincides with the center of mass frame of the initial particles. The conservation of momenta represented by the $\delta^{(4)}$ can be expressed in the t-channel frame as

$$\delta^{(4)}(p_a + p_b - p_1 - p_2 - p_3) = \delta^{(3)}(\vec{p}_0^{\,*} - \vec{p}_1^{\,*} - \vec{p}_2^{\,*} - \vec{p}_3^{\,*})\, \delta^{(0)}(E_0^* - E_1^* - E_2^* - E_3^*) \,. \tag{C.6}$$

Integrating over $d^3p_3^*$ we obtain the 3-momenta conservation $\vec{p}_3^* = \vec{p}_0^* - \vec{p}_1^* - \vec{p}_2^*$. The 3-body phase space becomes

$$d\Phi_3 = \frac{d^3p_1^* d^3p_2}{2^3(2\pi)^9 E_1^* E_2 E_3^*} \delta^{(0)}(E_0^* - E_1^* - E_2^* - E_3^*)\,. \tag{C.7}$$

Using spherical coordinates and considering that $\sqrt{t} = E_0^* - E_2^*$ we can express the phase space as

$$d\Phi_3 = \frac{(|\vec{p}_1^*|^2 d|\vec{p}_1^*| d\cos\theta_{31} d\phi_{31})(|\vec{p}_2|^2 d|\vec{p}_2| d\cos\theta_t d\phi_t)}{2^3(2\pi)^9 E_1^* E_2 E_3^*} \delta^{(0)}(\sqrt{t} - E_1^* - E_3^*)\,, \tag{C.8}$$

where $d\cos\theta_{31} = \sin\theta_{31} d\theta_{31}$ and $d\cos\theta_t = \sin\theta_t d\theta_t$. Considering azimuthal symmetry, the integral over $d\phi_t$ gives 2π and rewriting the Dirac's delta in terms of the momenta, we find

$$\begin{aligned} d\Phi_3 =& \frac{(|\vec{p}_1^*|^2 d|\vec{p}_1^*| d\cos\theta_{31} d\phi_{31})(|\vec{p}_2|^2 d|\vec{p}_2| d\cos\theta_t)}{2^3(2\pi)^8 E_1^* E_2 E_3^*} \\ & \times\delta^{(0)}\left(\sqrt{t} - \sqrt{|\vec{p}_1^*|^2 - m_1^2} - \sqrt{|\vec{p}_1^*|^2 - m_3^2}\right)\,, \end{aligned} \tag{C.9}$$

where in the t-channel frame we can consider the equality $|\vec{p}_3^*|^2 = |\vec{p}_1^*|^2$. Using the Dirac's delta relation,

$$\delta\left(g(x)\right) = \frac{\delta\left(x - x_0\right)}{|g'(x_0)|}, \tag{C.10}$$

where x_0 is obtained from the equation $g(x_0) = 0$ and $g'(x_0)$ is the derivative of $g(x)$ at position x_0, we can rewrite the delta in Eq.(C.9) as

$$\begin{aligned} &\delta^{(0)}\left(\sqrt{u} - \sqrt{|\vec{p}_1^*|^2 - m_1^2} - \sqrt{|\vec{p}_1^*|^2 - m_2^2}\right) = \\ &\frac{E_1^* E_3^*}{|\vec{p}_1^*|\sqrt{t}} \delta^{(0)}\left(|\vec{p}_1^*| - \frac{\sqrt{(t-(m_1+m_3)^2)(t-(m_1-m_3)^2)}}{2\sqrt{t}}\right)\,. \end{aligned} \tag{C.11}$$

Consequently, integrating over $d|\vec{p}_1^*|$ we obtain

$$|\vec{p}_1^*| = \frac{\sqrt{(t-(m_1+m_3)^2)(t-(m_1-m_3)^2)}}{2\sqrt{t}}. \tag{C.12}$$

The phase space now reads

$$d\Phi_3 = \frac{(|\vec{p}_1^{\,*}|d\cos\theta_{31}d\phi_{31})(|\vec{p}_2|^2 d|\vec{p}_2|d\cos\theta_t)}{2^3(2\pi)^8 E_2\sqrt{t}}, \tag{C.13}$$

thus we can express it in terms of dt by using

$$t = (p_0 - p_2)^2 = q^2 + m_2^2 - 2qE_2, \tag{C.14}$$

$$dt = -2q\frac{|\vec{p}_2|}{E_2}d|\vec{p}_2|, \tag{C.15}$$

which leads to the following expression

$$d\Phi_3 = -\frac{|\vec{p}_1^{\,*}||\vec{p}_2|dt\,d\cos\theta_{31}\,d\phi_{31}\,d\cos\theta_t}{2^4(2\pi)^8 q\sqrt{t}}. \tag{C.16}$$

Analogously, we can write the phase space in terms of ds by using

$$s = (p_0^* - p_1^*)^2 = q^2 + m_1^2 - 2E_0^*E_1^* + 2|\vec{p}_0^{\,*}||\vec{p}_1^{\,*}|\underbrace{\cos(\pi - \theta_{31})}_{-\cos(\theta_{31})}, \tag{C.17}$$

$$ds = -2|\vec{p}_0^{\,*}||\vec{p}_1^{\,*}|d\cos(\theta_{31}). \tag{C.18}$$

In this case we find

$$d\Phi_3 = \frac{|\vec{p}_2|}{|\vec{p}_0^{\,*}|}\frac{ds\,dt\,d\phi_{31}\,d\cos\theta_t}{2^5(2\pi)^8 q\sqrt{t}}. \tag{C.19}$$

With the modulus of the momenta given by

$$|\vec{p}_0^{\,*}| = \frac{\lambda^{1/2}(t, q^2, m_2^2)}{2\sqrt{t}}, \tag{C.20}$$

$$|\vec{p}_3| = \frac{\lambda^{1/2}(q^2, m_2^2, t)}{2q}, \tag{C.21}$$

the phase space becomes

$$d\Phi_3 = \frac{ds\,dt\,d\cos\theta_t\,d\phi_{31}}{2^4(2\pi)^8 q^2}. \tag{C.22}$$

Analogously, the 3-body phase space can be also expressed in terms of the angles in the s- and u-channel as

$$d\Phi_3 = \frac{ds\, dt\, d\cos\theta_s\, d\phi_{23}}{2^4(2\pi)^8 q^2} = \frac{ds\, du\, d\cos\theta_u\, d\phi_{12}}{2^4(2\pi)^8 q^2}. \tag{C.23}$$

Appendix D

Polar Angles

In this section we derive the expression for the polar angles used in the helicity amplitude Eq.(2.113), which are defined in the range $[0, \pi]$. The cosine of these angles can be written in terms of the Mandelstam variables and masses, which we obtain from the scalar product of the momenta of the external particles. The Mandelstam variables are defined as

$$\begin{aligned} s \equiv M_{\pi\pi}^2 &= (p_{\pi^+} + p_{\pi^-})^2 = (p_{\gamma^*} - p_\psi)^2, \\ t \equiv M_{\psi\pi^+}^2 &= (p_\psi + p_{\pi^+})^2 = (p_{\gamma^*} - p_{\pi^-})^2, \\ u \equiv M_{\psi\pi^-}^2 &= (p_\psi + p_{\pi^-})^2 = (p_{\gamma^*} - p_{\pi^+})^2, \end{aligned} \tag{D.1}$$

where we rel-labelled the momenta in a more descriptive way according to our process

$$p_1 = p_\psi, \quad p_2 = p_{\pi^-}, \quad p_3 = p_{\pi^+}. \tag{D.2}$$

The angles θ_{31} and θ_{12} are the angles of the momenta of ψ and $\pi^\pm$ in the rest frame of the intermediate state in the t-channel (Z_c^+) and u-channel (Z_c^-), respectively, as shown in Fig.D.1. The angle θ_{31} can be determine from the scalar product of the momenta of π^- and ψ,

$$\cos(\theta_{31}) = -\frac{M_{\psi\pi^-}^2 - m_\psi^2 - m_{\pi^-}^2 - 2E_\psi E_{\pi^-}}{2|\vec{p}_\psi||\vec{p}_{\pi^-}|}, \tag{D.3}$$

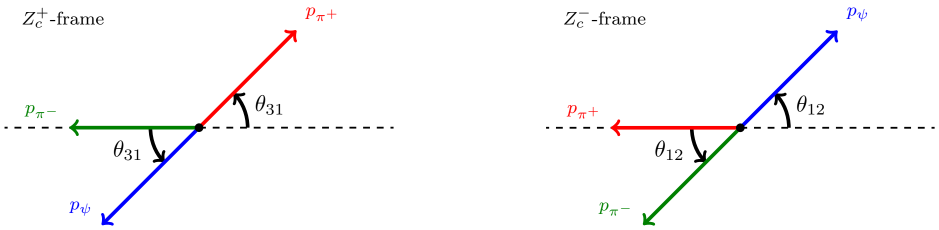

(A) (B)

FIGURE D.1: Momenta in the rest frame of Z_c^+ (A) and Z_c^- (B), where the blue, green and red arrows represent the three-momenta of ψ, π^+ and π^-, respectively. The angle θ_{31} is the angle between π^- and ψ in the Z_c^+ rest frame, while θ_{12} is the angle between π^+ and π^- in the Z_c^- rest frame.

where the energies and the momenta in the Z_c^+ rest frame are given by

$$\begin{aligned}
E_\psi^{Z_c^+} &= \frac{M^2_{\psi\pi^+} + m^2_\psi - m^2_{\pi^+}}{2M_{\psi\pi^+}}, \quad |\vec{p}_\psi^{\,Z_c^+}| = \frac{1}{2M_{\psi\pi^+}}\lambda^{1/2}(M^2_{\psi\pi^+}, m^2_\psi, m^2_{\pi^+}),\\
E_{\pi^-}^{Z_c^+} &= -\frac{M^2_{\psi\pi^+} + m^2_{\pi^-} - q^2}{2M_{\psi\pi^+}}, \quad |\vec{p}_{\pi^-}^{\,Z_c^+}| = \frac{1}{2M_{\psi\pi^+}}\lambda^{1/2}(M^2_{\psi\pi^+}, m^2_{\pi^-}, q^2).
\end{aligned} \tag{D.4}$$

Analogously, the angle θ_{12} can be obtained by calculating the scalar product of the momenta of π^- and π^+,

$$\cos(\theta_{12}) = -\frac{M^2_{\pi^+\pi^-} - m^2_{\pi^+} - m^2_{\pi^-} - 2E_{\pi^+}E_{\pi^-}}{2|\vec{p}_{\pi^+}||\vec{p}_{\pi^-}|}, \tag{D.5}$$

where the energies and the momenta in the Z_c^- rest frame are given by

$$\begin{aligned}
E_{\pi^-}^{Z_c^-} &= \frac{M^2_{\psi\pi^-} + m^2_{\pi^-} - m^2_\psi}{2M_{\psi\pi^-}}, \quad |\vec{p}_{\pi^-}^{\,Z_c^-}| = \frac{1}{2M_{\psi\pi^-}}\lambda^{1/2}(M^2_{\psi\pi^-}, m^2_{\pi^-}, m^2_\psi),\\
E_{\pi^+}^{Z_c^-} &= -\frac{M^2_{\psi\pi^-} + m^2_{\pi^+} - q^2}{2M_{\psi\pi^-}}, \quad |\vec{p}_{\pi^+}^{\,Z_c^-}| = \frac{1}{2M_{\psi\pi^-}}\lambda^{1/2}(M^2_{\psi\pi^-}, m^2_{\pi^+}, q^2).
\end{aligned} \tag{D.6}$$

The angles $\bar{\theta}_{ts}$ and $\bar{\theta}_{us}$ rotate the configurations of the t-channel and u-channel, back to the s-channel configuration, as discussed in Eq.(2.107) and Eq.(2.110) and shown in Fig.D.2. We obtain the rotations by using the scalar products in the γ^* rest frame

$$\cos\left(\bar{\theta}_{st}\right) = -\frac{M^2_{\psi\pi^-} - m^2_\psi - m^2_{\pi^-} - 2E_\psi E_{\pi^-}}{2|\vec{p}_\psi||\vec{p}_{\pi^-}|}, \tag{D.7}$$

$$\cos\left(\bar{\theta}_{us}\right) = -\frac{M^2_{\psi\pi^+} - m^2_\psi - m^2_{\pi^+} - 2E_\psi E_{\pi^+}}{2|\vec{p}_\psi||\vec{p}_{\pi^+}|}, \tag{D.8}$$

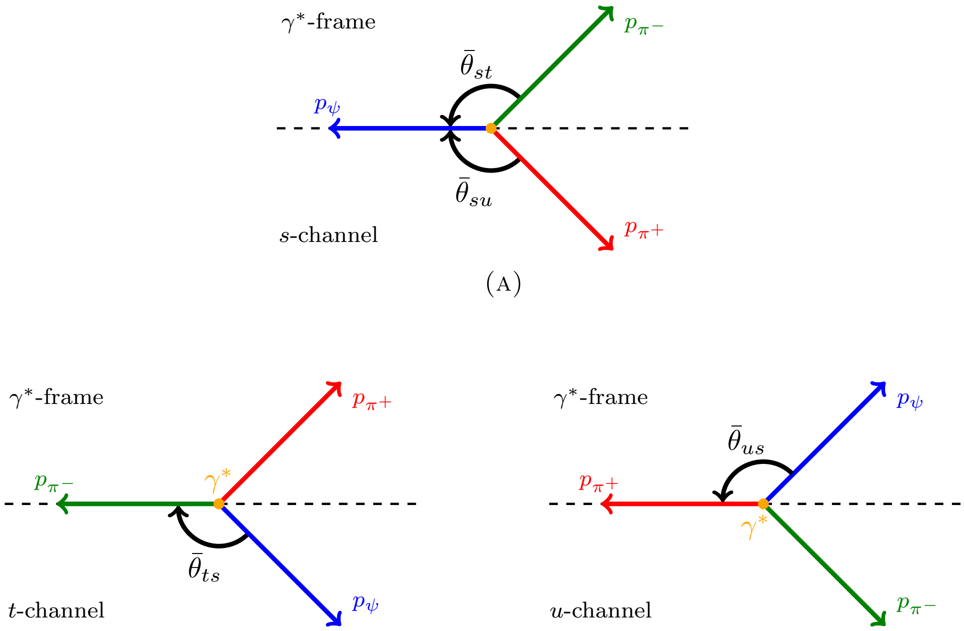

(A)

(B)

(C)

FIGURE D.2: Configurations of momenta in the s- (A), t- (B) and u- (C) channel in the rest frame of γ^*, where the blue, green and red arrows represent the three-momenta of ψ, π^+ and π^-, respectively. The rotations $\bar\theta_{ts}$ and $\bar\theta_{us}$ bring the configuration of the t- and u-channel to the s-channel, respectively.

where the energies and the momenta in the γ^* rest frame are given by

$$\begin{aligned}
E_\psi^{\gamma^*} &= \frac{q^2+m_\psi^2-M_{\pi\pi}^2}{2q}, \quad |\vec p_\psi^{\,\gamma^*}| = \frac{1}{2q}\lambda^{1/2}(q^2,m_\psi^2,M_{\pi\pi}^2),\\
E_{\pi^-}^{\gamma^*} &= \frac{q^2+m_{\pi^-}^2-M_{\psi\pi^+}^2}{2q}, \quad |\vec p_{\pi^-}^{\,\gamma^*}| = \frac{1}{2q}\lambda^{1/2}(q^2,m_{\pi^-}^2,M_{\psi\pi^+}^2),\\
E_{\pi^+}^{\gamma^*} &= \frac{q^2+m_{\pi^+}^2-M_{\psi\pi^-}^2}{2q}, \quad |\vec p_{\pi^+}^{\,\gamma^*}| = \frac{1}{2q}\lambda^{1/2}(q^2,m_{\pi^+}^2,M_{\psi\pi^-}^2).
\end{aligned} \tag{D.9}$$

Notice that we define anti-clockwise rotations as positive, consequently clockwise rotations are negative. Therefore the rotation from the t-channel to the s-channel is expressed as $\bar\theta_{ts} = -\bar\theta_{st}$. We can use then the following relation for the Wigner d-functions

$$d^j_{\lambda'\lambda}(\bar\theta_{ts}) = (-1)^{\lambda'-\lambda} d^j_{\lambda'\lambda}(\bar\theta_{st}) = d^j_{\lambda\lambda'}(\bar\theta_{st}). \tag{D.10}$$

The Wigner rotations $\omega_\psi^{(t)}$ and $\omega_\psi^{(u)}$ can be determined by boosting the system to the rest frame of ψ and observing how much the t- and u-channel configurations are rotated

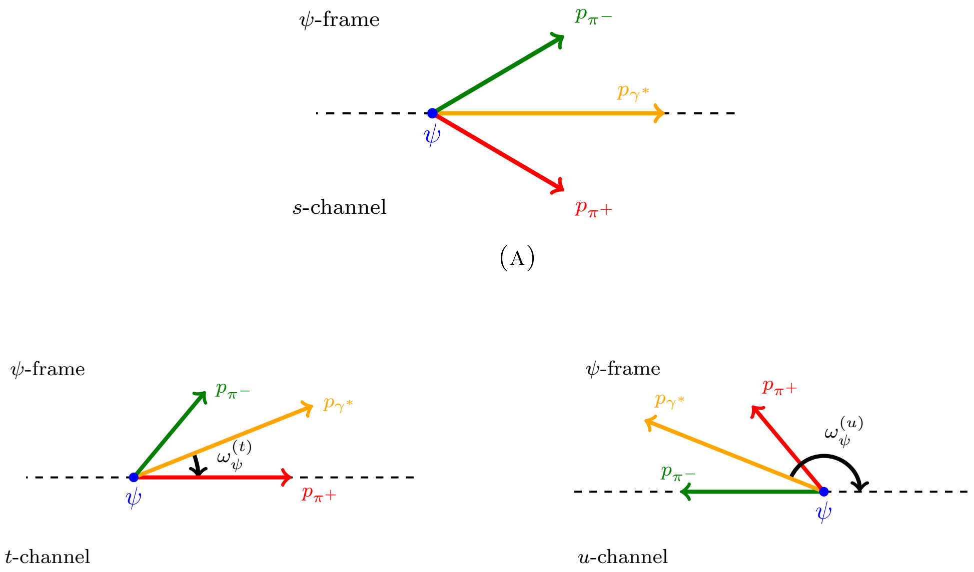

(A)

(B)

(C)

FIGURE D.3: The three-momenta of the particles are boosted to the rest frame of ψ for the configurations in the s- (A), t- (B) and u-channel (C), where the blue, green and red arrows represent the three-momenta of ψ, π^+ and π^-, respectively. The spin projections of ψ are different in each channel and we can express them consistently in the s-channel by using the Wigner rotations $\omega_\psi^{(t)}$ and $\omega_\psi^{(u)}$.

from the s-channel configuration, as shown in the Fig.D.3. As before, we can determine the Wigner rotations by using scalar products,

$$\cos(\alpha_{\gamma^*\pi^+}) = \frac{M_{\psi\pi^-}^2 - q^2 - m_{\pi^+}^2 + 2E_{\gamma^*}E_{\pi^+}}{2|\vec{p}_{\gamma^*}||\vec{p}_{\pi^+}|}, \tag{D.11}$$

$$\cos(\alpha_{\gamma^*\pi^-}) = \frac{M_{\psi\pi^+}^2 - q^2 - m_{\pi^-}^2 + 2E_{\gamma^*}E_{\pi^-}}{2|\vec{p}_{\gamma^*}||\vec{p}_{\pi^-}|}, \tag{D.12}$$

where $\alpha_{\psi\pi^-}$ and $\alpha_{\psi\pi^+}$ are the angles between ψ and π^- and ψ and π^+, respectively. The energies and the momenta in the ψ rest frame are given by

$$\begin{aligned}
E_{\gamma^*}^{\psi} &= \frac{m_\psi^2 + q^2 - M_{\pi\pi}^2}{2m_\psi}, \quad |\vec{p}_{\gamma^*}^{\,\psi}| = \frac{1}{2m_\psi}\lambda^{1/2}(m_\psi^2, q^2, M_{\pi\pi}^2), \\
E_{\pi^-}^{\psi} &= -\frac{m_\psi^2 + m_{\pi^-}^2 - M_{\psi\pi^-}^2}{2m_\psi}, \quad |\vec{p}_{\pi^-}^{\,\psi}| = \frac{1}{2m_\psi}\lambda^{1/2}(m_\psi^2, m_{\pi^-}^2, M_{\psi\pi^-}^2), \\
E_{\pi^+}^{\psi} &= -\frac{m_\psi^2 + m_{\pi^+}^2 - M_{\psi\pi^+}^2}{2m_\psi}, \quad |\vec{p}_{\pi^+}^{\,\psi}| = \frac{1}{2m_\psi}\lambda^{1/2}(m_\psi^2, m_{\pi^+}^2, M_{\psi\pi^+}^2).
\end{aligned} \tag{D.13}$$

Consequently, as shown in Fig.D.3, the Wigner rotations are expressed as following

$$\begin{aligned} \omega_{\psi}^{(t)} &= -\alpha_{\gamma^*\pi^+}, \\ \omega_{\psi}^{(u)} &= -(\pi - \alpha_{\gamma^*\pi^-}). \end{aligned} \tag{D.14}$$

Notice that we can use the following relation for the Wigner d-functions

$$d^j_{\lambda'\lambda}(\pi - \alpha) = (-1)^{j-\lambda'} d^j_{\lambda'(-\lambda)}(\alpha). \tag{D.15}$$

Bibliography

[1] D. A. S. Molnar, I. Danilkin, and M. Vanderhaeghen, "The role of charged exotic states in $e^+e^- \to \psi(2S)\, \pi^+\pi^-$", Phys. Lett. B **797**, 134851 (2019).

[2] I. Danilkin, D. A. S. Molnar, and M. Vanderhaeghen, "Simultaneous description of the $e^+e^- \to J/\psi\pi\pi(K\bar{K})$ processes", Phys. Rev. D **102**, 016019 (2020).

[3] I. Danilkin, D. A. S. Molnar, and M. Vanderhaeghen, "Dispersive Analysis of $e^+e^- \to h_c\, \pi^+\pi^-$", In Preparation.

[4] H. Yukawa, Proc. Phys. Math. Soc. Japan **17**, 1935 (1935).

[5] C. M. G. Lattes, G. Occhialini, and C. Powell, Nature **160**, 486 (1947).

[6] E. Gardner and C. M. G. Lattes, Science **107**, 270 (1948).

[7] M. Gell-Mann, Phys. Rev. Lett. **8**, 214 (1964).

[8] G. Zweig, CERN Preprint **8182/TH401**, 24 (1964).

[9] R. P. Feynman, Phys. Rev.Lett. **23**, 1415 (1969).

[10] K. Olive *et al.* (Particle Data Group), Chin. Phys. C **38**, 090001 (2014).

[11] G. 't Hooft and M. J. G. Veltman, "Regularization and Renormalization of Gauge Fields", Nucl. Phys. B **44**, 189–213 (1972).

[12] D. J. Gross and F. Wilczek, "Ultraviolet behavior of non-abelian gauge theories", Phys. Rev. Lett. **30**, 1343–1346 (1973).

[13] H. D. Politzer, "Reliable perturbative results for strong interactions?", Phys. Rev. Lett. **30**, 1346–1349 (1973).

[14] R. Ellis, W. Stirling, and B. Webber, *Qcd and collider physics* (Cambridge University Press, Cambridge, UK, 1996).

[15] B. Ioffe, V. Fadin, and L. Lipatov, *Qcd perturbative and nonpertubative aspects* (Cambridge University Press, Cambridge, UK, 2010).

[16] G. Dissertori, I. Knowles, and M. Schmelling, *Quantum chromodynamics* (Oxford University Press, New York, USA, 2010).

[17] J. Collins, *Foundations of perturbative qcd* (Cambridge University Press, Cambridge, UK, 2011).

[18] A. Hosaka and H. Toki, *Quarks, baryons and chiral symmetry* (World Scientific, Singapore, 2001).

[19] D. Griffiths, *Introduction to elementary particles* (Wiley, New York, USA, 1987).

[20] M. Luscher, “Lattice QCD: From quark confinement to asymptotic freedom”, Annales Henri Poincare **4**, edited by V. Rivasseau, S197–S210 (2003), arXiv:`hep-ph/0211220`.

[21] C. Davies and P. Lepage, “Lattice QCD meets experiment in hadron physics”, AIP Conf. Proc. **717**, edited by H. Orth, H. Koch, and E. Klempt, 615–624 (2004), arXiv:`hep-ph/0311041`.

[22] R. Frezzotti, M. Garofalo, V. Lubicz, G. Martinelli, C. T. Sachrajda, F. Sanfilippo, S. Simula, and N. Tantalo, “Comparison of lattice QCD+QED predictions for radiative leptonic decays of light mesons with experimental data”, Phys. Rev. D **103**, 053005 (2021).

[23] D. G. Ireland, *Notes on Hadron Physics*, 19th UK Nuclear Physics Summer School, 2017.

[24] G. Cowan and T. Gershon, “Tetraquarks and pentaquarks”, arXiv:1808.04153 [physics.pop-ph] (2018).

[25] J. J. Aubert et al. (E598), “Experimental Observation of a Heavy Particle J”, Phys. Rev. Lett. **33**, 1404–1406 (1974).

[26] J. E. Augustin et al. (SLAC-SP-017), “Discovery of a Narrow Resonance in e^+e^- Annihilation”, Phys. Rev. Lett. **33**, 1406–1408 (1974).

[27] T. Appelquist and H. D. Politzer, “Orthocharmonium and e+ e- Annihilation”, Phys. Rev. Lett. **34**, 43 (1975).

[28] J. D. Bjorken and S. L. Glashow, “Elementary Particles and SU(4)”, Phys. Lett. **11**, 255–257 (1964).

[29] S. W. Herb et al., “Observation of a Dimuon Resonance at 9.5-GeV in 400-GeV Proton-Nucleus Collisions”, Phys. Rev. Lett. **39**, 252–255 (1977).

[30] N. Brambilla, S. Eidelman, C. Hanhart, A. Nefediev, C.-P. Shen, C. E. Thomas, A. Vairo, and C.-Z. Yuan, “The XYZ states: experimental and theoretical status and perspectives”, Phys. Rept. **873**, 1–154 (2020), arXiv:`1907.07583 [hep-ex]`.

[31] D. Acosta *et al.* (CDF Collaboration), Phys. Rev. Lett. **93**, 072001 (2004).

[32] V. M. Abazov *et al.* (D0 Collaboration), Phys. Rev. Lett. **93**, 162002 (2004).

[33] S. K. Choi et al. (Belle), "Observation of a resonance-like structure in the $\pi^{+-}\psi'$ mass distribution in exclusive $B \to K\pi^{+-}\psi'$ decays", Phys. Rev. Lett. **100**, 142001 (2008).

[34] R. Aaij et al. (LHCb), "Observation of the resonant character of the $Z(4430)^-$ state", Phys. Rev. Lett. **112**, 222002 (2014).

[35] K. Chilikin et al. (Belle), "Experimental constraints on the spin and parity of the $Z(4430)^+$", Phys. Rev. **D88**, 074026 (2013).

[36] M. Ablikim et al. (BESIII), "Observation of a Charged Charmoniumlike Structure in $e^+e^- \to \pi^+\pi^- J/\psi$ at $\sqrt{s} = 4.26$ GeV", Phys. Rev. Lett. **110**, 252001 (2013), `arXiv:1303.5949 [hep-ex]`.

[37] M. Tanabashi et al. (Particle Data Group), "Review of Particle Physics", Phys. Rev. **D98**, 030001 (2018).

[38] C.-Z. Yuan, "The XYZ states revisited", Int. J. Mod. Phys. **A33**, 1830018 (2018).

[39] S. L. Olsen, T. Skwarnicki, and D. Zieminska, "Nonstandard heavy mesons and baryons: Experimental evidence", Rev. Mod. Phys. **90**, 015003 (2018).

[40] R. F. Lebed, R. E. Mitchell, and E. S. Swanson, "Heavy-Quark QCD Exotica", Prog. Part. Nucl. Phys. **93**, 143–194 (2017).

[41] F.-K. Guo, C. Hanhart, U.-G. Meißner, Q. Wang, Q. Zhao, and B.-S. Zou, "Hadronic molecules", Rev. Mod. Phys. **90**, 015004 (2018).

[42] H.-X. Chen, W. Chen, X. Liu, and S.-L. Zhu, "The hidden-charm pentaquark and tetraquark states", Phys. Rept. **639**, 1–121 (2016).

[43] M. R. Shepherd, J. J. Dudek, and R. E. Mitchell, "Searching for the rules that govern hadron construction", Nature **534**, 487–493 (2016).

[44] Y.-R. Liu, H.-X. Chen, W. Chen, X. Liu, and S.-L. Zhu, "Pentaquark and tetraquark states", Progress in Particle and Nuclear Physics **107**, 237–320 (2019).

[45] E. S. Swanson, "Z_b and Z_c Exotic States as Coupled Channel Cusps", Phys. Rev. **D91**, 034009 (2015).

[46] A. P. Szczepaniak, "Triangle Singularities and XYZ Quarkonium Peaks", Phys. Lett. **B747**, 410–416 (2015).

[47] A. Pilloni et al. (JPAC), "Amplitude analysis and the nature of the $Z_c(3900)$", Phys. Lett. **B772**, 200–209 (2017).

[48] F.-K. Guo, C. Hanhart, Q. Wang, and Q. Zhao, "Could the near-threshold XYZ states be simply kinematic effects?", Phys. Rev. **D91**, 051504 (2015).

[49] S. X. Nakamura and K. Tsushima, "$Z_c(4430)$ and $Z_c(4200)$ as triangle singularities", (2019), `arXiv:1901.07385 [hep-ph]`.

[50] S. X. Nakamura, "Triangle singularities in $\bar{B}^0 \to \chi_{c1} K^- \pi^+$ relevant to $Z_1(4050)$ and $Z_2(4250)$", Phys. Rev. **D100**, 011504 (2019), `arXiv:1903.08098 [hep-ph]`.

[51] M. Ablikim et al. (BESIII), "Determination of the Spin and Parity of the $Z_c(3900)$", Phys. Rev. Lett. **119**, 072001 (2017).

[52] J. A. Wheeler, "On the mathematical description of light nuclei by the method of resonating group structure", Phys. Rev. **52**, 1107–1122 (1937).

[53] W. Heisenberg, "Die "beobachtbaren größen" in der theorie der elementarteilchen", Zeitschrift für Physik **120**, 513–538 (1943).

[54] D. A. S. Molnar, "Teoria Efetiva para Decaimentos Radiativos do X(3872)", Master thesis (Universidade de Sao Paulo, 2015).

[55] H. M. Nussenzveig, *Causality and dispersion relations* (Academic Press, New York, USA, 1972).

[56] O. Gryniuk, "Dispersion Relations in two-photon hadronic processes", PhD thesis (Universitat Mainz, 2020).

[57] A. R. Bilbao, "Dispersive study of light mesons", PhD thesis (Universidad Complutense de Madrid, 2019).

[58] J. R. de Elvira Carrascal, "Study of the properties and nature of the lightest scalar mesons", PhD thesis (Universidad Complutense de Madrid, 2013).

[59] F. Niecknig, "Dispersive analysis of charmed meson decays", PhD thesis (Universitat Bonn, 2016).

[60] S. Lanz, "Determination of the quark mass ratio Q from $\eta \to 3\pi$", PhD thesis (Universitat Bern, 2011).

[61] A. W. Jackura, "Studies in multiparticles scattering theory", PhD thesis (Indiana University, 2019).

[62] O. Deineika, "Dispersive analysis of $\gamma\gamma \to \pi\eta$", MA thesis (Universitat Mainz, 2017).

[63] I. Danilkin, “Coupled-channel dynamics in mesonic systems”, PhD thesis (Technische Universitat Darmstadt, 2019).

[64] I. Danilkin, *Notes on Dispersion Relations*, Summer School Indiana University, 2015.

[65] R. J. Eden, P. V. Landshoff, D. I. Olive, and J. C. Polkinghorne, *The Analytic S-Matrix* (Cambrige University Press, 1966).

[66] V. Barone and E. Predazzi, *High-Energy particle Diffraction* (Springer, 2002).

[67] S. Gasiorowicz, *Elementary particle physics* (John Wiley & Sons, 1966).

[68] R. Dalitz, “On the analysis of tau-meson data and the nature of the tau-meson”, Phil. Mag. Ser. 7 **44**, 1068–1080 (1953).

[69] R. Dalitz, “Decay of tau mesons of known charge”, Phys. Rev. **94**, 1046–1051 (1954).

[70] Muskhelishvili, Trud. Tbil. Mat. Inst. **10**, 1 (1941).

[71] R. Omnes, “On the Solution of certain singular integral equations of quantum field theory”, Nuovo Cim. **8**, 316 (1958).

[72] F. Yndurain, “Low-energy pion physics”, (2002), arXiv:`hep-ph/0212282`.

[73] K. M. Watson, “Some general relations between the photoproduction and scattering of pi mesons”, Phys. Rev. **95**, 228–236 (1954).

[74] G. Kallen, “On the definition of the Renormalization Constants in Quantum Electrodynamics”, Helv. Phys. Acta **25**, edited by C. Jarlskog, 417 (1952).

[75] H. Lehmann, “On the Properties of propagation functions and renormalization contants of quantized fields”, Nuovo Cim. **11**, 342–357 (1954).

[76] B. Moussallam, “Unified dispersive approach to real and virtual photon-photon scattering at low energy”, Eur. Phys. J. **C73**, 2539 (2013).

[77] L. D. Landau, “On analytic properties of vertex parts in quantum field theory”, Nucl. Phys. **13**, 181–192 (1959).

[78] K. Way and E. Wigner, “The Rate of Decay of Fission Products”, Phys. Rev. **73**, 1318–1330 (1948).

[79] F.-K. Guo, X.-H. Liu, and S. Sakai, “Threshold cusps and triangle singularities in hadronic reactions”, Prog. Part. Nucl. Phys. **112**, 103757 (2020).

[80] S. Coleman and R. E. Norton, “Singularities in the physical region”, Nuovo Cim. **38**, 438–442 (1965).

[81] R. E. Cutkosky, “Singularities and discontinuities of Feynman amplitudes”, J. Math. Phys. **1**, 429–433 (1960).

[82] H. Chen and R.-G. Ping, “Coherent helicity amplitude for sequential decays”, Phys. Rev. D **95**, 076010 (2017), arXiv:`1704.05184 [hep-ph]`.

[83] M. Mikhasenko et al. (JPAC), “Dalitz-plot decomposition for three-body decays”, Phys. Rev. D **101**, 034033 (2020), arXiv:`1910.04566 [hep-ph]`.

[84] M. Jacob and G. C. Wick, “On the General Theory of Collisions for Particles with Spin”, Annals Phys. **7**, 404–428 (1959).

[85] J. Gasser and H. Leutwyler, “Chiral Perturbation Theory to One Loop”, Annals Phys. **158**, 142 (1984).

[86] D. R. Bolton, R. A. Briceno, and D. J. Wilson, “Connecting physical resonant amplitudes and lattice QCD”, Phys. Lett. **B757**, 50–56 (2016).

[87] A. Gomez Nicola and J. R. Pelaez, “Meson meson scattering within one loop chiral perturbation theory and its unitarization”, Phys. Rev. **D65**, 054009 (2002).

[88] J. Gasser and H. Leutwyler, “Low-Energy Theorems as Precision Tests of QCD”, Phys. Lett. **125B**, 325–329 (1983).

[89] J. Gasser and H. Leutwyler, “Chiral Perturbation Theory: Expansions in the Mass of the Strange Quark”, Nucl. Phys. **B250**, 465–516 (1985).

[90] C. Hanhart, J. R. Pelaez, and G. Rios, “Quark mass dependence of the rho and sigma from dispersion relations and Chiral Perturbation Theory”, Phys. Rev. Lett. **100**, 152001 (2008).

[91] R. Garcia-Martin, R. Kaminski, J. R. Pelaez, J. Ruiz de Elvira, and F. J. Yndurain, “The Pion-pion scattering amplitude. IV: Improved analysis with once subtracted Roy-like equations up to 1100 MeV”, Phys. Rev. **D83**, 074004 (2011).

[92] A. Gomez Nicola, J. R. Pelaez, and G. Rios, “The Inverse Amplitude Method and Adler Zeros”, Phys. Rev. **D77**, 056006 (2008).

[93] G. Colangelo, M. Hoferichter, M. Procura, and P. Stoffer, “Rescattering effects in the hadronic-light-by-light contribution to the anomalous magnetic moment of the muon”, Phys. Rev. Lett. **118**, 232001 (2017).

[94] G. Colangelo, M. Hoferichter, M. Procura, and P. Stoffer, "Dispersion relation for hadronic light-by-light scattering: two-pion contributions", JHEP **04**, 161 (2017), `arXiv:1702.07347 [hep-ph]`.

[95] J. A. Oller, L. Roca, and C. Schat, "Improved dispersion relations for $\gamma\gamma \to \pi^0\pi^0$", Phys. Lett. **B659**, 201–208 (2008).

[96] I. Danilkin, O. Deineka, and M. Vanderhaeghen, "Data-driven dispersive analysis of the $\pi\pi$ and πK scattering", Phys. Rev. D **103**, 114023 (2021), `arXiv:2012.11636 [hep-ph]`.

[97] A. Gasparyan and M. F. M. Lutz, "Photon- and pion-nucleon interactions in a unitary and causal effective field theory based on the chiral Lagrangian", Nucl. Phys. **A848**, 126–182 (2010).

[98] I. V. Danilkin, A. M. Gasparyan, and M. F. M. Lutz, "On causality, unitarity and perturbative expansions", Phys. Lett. **B697**, 147–152 (2011).

[99] G. F. Chew and S. Mandelstam, "Theory of low-energy pion pion interactions", Phys. Rev. **119**, 467–477 (1960).

[100] I. V. Danilkin, L. I. R. Gil, and M. F. M. Lutz, "Dynamical light vector mesons in low-energy scattering of Goldstone bosons", Phys. Lett. **B703**, 504–509 (2011).

[101] P. Buettiker, S. Descotes-Genon, and B. Moussallam, "A new analysis of pi K scattering from Roy and Steiner type equations", Eur. Phys. J. **C33**, 409–432 (2004).

[102] J. R. Pelaez and A. Rodas, "$\pi\pi \to K\bar{K}$ scattering up to 1.47 GeV with hyperbolic dispersion relations", Eur. Phys. J. **C78**, 897 (2018).

[103] I. Danilkin and M. Vanderhaeghen, "Dispersive analysis of the $\gamma\gamma^* \to \pi\pi$ process", Phys. Lett. **B789**, 366–372 (2019).

[104] I. Danilkin, C. F. Redmer, and M. Vanderhaeghen, "The hadronic light-by-light contribution to the muons anomalous magnetic moment", Prog. Part. Nucl. Phys. **107**, 20–68 (2019).

[105] I. Danilkin, O. Deineka, and M. Vanderhaeghen, "Dispersive analysis of the $\gamma^*\gamma^* \to \pi\pi$ process", Phys. Rev. D **101**, 054008 (2020).

[106] X. L. Wang et al. (Belle), "Measurement of $e^+e^- \to \pi^+\pi^-\psi(2S)$ via Initial State Radiation at Belle", Phys. Rev. **D91**, 112007 (2015).

[107] X. L. Wang et al. (Belle), "Observation of Two Resonant Structures in e+e- to pi+ pi- psi(2S) via Initial State Radiation at Belle", Phys. Rev. Lett. **99**, 142002 (2007).

[108] M. Ablikim et al. (BESIII), "Measurement of $e^+e^- \to \pi^+\pi^-\psi(3686)$ from 4.008 to 4.600 GeV and observation of a charged structure in the $\pi^\pm\psi(3686)$ mass spectrum", Phys. Rev. **D96**, 032004 (2017).

[109] Y.-H. Chen, J. T. Daub, F.-K. Guo, B. Kubis, U.-G. Meißner, and B.-S. Zou, "Effect of Z_b states on $\Upsilon(3S) \to \Upsilon(1S)\pi\pi$ decays", Phys. Rev. **D93**, 034030 (2016).

[110] Y.-H. Chen, M. Cleven, J. T. Daub, F.-K. Guo, C. Hanhart, B. Kubis, U.-G. Meißner, and B.-S. Zou, "Effects of Z_b states and bottom meson loops on $\Upsilon(4S) \to \Upsilon(1S, 2S)\pi^+\pi^-$ transitions", Phys. Rev. **D95**, 034022 (2017).

[111] T. Isken, B. Kubis, S. P. Schneider, and P. Stoffer, "Dispersion relations for $\eta' \to \eta\pi\pi$", Eur. Phys. J. **C77**, 489 (2017).

[112] Y.-H. Chen, L.-Y. Dai, F.-K. Guo, and B. Kubis, "Nature of the $Y(4260)$: A light-quark perspective", Phys. Rev. **D99**, 074016 (2019), `arXiv:1902.10957 [hep-ph]`.

[113] M. Ablikim et al. (BESIII), "Measurement of $e^+e^- \to \pi^0\pi^0\psi(3686)$ at $\sqrt{s}$ from 4.009 to 4.600 GeV and observation of a neutral charmoniumlike structure", Phys. Rev. **D97**, 052001 (2018).

[114] R. Tarrach, "Invariant Amplitudes for Virtual Compton Scattering Off Polarized Nucleons Free from Kinematical Singularities, Zeros and Constraints", Nuovo Cim. **A28**, 409 (1975).

[115] D. Drechsel, G. Knochlein, A. Y. Korchin, A. Metz, and S. Scherer, "Structure analysis of the virtual Compton scattering amplitude at low-energies", Phys. Rev. **C57**, 941–952 (1998).

[116] G. Colangelo, M. Hoferichter, M. Procura, and P. Stoffer, "Dispersion relation for hadronic light-by-light scattering: theoretical foundations", JHEP **09**, 074 (2015).

[117] I. Danilkin, O. Deineka, and M. Vanderhaeghen, "Theoretical analysis of the $\gamma\gamma \to \pi^0\eta$ process", Phys. Rev. **D96**, 114018 (2017).

[118] M. Hoferichter and P. Stoffer, "Dispersion relations for $\gamma^*\gamma^* \to \pi\pi$: helicity amplitudes, subtractions, and anomalous thresholds", JHEP **07**, 073 (2019).

[119] P. Lichard and J. Juran, “Four-charged-pion decay of $\rho_0(770)$ and the $a(1) - \rho\pi$ Lagrangian”, Phys. Rev. D **76**, 094030 (2007), arXiv:`hep-ph/0601234`.

[120] L. Roca, J. E. Palomar, and E. Oset, “Decay of axial vector mesons into VP and P gamma”, Phys. Rev. **D70**, 094006 (2004).

[121] R. Karplus, C. M. Sommerfield, and E. H. Wichmann, “Spectral Representations in Perturbation Theory. 1. Vertex Function”, Phys. Rev. **111**, 1187–1190 (1958).

[122] S. Mandelstam, “Unitarity Condition Below Physical Thresholds in the Normal and Anomalous Cases”, Phys. Rev. Lett. **4**, 84–87 (1960).

[123] M. Hoferichter, G. Colangelo, M. Procura, and P. Stoffer, “Virtual photon-photon scattering”, Int. J. Mod. Phys. Conf. Ser. **35**, 1460400 (2014).

[124] M. F. M. Lutz, E. E. Kolomeitsev, and C. L. Korpa, “Spectral representation for u- and t-channel exchange processes in a partial-wave decomposition”, Phys. Rev. **D92**, 016003 (2015).

[125] J. B. Bronzan and C. Kacser, “Khuri-Treiman Representation and Perturbation Theory”, Phys. Rev. **132**, 2703 (1963).

[126] M. Ablikim et al. (BESIII), “Observation of $e^+e^- \to \pi^0\pi^0 h_c$ and a Neutral Charmoniumlike Structure $Z_c(4020)^0$”, Phys. Rev. Lett. **113**, 212002 (2014).

[127] M. Ablikim et al. (BESIII), “Observation of a neutral charmoniumlike state $Z_c(4025)^0$ in $e^+e^- \to (D^*\bar{D}^*)^0\pi^0$”, Phys. Rev. Lett. **115**, 182002 (2015).

[128] M. Ablikim et al. (BESIII), “Observation of a Charged Charmoniumlike Structure $Z_c(4020)$ and Search for the $Z_c(3900)$ in $e^+e^- \to \pi^+\pi^- h_c$”, Phys. Rev. Lett. **111**, 242001 (2013).

[129] M. Ablikim et al. (BESIII), “Observation of a charged charmoniumlike structure in $e^+e^- \to (D^*\bar{D}^*)^\pm\pi^\mp$ at $\sqrt{s} = 4.26$GeV”, Phys. Rev. Lett. **112**, 132001 (2014).

[130] S. H. Lee, M. Nielsen, and U. Wiedner, “D(s)D* molecule as an axial meson”, J. Korean Phys. Soc. **55**, 424 (2009).

[131] M. Ablikim et al. (BESIII), “Precise measurement of the $e^+e^- \to \pi^+\pi^- J/\psi$ cross section at center-of-mass energies from 3.77 to 4.60 GeV”, Phys. Rev. Lett. **118**, 092001 (2017).

[132] N. Achasov, A. Kozhevnikov, and G. Shestakov, “Isospin breaking decay $\eta(1405) \to f_0(980)\pi^0 \to 3\pi$”, Phys. Rev. D **92**, 036003 (2015).

[133] N. Achasov and G. Shestakov, “Isotopic Symmetry Breaking in the $\eta(1405) \to f_0(980)\pi^0 \to \pi^+\pi^-\pi^0$.”, JETP Lett. **107**, 276–281 (2018), `arXiv:1804.10749 [hep-ph]`.

[134] M. Ablikim et al. (BESIII), “Observation of $e^+e^- \to K\bar{K}J/\psi$ at center-of-mass energies from 4.189 to 4.600 GeV”, Phys. Rev. **D97**, 071101 (2018), `arXiv:1802.01216 [hep-ex]`.

[135] M. Karliner, J. L. Rosner, and T. Skwarnicki, “Multiquark States”, Ann. Rev. Nucl. Part. Sci. **68**, 17–44 (2018), `arXiv:1711.10626 [hep-ph]`.

[136] M. Ablikim et al. (BESIII), “Observation of a Near-Threshold Structure in the K^+ Recoil-Mass Spectra in $e^+e^- \to K^+(D_s^- D^{*0} + D_s^{*-} D^0)$”, Phys. Rev. Lett. **126**, 102001 (2021), `arXiv:2011.07855 [hep-ex]`.

[137] R. Aaij et al. (LHCb), “Observation of New Resonances Decaying to $J/\psi K^+ +$ and $J/\psi\phi$”, Phys. Rev. Lett. **127**, 082001 (2021), `arXiv:2103.01803 [hep-ex]`.

[138] A. Garmash et al. (Belle), “Amplitude analysis of $e^+e^- \to \Upsilon(nS)\pi^+\pi^-$ at $\sqrt{s} =$ 10.865˜GeV”, Phys. Rev. D **91**, 072003 (2015), `arXiv:1403.0992 [hep-ex]`.

[139] T. N. Truong, “Chiral Perturbation Theory and Final State Theorem”, Phys. Rev. Lett. **61**, 2526 (1988).

[140] T. N. Truong, “Remarks on the unitarization methods”, Phys. Rev. Lett. **67**, 2260–2263 (1991).

[141] A. Dobado and J. R. Pelaez, “The Inverse amplitude method in chiral perturbation theory”, Phys. Rev. **D56**, 3057–3073 (1997).

[142] S. L. Adler, “Consistency conditions on the strong interactions implied by a partially conserved axial-vector current”, Phys. Rev. **137**, B1022–B1033 (1965).

[143] S. L. Adler, “Consistency conditions on the strong interactions implied by a partially conserved axial-vector current. ii”, Phys. Rev. **139**, B1638–B1643 (1965).

[144] M. E. Peskin and D. V. Schroeder, *An Introduction to quantum field theory* (Addison-Wesley, Reading, USA, 1995).

Acknowledgements

This work was supported by the Deutsche Forschungsgemeinschaft (DFG, German Research Foundation), in part through the Collaborative Research Center [The Low-Energy Frontier of the Standard Model, Projektnummer 204404729 - SFB 1044], and in part through the Cluster of Excellence [Precision Physics, Fundamental Interactions, and Structure of Matter] (PRISMA+ EXC 2118/1) within the German Excellence Strategy (Project ID 39083149).